Pedro Henrique Rezende Gonçalves

Structural and electronic transformations upon heating of the Topological Insulator Bi_2Se_3

Dissertation submitted to the UNIVERSIDADE FEDERAL DE MINAS GERAIS (UFMG) as a partial requirement for the Degree of Master in Physics

Advisor: Prof. Dr. Rogério Magalhães Paniago (UFMG)
Co-Advisor: Prof. Dr. Ângelo Malachias de Souza (UFMG)

Belo Horizonte
2018

Acknowledgements

I would like to thanks Prof. Rogério Paniago, for the patience he had with me, his good advices and his friendship;

Professor Ângelo Malachias for the collaboration with this work and his good advices; Professor Mário Sérgio Mazzoni, for the theoretical support; and Thaís Chagas, for also collaborate with this work;

I also thank the fellows of the UHV Nanoscopy Laboratory: Dr. Gustavo Safar, Dr. Diogo Reis, Lucas Marçal, Bárbara Rosa, Otávio Alonso, Luan Calil and Everton Andrade;

The teachers and employees of the Physics Department, for all support I received in my formation;

My friends and family, who gave me the emotional and financial support I have needed. And a special thanks to my father José Carlos Gonçalves, whom I dedicate this work and any accomplishment I may achieve in the future;

The Laboratório Nacional de Luz Síncroton (LNLS), for the support with the X-Ray experiments;

Finally, I wish to acknowledge the financial support from agencies CNPEM, CNPq, Capes, Fapemig and to INCT-Nanocarbono. Their help was essential for the outcome of this dissertation.

Abstract

Bismuth Selenide (Bi_2Se_3) is a topological insulator compound with a lamellar structure formed by the repetition of stacks of five atomic monolayers, each of them consisting of layers with either Se or Bi atoms. Each ensemble of five covalently bonded planes is connected to other quintuple-layers by van der Waals interactions, making this material potentially interesting for building novel devices. Its electronics properties are intimately related to other two-dimensional systems, presenting surface states with an electronic linear dispersion on selected points of the Brillouin zone.

The goal of this work was to observe and interpret the transformations that occur upon heating Bi_2Se_3 at temperatures up to 350°C. X-ray diffraction and Scanning Tunneling Microscopy (STM) techniques were used to observe these transformations. X-ray diffraction was measured following the 00L and 01L truncation rods. These measurements revealed that upon heating there is a coexistence of a major Bi_2Se_3 phase (a three-dimensional topological insulator) and a conducting phase with a structure composed of five Bi_2Se_3 quintuple-layers followed by a bilayer of Bismuth, leading to an overall Bi_4Se_5 stoichiometry.

Density Functional Theory calculations showed that whereas Bi_2Se_3 is a topological insulator, Bi_4Se_5 is a conventional conductor with several van Hove singularities near the Fermi level. STM measurements of the surface of this material showed the presence of hexagonal Bi_4Se_5 domains (approximately 200nm) terminated in Bismuth bilayers embedded in a Bi_2Se_3 matrix. Low temperature scanning tunneling spectroscopy revealed that the bilayer termination exhibits a conducting behavior, with a corresponding conductor-like density of states, presenting no band gap. STS also showed that the bilayer and Bi_2Se_3 are in electrical contact, with the possibility of the presence of a topological state at the edge of the bilayer, since Bismuth islands are two-dimensional topological insulators.

Keywords: Topological Insulators, Scanning Tunneling Microscopy, X-Ray Scattering

Summary

1. INTRODUCTION 9

2. TOPOLOGICAL INSULATORS 11

2.1 SURFACE STATES 11

2.2 QUANTUM HALL EFFECT 14

2.3 QUANTUM SPIN HALL EFFECT: 2D TOPOLOGICAL INSULATORS 16

2.4 3D TOPOLOGICAL INSULATORS AND THE BI-CHALCOGENIDE-BASED CLASS 18

2.5 CRYSTALLINE AND ELECTRONIC STRUCTURE OF Bi_2Se_3 AND Bi_4Se_5 20

3. X-RAY SCATTERING 25

3.1 SCATTERING BY AN ELECTRON 26

3.2 SCATTERING BY AN ATOM 29

3.3 SCATTERING BY CRYSTALS 30

3.4 FORM FACTOR IN THREE DIMENSIONS 32

3.5 UNIT CELL STRUCTURE FACTOR 33

3.6 CRYSTAL TRUNCATION ROD SCATTERING 34

3.7 EXPERIMENTAL SETUP 36

4. SCANNING TUNNELING MICROSCOPY AND SPECTROSCOPY 38

4.1 TUNNELING THROUGH A ONE-DIMENSIONAL SQUARE POTENTIAL 38

4.2 THE SCANNING TUNNELING MICROSCOPE 40

4.3 LANDAUER THEORY OF TUNNELING 41

4.4 BARDEEN THEORY 43

4.5 TERSOFF-HAMANN MODEL 47

4.6 SCANNING TUNNELING SPECTROSCOPY WITH A LOCK-IN AMPLIFIER 49

4.7 EXPERIMENTAL SETUP 52

5. RESULTS AND DISCUSSIONS 55

5.1 X-RAY SCATTERING RESULTSS 55

5.2 DENSITY FUNCTIONAL THEORY CALCULATIONS 61
5.3 SCANNING TUNNELING MICROSCOPY RESULTS 65
5.4 SCANNING TUNNELING SPECTROSCOPY RESULTS 68

6. CONCLUSIONS AND PROSPECTS 71

REFERENCES 72

APPENDIX - PUBLISHED PAPERS RELATED TO THIS DISSERTATION 75

1 - Introduction

One of the most important fields of Physics is related to materials. It is an area of physics that studies in particular the condensed phase, i.e. when the number of constituents of a system becomes very large and the interactions between them are strong [1]. The most known examples are solids and liquids.

The most important fields in Materials Physics are related to their mechanical and electromagnetic properties, i.e., their atomic and electronic structure. This field has become very important since the beginning of the twentieth century due to the discovery of X-rays [2]. They were discovered by the German physicist Wilhelm Conrad Röntgen (1845-1923) on 1895. A few decades later W. Henry Bragg (1862-1942) and his son W. Lawrence Bragg (1890-1971) used this radiation to determine the atomic structure of crystals.

Over the last century until today, several techniques were developed to determine and characterize all kind of materials. In our case, we have used X-Ray Diffraction, Scanning Tunneling Microscopy and Spectroscopy to understand the atomic and electronic properties of our sample: a polyphase crystal formed by two major compounds: Bi_2Se_3 and Bi_4Se_5.

Bismuth Selenide (Bi_2Se_3) belongs to a class of materials called topological insulators. There are many different phases of matter related to their electrical properties: conductors, insulators and semiconductors. Topological insulators are, in a simple explanation, materials which behave like insulators in their interior and conductors at the surface (with very particular features).

Due to phenomena such as the Quantum Hall Effect, surface states appear on bulk insulators, i.e., localized protected metallic states of electrons [3]. An interesting feature of the topological insulators is the topologically protected state, which gives electrons the possibility to pass by non-magnetic barriers without any scattering. This is due to the spin dependence on their conduction, which I similar to massless Dirac particles [4].

This dissertation is divided into 6 chapters. This introduction (Chapter 1) is an attempt to briefly contextualize the importance of Topological Insulators. Chapter 2 involves a discussion about the material we have studied (Bi_2Se_3), first presenting a qualitative introduction to topological insulators in general. A brief and simple explanation using concepts of Quantum Mechanics and the Quantum Spin Hall Effect is given. A comparison between this effect and topological insulators themselves is shown, covering their most important features. At the end of this chapter a short discussion about the structural and electronic properties of Bi_2Se_3 and Bi_4Se_5, the materials we have worked with, is presented.

The next two chapters cover the theory of the experimental techniques we have used. Chapter 3 is about X-Ray Diffraction, focusing on the mathematics behind it and

presenting the technique of Crystal Truncation Rod Scattering (CTRS). Chapter 4 presents the main features of Scanning Tunneling Microscopy (STM) and Spectroscopy (STS), what they can measure and the theory behind them. The main goal of this chapter is to show the relationship between Scanning Tunneling Spectroscopy and the Local Density of states (LDOS) of samples measured using this technique.

Chapters 5 focus on the results of our experiments. X-ray Crystal Truncation Rods were measured at Beamline XRD2 of the Brazilian Synchrotron Light Laboratory (LNLS), located in Campinas/SP. STM and STS experiments were performed at the UHV Nanoscopy Laboratory at UFMG. A discussion about the results and the relationship to Density Functional Theory (DFT) calculations, connecting all previous results, is finally presented. Chapter 6 presents some final considerations and the conclusions of this work.

2 - Topological Insulators

Topological Insulators (TIs) are a new state of matter concerning their topology. They are promising materials for the development of new electronic devices [5] due their distinguished surfaces states [6]. The dispersion relations of the bulk and the surface differ considerably in these materials. They behave as insulators in the bulk and conductors (actually semi-metals) at the surface, presenting a Dirac cone band shape in their energy-momentum diagram [7]. Such behavior is caused by spin-polarized surface states with a linear dispersion relation near the Fermi Level, with topologically protected states for the electrons [8].

The first section of this chapter introduces the theory of surface states in crystalline solids. Sections 2 and 3 cover a simple, qualitatively explanation about the Quantum Hall Effect (QHE), the Quantum Spin Hall Effect (QSHE) and how they are related to two-dimensional topological insulators. Section 4 covers three-dimensional topological insulators, particularly the Bismuth Chalcogenide family. Finally, Section 5 presents the compounds Bi_2Se_3 and Bi_4Se_5 with their predicted electronic and structure properties.

2.1 Surface States

Using Schrödinger´s equation the energies of electrons in a physical system can be calculated [9]. This equation can provide the relationship between energy and position or momentum of these electrons. An atom, for example, has discrete electronic energies given by their quantum numbers n, l and m [9]. For a crystalline solid composed of an array of many atoms, the energy states have a continuous energy-momentum distribution resulting in a band structure [10]. Figure 2.1 is a representation of the band structure of an insulator.

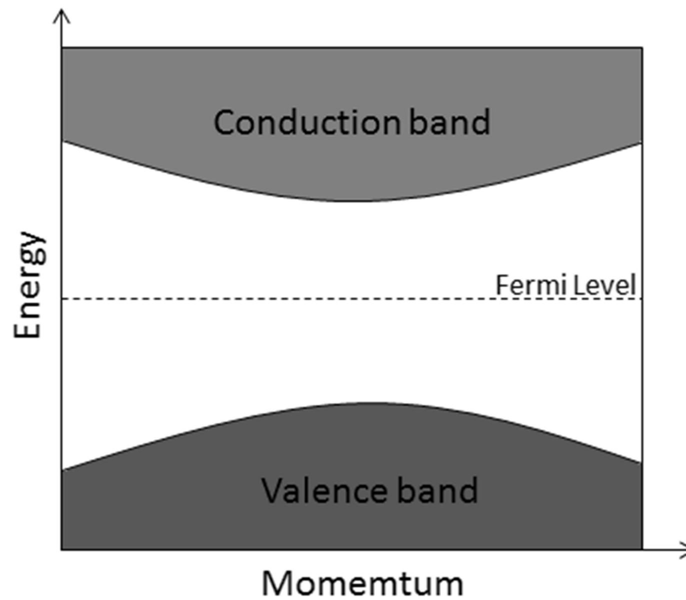

Figure 2.1: Energy-momentum representation of an insulator. The empty space between valence and conduction bands is called *band gap*.

The energy eigenvalues of an electron in a solid can be calculated using the Kronig-Penney model using Bloch functions [11]. This theory uses a simple model of a periodic potential with the Schrödinger equation and it considers a crystal as infinite in all directions. A continuum band structure in the energy (*E*) - momentum (*k*) diagram is obtained. The spatial Bloch functions $\psi_k(x)$ have the form:

$$\psi_k(x) = \mathrm{e}^{ikx} u_k(x) \quad . \tag{2.1}$$

Where $u_k(x)$ is a function with the same periodicity of the crystal. A more realistic model for a crystal takes into account the finite shape of the solid. Considering the solid cleaved in one direction, the consequence is the appearance of surface states. This is due to boundary conditions that need to be satisfied in the Kronig-Penney model for a finite crystal. The concept of surface states was first proposed by Igor Y. Tamm using a one dimensional analytical model [12].

As can be seen in Eq. 2.1, Bloch functions have a unitary complex phase. For a finite case, this restriction is removed. The result is a function which decays when approaching the surface. The Bloch function has to decay to zero into the vacuum. The Bloch functions at the interface solid-vacuum are the same in both two sides. They are represented in Figure 2.2.

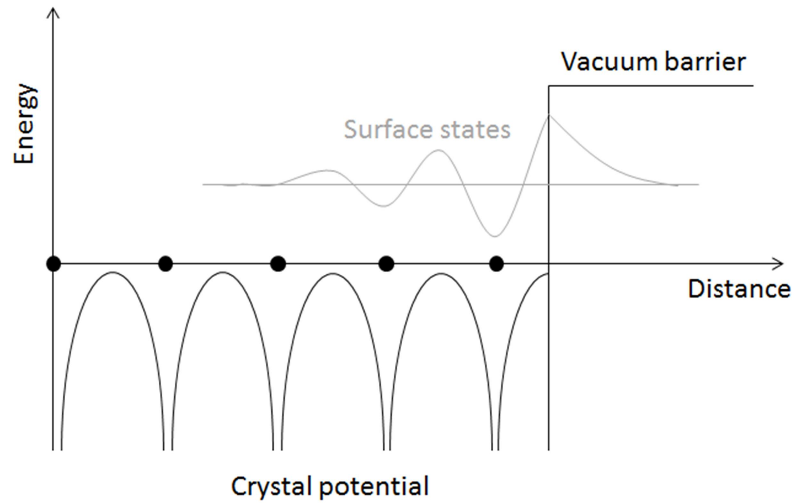

Figure 2.2: Representation of surface states. The surface states decay exponentially into the vacuum and into the solid. Its wave is out of scale for clarity.

The calculations made by Tamm resulted in a simple equation for the energies of the surface states,

$$q'a\cot Ka = \frac{q^2a^2}{2P} - \sqrt{q^2 - {q'}^2}a \quad , \tag{2.2}$$

where $q = \sqrt{2mU}/\hbar$ is a constant determined by the periodic potential, $q' = \sqrt{2mE}/\hbar$ is related to the energy of the electron, P is a normalization parameter and a is the period of the crystalline structure.

With this simple model, one can infer some features of these surface states, i.e., their strength depends on the periodic potential. If P << 1, there will be no surface states. For large values of P, the energy gaps are wide, and the amplitudes of the surface states at the solid surface are large. For transition metals and semiconductors surface states are usually strong. For alkali metals they are weak of even do not exist.

This simple one-dimensional model also predicts the existence of discrete energy levels for surface states. In real solids (three-dimensional case), the lateral Bloch vector always results in dispersion, where the added energy depends on the surface wavevector $\boldsymbol{k} = (k_x, k_y)$:

$$E(k) = E_F - E_0 + \frac{\hbar^2k^2}{2m^*} \quad , \tag{2.3}$$

where E_0 is the electron binding energy, E_F is the Fermi level energy and m^* is the effective mass of the electron in the surface state. Experimentally, surface states have been extensively observed on noble-metal surfaces. Figure 2.3 shows the experimental observation of the $\bar{\Gamma}$ surface state of Au(111).

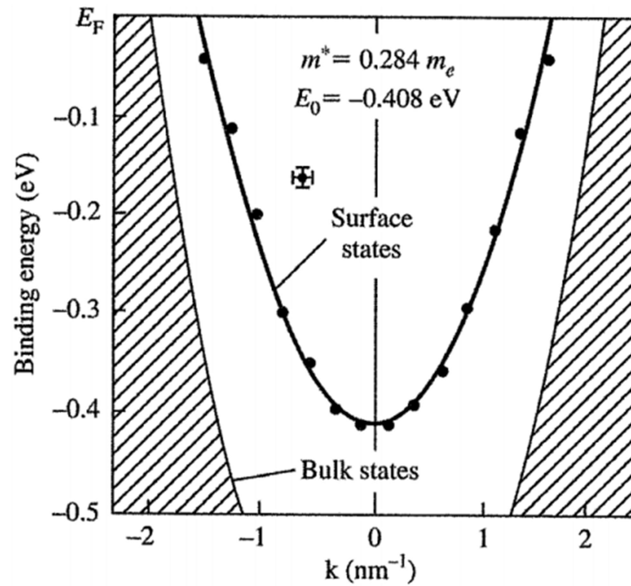

Figure 2.3: Surface state observed for Au(111). The dots represent angle-resolved photoemission data. The solid curve represents the fit to the data using equation 2.3, yielding the binding energy E_0 and the effective mass m^*. From [13].

2.2 Quantum Hall Effect

The concept and the mathematics involved in topological insulators are very complex and difficult to understand. In this dissertation, a simple explanation will be presented. The concepts of Quantum Hall Effect and Surface Sates can be used to give a qualitative idea about the properties of a topological insulator.

First, one can discuss the Quantum Hall Effect (QHE). It was observed for the first time by Klaus von Klitzing in the 1980 decade. Electrons were confined in a two-dimensional interface of two semiconductors and were then submitted to a strong magnetic field at low temperature [14]. The Lorentz force created by the magnetic field leads the electron to move in a well-determined orbit [15]. The movement of electrons is governed by Quantum Mechanics, so the orbits have quantized energies, given by a typical harmonic oscillator relationship $E = (n + \frac{1}{2})\hbar\omega_c$. $\omega_c = eB/m$ is known as the cyclotron frequency. These discrete states are called Landau Levels.

The orbits of the Landau levels are shown in Figure 2.4c. At the borders of the system, the electrons cannot follow their natural trajectory because they are blocked by the vacuum barrier. They move by bouncing back at the border as shown in Figure 2.4c. As a

result, new channels of conduction arrive only at the border. This is an example of a surface state in a two-dimensional system.

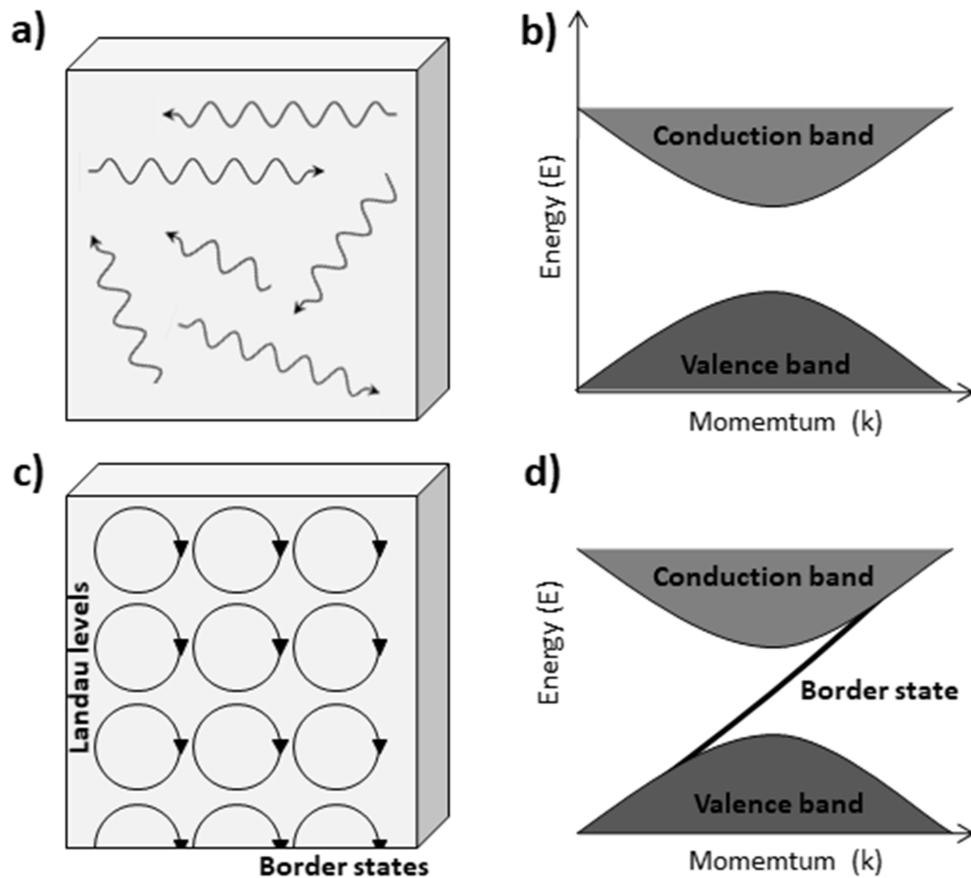

Figure 2.4: The Quantum Hall Insulator. a) Representation of an ordinary insulator. The conducting electrons move freely into the crystal. b) Energy-momentum relation of an ordinary insulator characterized by an energy band gap. c) Representation of a Quantum Hall insulator (QHI) with conducting edge states. In presence of magnetic fields the electrons move on some given orbits, called Landau Levels. The border states occur at the edges of the crystal, where they cannot complete their orbit. d) Energy-momentum relation of a QHI showing the conducting QHE states appearing in the energy band gap.

The conducting surface state at the border has an interesting feature: as the electron cannot change its movement in the direction parallel to the surface, when it encounters a defect or a barrier, its lateral movement is not affected. So the electrons have strong protected states at the border, which makes electron back-scattering forbidden [16]. When in a surface state, electrons contour the defect and continue to propagate.

The von Klitzing experiment also showed that the Hall Conductance exhibits well-defined steps as a function of magnetic field, as shown in Figure 2.5. The Hall Conductance

always presents itself by multiples of e^2/h. This was measured by von Klitzing with a very high precision [14].

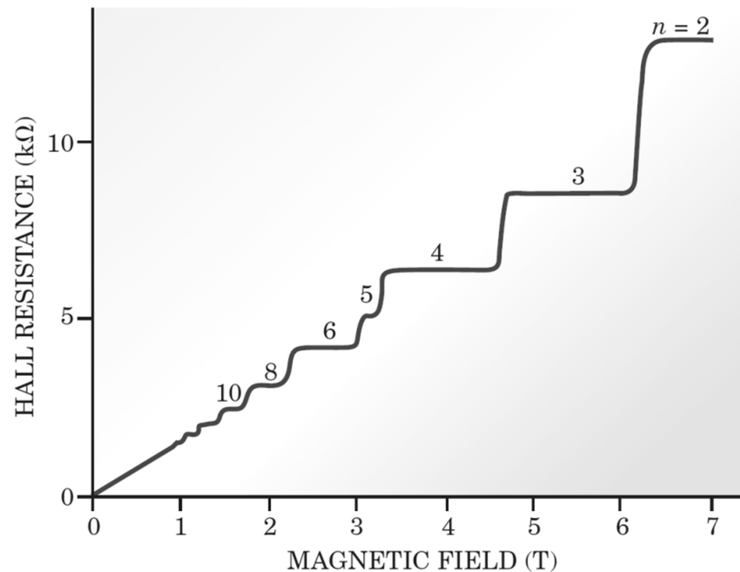

Figure 2.5: Hall resistance as a function of Magnetic field in a 2D electron gas. From [17].

This robust transport mechanism of the surface states with no dissipation can be extremely useful in semiconductor devices. However, strong magnetic fields and low temperatures are necessary and represent a limitation.

Recently, a new class of materials was theoretically predicted [18] and experimentally confirmed [19], presenting states similar to a Quantum Hall solid without the presence of a strong magnetic field. This is possible due to the Quantum Spin Hall Effect, which exists even in the absence of an external magnetic field. This effect and these new materials will be discussed in the next section.

2.3 Quantum Spin Hall Effect: 2D Topological Insulators

The Quantum Spin Hall Effect (QSHE) was theoretically predicted in 2005 in two-dimensional insulators with a strong spin-orbit coupling (SOC) [18]. The spin-orbit coupling of these materials plays the role of the external magnetic field. These materials are called Quantum Spin Hall solids, where topological insulators are a specific group.

The surface states in these materials have an additional property: they are protected by spin polarization. As the role of the magnetic field is played by the electron spin, it has

two orientations, giving two different orbits for the Landau Levels. As a result, surface states have two orientations, each one related to the respective electron spin, as shown in Figure 2.6. The protection feature is given the properties of non-backscattering discussed in the previous section. A structural non-magnetic defect cannot break the robustness of these spin-polarized edge states, but a magnetic one can. This apparent disadvantage can be used to elaborate high-sensitivity magnetic field devices [20].

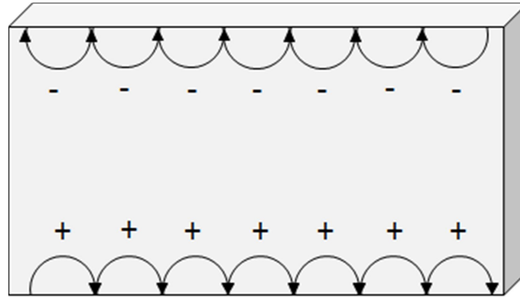

Figure 2.6: Spin-protected states. Due to spin polarization, the electrons on a QSH insulator have two different ways to propagating as surface states.

The two-dimensional topological insulator was originally predicted for graphene [21], albeit not observed. The spin-orbit coupling in a topological insulator has to be strong enough to modify the electronic structure of the material. The spin-orbit coupling is more evident in heavy elements. If the spin-orbit coupling energy is comparable to the bulk gap; it is sufficient to modify the electronic structure of the surface of the material.

In 2006, theoretical studies by B. A. Bernevig e collaborators concluded that quantum wells of CdTe-HgTe-CdTe, above a certain thickness, would present QSH states [18]. The mechanism responsible for the appearance of these states is the spin-obit coupling, which leads to an inversion of the conduction and valence bands.

In most semiconductors, the conduction band is formed by s-type electrons and the valence band by p-type electrons. In heavy elements, the spin-orbit coupling is so strong that it splits the $p_j = 1/2$ and $p_j = 3/2$ levels and leads to a band inversion [22]. By increasing the thickness of the HgTe film, the spin-orbit coupling also increases, leading to this band inversion.

Less than a year after this theoretical prediction, the Quantum Spin Hall Effect was experimentally observed in CdTe-HgTe-CdTe systems by L. Molenkamp and his collaborators [19]. These studies motivated the investigations on topological insulators and three difference theoretical groups generalized the theory for the three-dimensional topological case [23]. 3D topological insulators will be discussed in the next section.

2.4 Three-dimensional Topological Insulators and the Bi-Chalcogenide-Based Class

The theory of 3D topological insulators involves notions of topology and a very complex mathematical treatment. What one needs to know is that using the concept of surface states described in Section 2.1 and the 2D topological insulator from Section 2.3, the 3D topological insulator can be understood as a3D extension of the 2D topological insulator case. The spin-protected conducting border state is now a surface 2D state.

As the quantum wells on CdTe-HgTe-CdTe system, the three-dimensional topological insulator presents a band inversion at the Γ-point of the Brillouin zone due to spin-orbit coupling [23]. The surface states cross the gap at $k = 0$ and near this point the dispersion is linear, which is a characteristic of massless Dirac fermions in one dimension. For 3D topological insulators, this crossing of the surface states arises in what is called a *Dirac-Cone*, due to its cone shape, as shown in Figure 2.7.

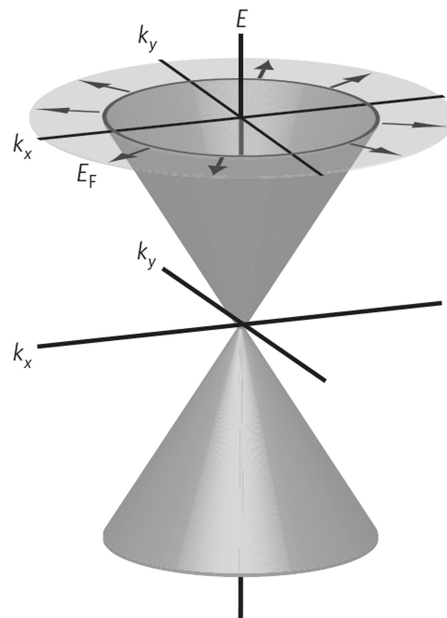

Figure 2.7: The Dirac-cone of a 3D topological insulator. From [24].

As in the 2D case, the direction of the electrons at the surface is determined by their spins, which now varies continually as function of the propagation. There are well-defined energy-momentum paths which electrons with a given spin can have and the opposite cannot. The first candidate for a 3D topological insulator was a Bismuth Antimonide alloy $Bi_{1-x}Sb_x$. It was predicted that for the range of concentration x=0.09 to x=0.18, $Bi_{1-x}Sb_x$ is a

topological insulator [25], and this was proven by Angular Resolved Photo-emission Spectroscopy (ARPES) measurements by Hsieh et al. [26].

The electronic structure of $Bi_{1-x}Sb_x$ is very complicated because it presents normal surface states besides the topological insulators states [27]. So, it can be really difficult to measure the topological state alone. The weak gap (100 meV) is also a limiting factor, reducing the visualization of this effect to very low temperatures.

Latter studies predicted the existence of a second generation of topological insulators, the chalcogenide-based TIs: Bi_2Te_3, Bi_2Se_3, Sb_2Te_3, etc. As in the previous cases the experimental proof was obtained using ARPES for Bi_2Te_3 [28], Bi_2Se_3 [29] and others [30], evidencing the signature of a 3D topological insulator.

These materials present all the features of a 3D topological insulator discussed before: 2D protected metallic states localized at the surface, a Dirac-cone, conduction without dissipation, defect robustness, spin-polarization, etc. The mainly advantage of the second generation to the first one are the band structure near to the ideal case. They present only one Dirac-cone and a sufficiently large band gap, 300 meV for Bi_2Se_3, to make them usable at room-temperature. Its atomic structure is shown in Figure 2.8.

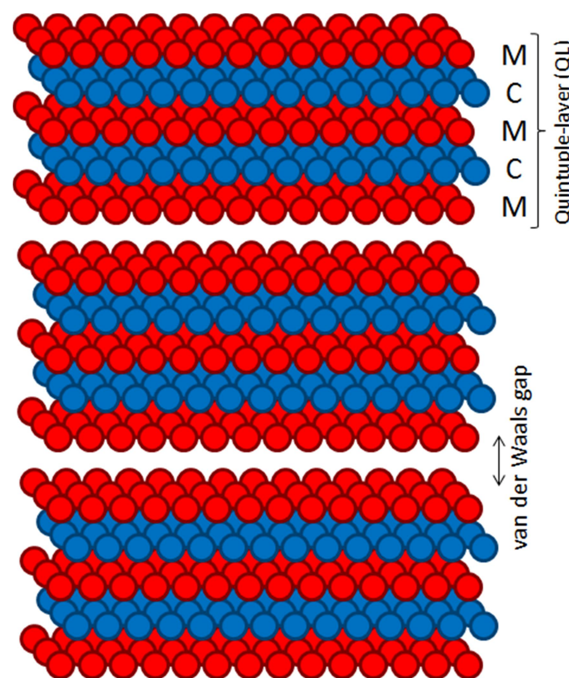

Figure 2.8: Basic atomic structure of Bi-Chalcogenide class of TIs. Letter M represents a metal that can be Se, Te, etc. C is the chalcogenide atom: Bi, Sb, etc. These stacks bonded by van der Waals forces form compounds like Bi_2Se_3 and Bi_2Te_3.

This second generation of TIs also has the advantage that they are stoichiometric, making them easy to produce with high purity. They present the same basic atomic structure: rhombohedral lattice with fifteen atoms in the unit cell. The structure presents a stacking of quintuple-layers (QLs) with M-C-M-C-M atoms, where M is a metallic atom (Se or Te) and C is the chalcogenide (Bi, Sb, etc.). The most common compounds are Bi_2Te_3 and Bi_2Se_3. The stacking is of ABC type, so three QLs are needed to make a unit cell. Inside the quintuple-layer the atoms are bonded by covalent forces, but the force which binds the QLs together is of van der Waals nature. As the van der Waals force is weaker than covalent ones, the material can be easily exfoliated at the QLs interface.

2.5 Crystalline and electronic structure of Bi_2Se_3 and Bi_4Se_5

The crystalline structure of Bismuth Selenide (Bi_2Se_3) is the same as shown in Figure 2.8 at the previous section, with stacks of quintuple-layers of Se-Bi-Se-Bi-Se. The atoms are hexagonally-packed as can be seen in the atomically-resolved STM image of Figure 2.9. The unit cell has atomic distances of 0.41 nm for the x-y plane lattice parameters and 2.84 nm in the z direction.

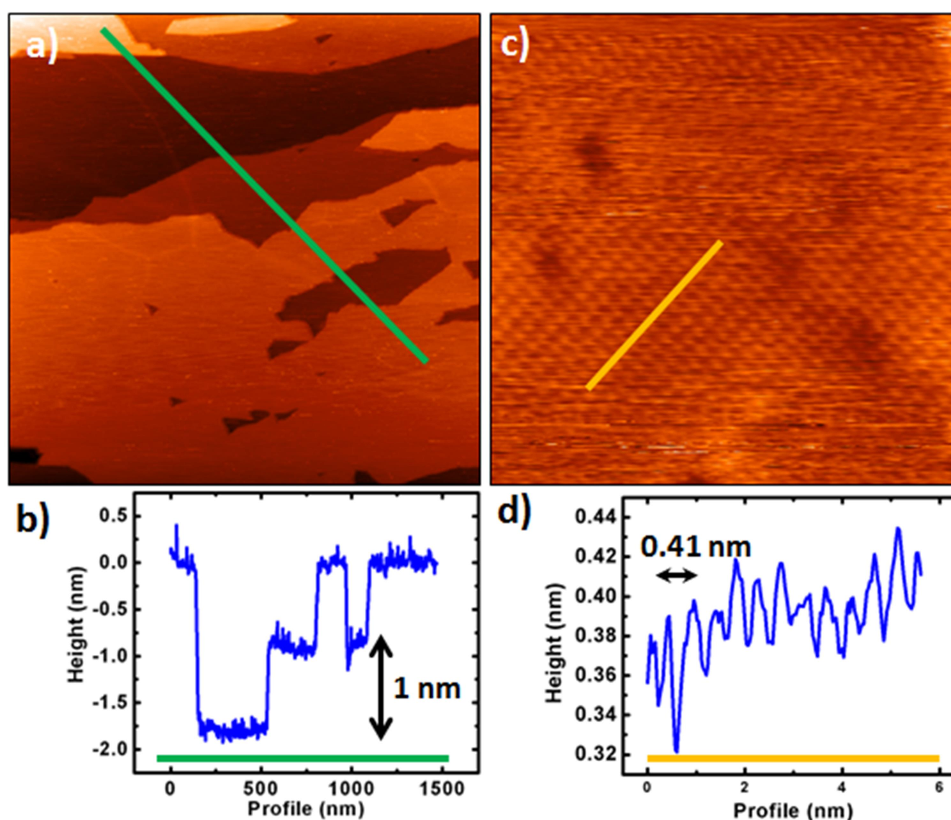

Figure 2.9: Scanning Tunneling Microscopy (STM) images of Bi_2Se_3. a) 1.2µm^2 STM image of Bi_2Se_3. b) A line profile of (a) showing the 1 nm space between QLs. c) 16nm^2 high-resolution image of Bi_2Se_3. d) A line profile of (c) showing the x-y atomic distance between atoms of 0.44 nm.

The electronic structure of Bi_2Se_3 can be determined by Angle-Resolved Photo-emission Spectroscopy (ARPES). It presents a Dirac-cone lying in between the conduction and valence bands centered at the Γ-point. The ARPES measurements revealed a non-expected behavior for this material. The Dirac-point is not exactly at the Fermi-level, as predicted by theoretical calculations. This difference between theory and experiment is due to defects at the Bi_2Se_3 crystalline surface. Holes of Se at the surface can induce a natural doping of the material which changes the position of the Fermi-level [31]. One way to bring the Fermi-level to the Dirac-point by is by doping the material with, for example, Calcium [32]. Figure 2.10 shows an ARPES measurement of pure-Bi_2Se_3 and DFT calculations of its electronic band structure.

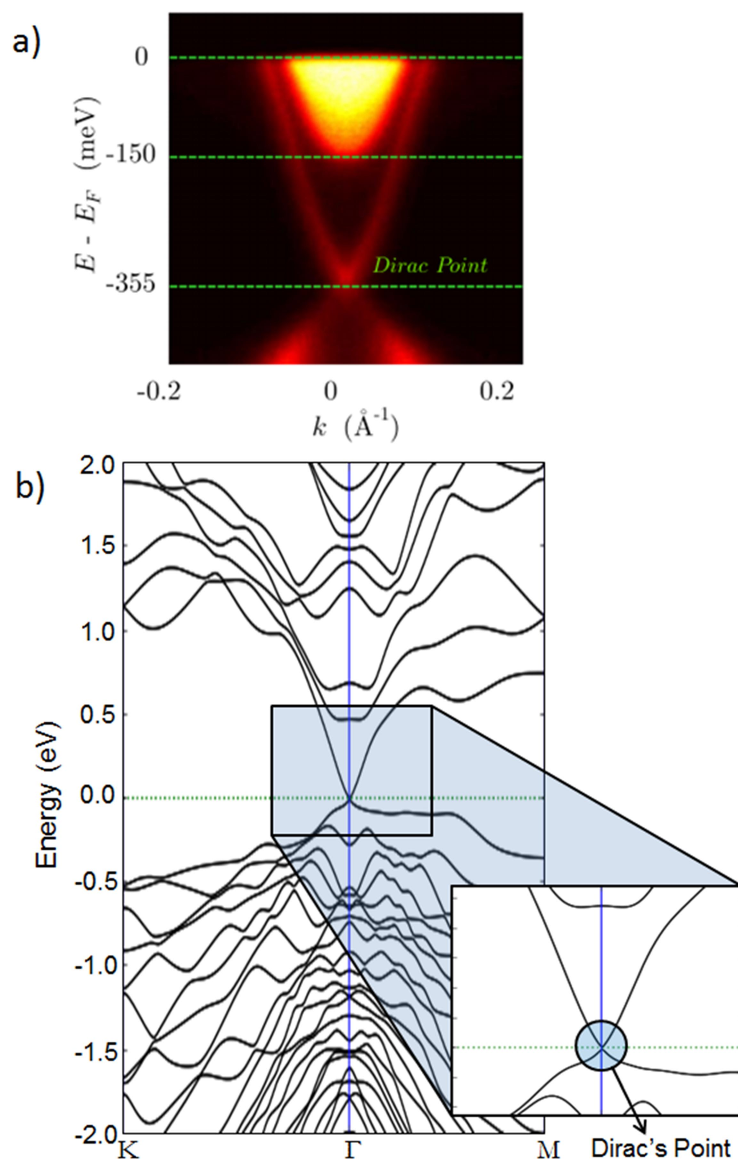

Figure 2.10: The electronic band structure of Bi_2Se_3. a) ARPES measurements showing the Fermi-level at the conduction band, away from the Dirac-point. From [33]. b) Density Functional Theory (DFT) calculations of the electronic band structure of Bi_2Se_3, showing the Dirac-point at the Fermi-level. Image made with the software Virtual NanoLab by QuantumWise A/S.

One of the best properties of Bi_2Se_3 is its stoichiometry condition. With three atomic parts of selenium and two of bismuth, it is possible to synthesize high-quality Bi_2Se_3 crystals. Studies of Bi_2Se_3 growth have shown that in excess of selenium, Bi_2Se_3 is always synthesized and the excess of selenium is phase-separated. With a lack of selenium other phases of Bismuth Selenide can be formed. In Figure 2.11 the Bi-Se phase diagram is shown with all possible phases.

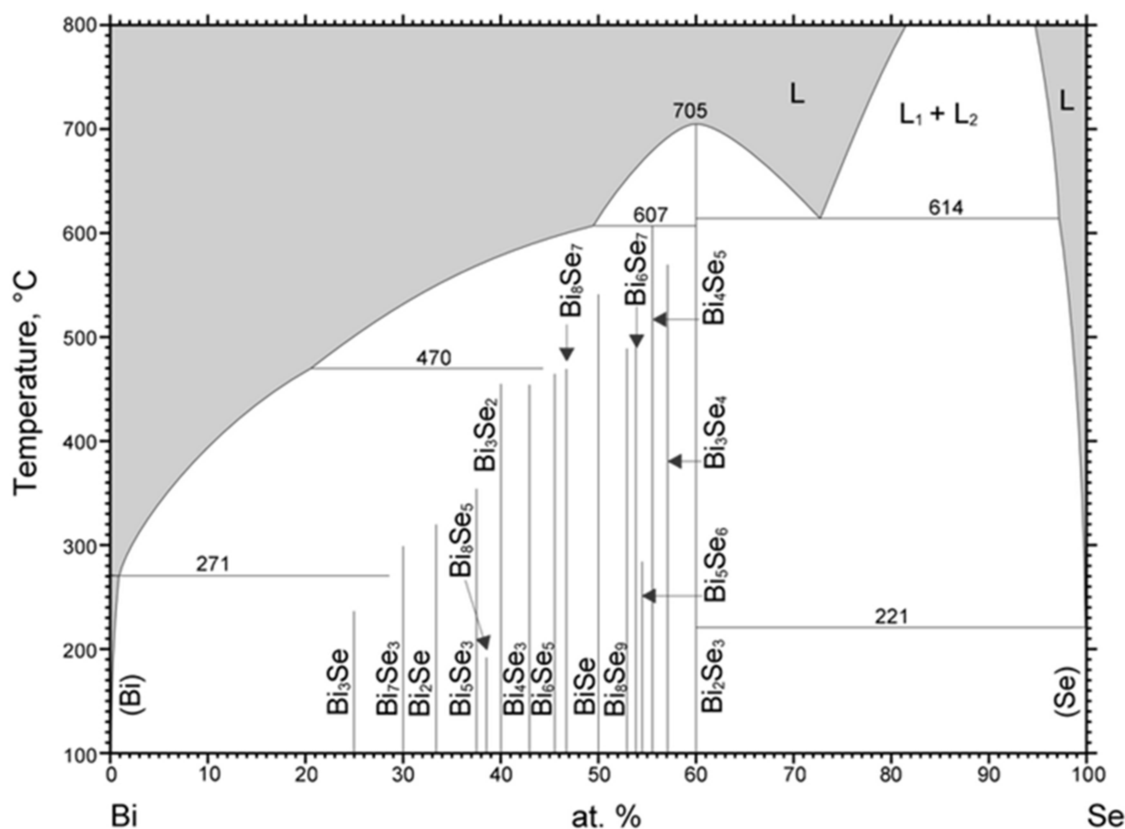

Figure 2.11: Phase diagram of the BiSe system. The graph shows the phases of Bismuth Selenide that can be formed by a given temperature, percentage of bismuth and selenium. From [34].

X-ray measurements, which will be discussed in Chapter 3, showed that our sample contains the main Bi_2Se_3 phase and other minor phases. Among these minor phases the more evident is Bi_4Se_5. The unit cell of Bi_4Se_5 is formed by five Bi_2Se_3 quintuple-layers and a Bismuth bilayer on top of it. The unit cell can be understood as two unit cells of Bi_2Se_3 with one quintuple layer replaced by a Bismuth bilayer. An illustration of these stacks is shown in Figure 2.12.

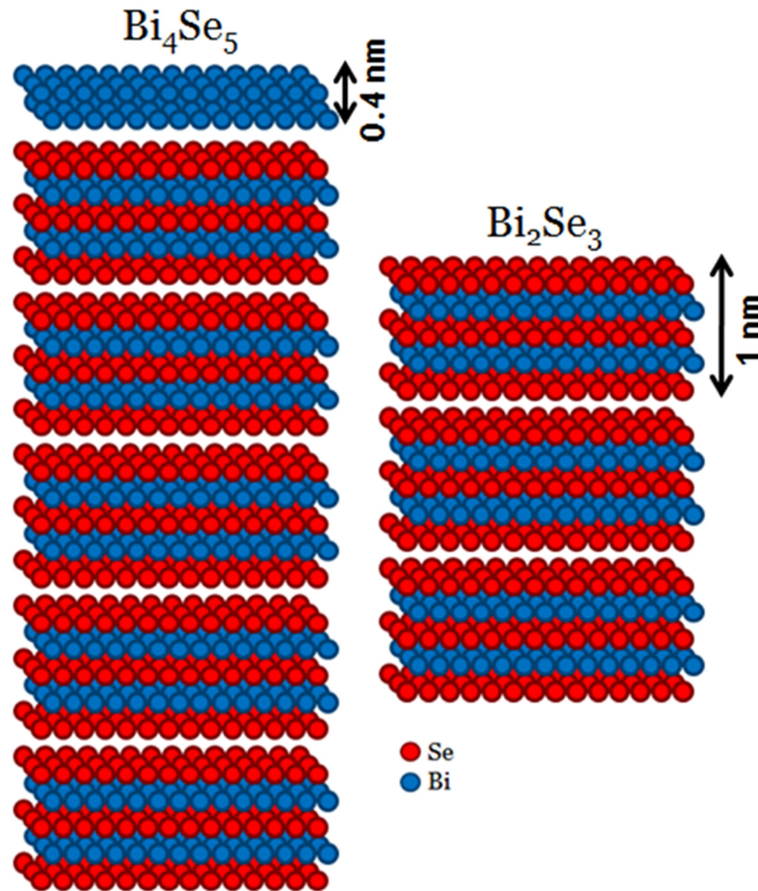

Figure 2.12: Unit cell of Bi_4Se_5 and Bi_2Se_3. Bi_4Se_5 phase is formed by 5 QLs of Bi_2Se_3 and a Bi_2 bilayer.

As can be seen in the literature, the main phases of Bismuth Selenide are formed by the intercalation of Bi_2Se_3 quintuple-layers and Bi_2bilayers [35]. For example: two QLs with a bilayer form BiSe, three QLs with a bilayer form Bi_3Se_4, etc. A comparative table is shown in Table I.

% Selenium	Number of QLs	Number of BLs	Number of Bismuth atoms per unit cell	Number of Selenium atoms per unit cell	Phase formed
43,0	1	1	4	3	Bi_4Se_3
50,0	2	1	6	6	BiSe
53,0	3	1	8	9	Bi_8Se_9
55,5	4	1	10	12	Bi_5Se_6
56,5	5	1	12	15	Bi_4Se_5
57	8	1	18	24	Bi_3Se_4
60	3	0	6	9	Bi_2Se_3

Table I: Comparative table of the atomic composition in the unit cell of the $(Bi_2Se_3)_x(Bi_2)_y$ compounds.

The electronic band structure of Bi_4Se_5 differs considerably from Bi_2Se_3. Density Functional Theory (DFT) can be used to predict its band structure. Scanning tunneling spectroscopy can locally differentiate the electronic density of states of both phases. The Bi_4Se_5 phase is not expected to be a topological insulator and our measurements confirm this prediction. This will be shown in Chapter 5 of this dissertation.

3 - X-Ray Scattering

X-Rays were discovered by Wilhelm Conrad Röntgen (1845-1923) in 1895 when investigating cathodic rays. He observed that when electrons decelerate they produce this penetrating kind of radiation. The first Nobel Prize was awarded to him in 1901 "in recognition of the extraordinary services that rendered the discovery of the remarkable rays subsequently named after him".

Further works of William Henry Bragg (1862-1942) and his son William Lawrence Bragg (1890-1971) showed that one can study the crystalline structure of solids using X-ray radiation, due to their wavelength between 0.01 and 10 nanometers, which is comparable to the inter-atomic distance in solids. They both won the Nobel Prize in 1915 "for their services in the analysis of crystal structures by means of X-rays".

One method to produce X-rays in an intense and effective way is to use Synchrotron X-ray sources (Figure3.1). In the early 70's, scientists observed that electrons accelerating in storage rings, which were initially built to performed high energy nuclear physics experiments, produce X-rays when they pass along a curve of the storage ring [36]. After this discovery, scientists around the world started to build accelerators only to produce X-rays.

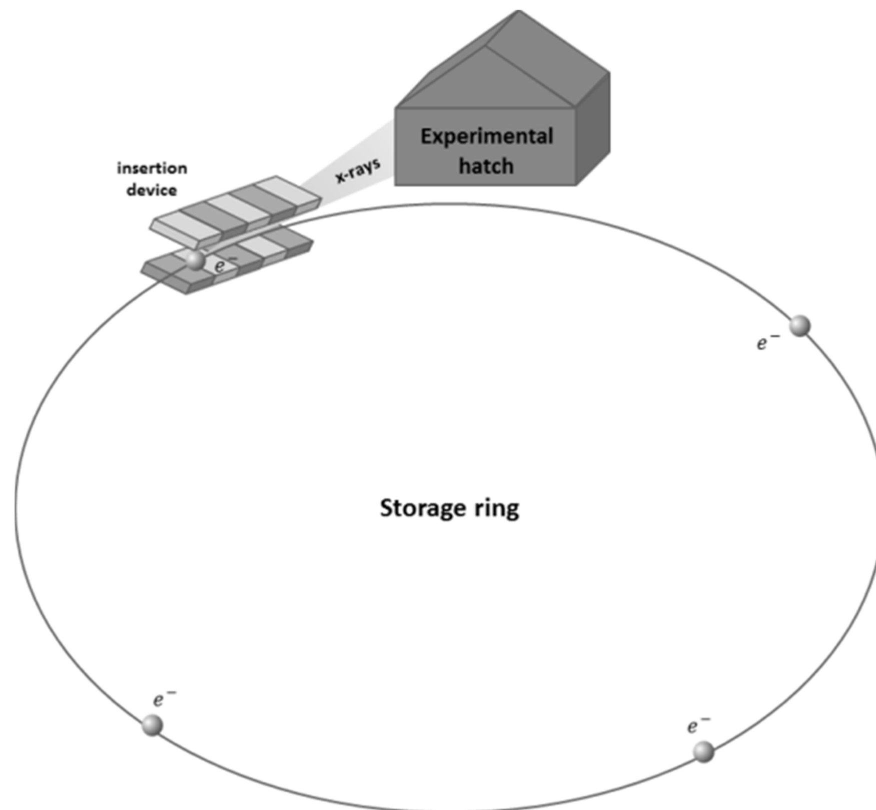

Figure 3.1: A simple schematic of a typical X-ray Beamline at a third generation X-ray source. When electrons pass into a curve along a storage ring, they produce rays that are monochomatized and focused to be used into an experimental hatch called Beamline.

Since the major experiments in this area use monochromatic radiation, an X-ray beam may be represented by a monochromatic plane wave (Figure 3.2), where its electric field is given by

$$\mathbf{E}(\mathbf{r},t) = \mathrm{E}_0\hat{\boldsymbol{\varepsilon}}\mathrm{e}^{\mathrm{i}(\mathbf{k}\cdot\mathbf{r}-\omega t)} \; . \tag{3.1}$$

$\mathrm{E}_0$is the amplitude of the electric field, $\hat{\boldsymbol{\varepsilon}}$ is the unitary polarization vector, $\mathbf{k}$ is the electron wavevector and ω the angular frequency of the wave.

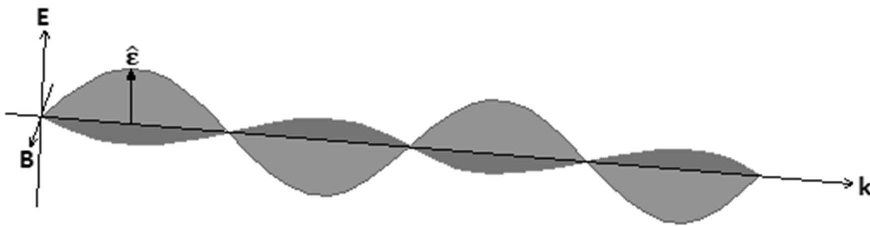

Figure 3.2: A monochromatic plane electromagnetic wave.

When X-rays interact with an atom, they can be absorbed or scattered [36]. The absorption process will not be discussed in this work, which focuses in the scattering process. The X-ray Diffraction experiment consists on shining X-ray radiation onto a crystal sample and measure the intensity of the diffracted beam. To measure this intensity a photon counter detector is used at a fixed distance to the sample, equipped with a diffractometer. The diffractometer is the equipment used to move the detector and the sample to angles where we want to measure the scattered intensity.

In the next sections, we present the mathematics of the scattering process of X-rays by an electron, an atom and a crystal; finalizing with the crystal truncation rod diffraction, which was performed in our experiment.

3.1 Scattering by an electron

For the understanding of the scattering phenomena in crystals, we first need to study the scattering of a single electron by the electromagnetic wave, the X-ray. Classical electromagnetic theory tells us that when an X-ray wave interacts with an electron, its electric field forces it to vibrate and generating a radiated wave [37]. The vibrating electron can be understood as a radiation source, producing a spherical wave.

The goal of this section is to calculate the intensity of the scattered wave at a given distance from the source, which will be sum of the incident and radiated waves. Considering the vector potential of the source charges:

$$\mathbf{A}(\mathbf{r},t') = \frac{1}{4\pi\epsilon_0 c^2}\int_V \frac{\mathbf{J}(\mathbf{r}',\mathrm{t}')}{|\mathbf{r}-\mathbf{r}'|}d\mathbf{r}' \;, \tag{3.2}$$

where $\mathbf{J}(\mathbf{r}',t')$ is the current density of the source. $|\mathbf{r}-\mathbf{r}'|$ is the distance between the source $\mathbf{r}$ and the observation point $\mathbf{r}'$; and ϵ_0 is the vacuum permittivity. The factor $t' = t - |\mathbf{r}-\mathbf{r}'|/c$ refers to the fact that the field propagates with a finite velocity c. This retarded vector potential gives us the electric field $\mathbf{E}$ and the magnetic field $\mathbf{B}$ by the following equations:

$$\mathbf{E} = -\nabla\Phi - \frac{\partial\mathbf{A}}{\partial \mathrm{t}} \qquad \text{and} \tag{3.3a}$$

$$\mathbf{B} = \nabla \times \mathbf{A} \;. \tag{3.3b}$$

As the electron is considered free, the electric potential $\Phi = 0$and $\mathbf{E}$ and $\mathbf{B}$ depend only on the vector potential $\mathbf{A}$. Using the dipole approximation [37], $\mathbf{r} \gg \mathbf{r}'$, and evaluating the integral in Eq. 3.2, the retarded vector potential becomes proportional to the derivative of the electric dipole moment, and equation 3.2 becomes

$$\mathbf{A}(\mathbf{r},t) \approx \frac{1}{4\pi\epsilon_0 c^2 \mathrm{r}}\dot{\mathbf{p}}(t') \;. \tag{3.4}$$

Where $\dot{\mathbf{p}}(t')$ is the derivative of the dipole moment at the retarded time t'. Using Eq. 3.3b and considering that we are only interested in the case of larger distances r (the $1/r^2$ term can be neglected), $\mathbf{B}$ will be expressed by

$$\mathbf{B} \approx \left(\frac{1}{4\pi\epsilon_0 c^2}\right)\frac{1}{c\mathrm{r}}\ddot{\mathbf{p}}(t') \times \hat{\mathbf{r}} \;. \tag{3.5}$$

Where $\ddot{\mathbf{p}}(t')$ is the second derivative of the dipole moment at the retarded time t'. The numerical value of the vector product in Eq. 3.5 is $\ddot{\mathrm{p}}\cos\psi$, with ψ shown in Figure 3.3a. The modulus of the amplitude of electromagnetic waves is given by the relation $|\mathbf{E}| = c|\mathbf{B}|$. The electric field is then

$$\mathrm{E(t)} = \left(\frac{1}{4\pi\epsilon_0 c^2}\right)\frac{1}{\mathrm{r}}\ddot{\mathrm{p}}(t')\cos\psi \tag{3.6}$$

and evaluating $\ddot{\mathrm{p}}$:

$$\ddot{\mathrm{p}}(t') = q\ddot{\mathrm{z}} = q\frac{q\mathrm{E_{in}}}{m} = \frac{q^2}{m}\mathrm{E_0 e^{-i\omega(t-r/c)}} \;.$$

Where $\ddot{z}$ is the acceleration of the wave, E_{in} is the incident electric field, m the mass of the electron and q its charge. Finally, the electric field of the radiated wave can be written as

$$E(t) = -r_0 \left(\frac{e^{ikr}}{r}\right)\left(E_0 e^{i\omega t}\right)\cos\psi \ , \tag{3.7}$$

where, $r_0 = e^2/4\pi\epsilon_0 mc^2$ is called Thomson scattering length and $\cos\psi = |\hat{\boldsymbol{\varepsilon}} \cdot \hat{\boldsymbol{\varepsilon}}'|$ is related to the different polarization of the incident and scattering waves (see Figure 3.3b). The e^{ikr}/r factor represents the spherical radiated wave and the $E_0 e^{i\omega t}$ factor represents the incident plane wave. The scattering amplitude depends on the position of the detector. As can be seen in Figure 3.3b, if the detector is positioned along the y-axis, the $\cos\psi = 0$ and there is no signal at the detector. For the case of a synchrotron source, where a diffraction experiment is performed along the vertical scattering plane, $\cos\psi = 1$.

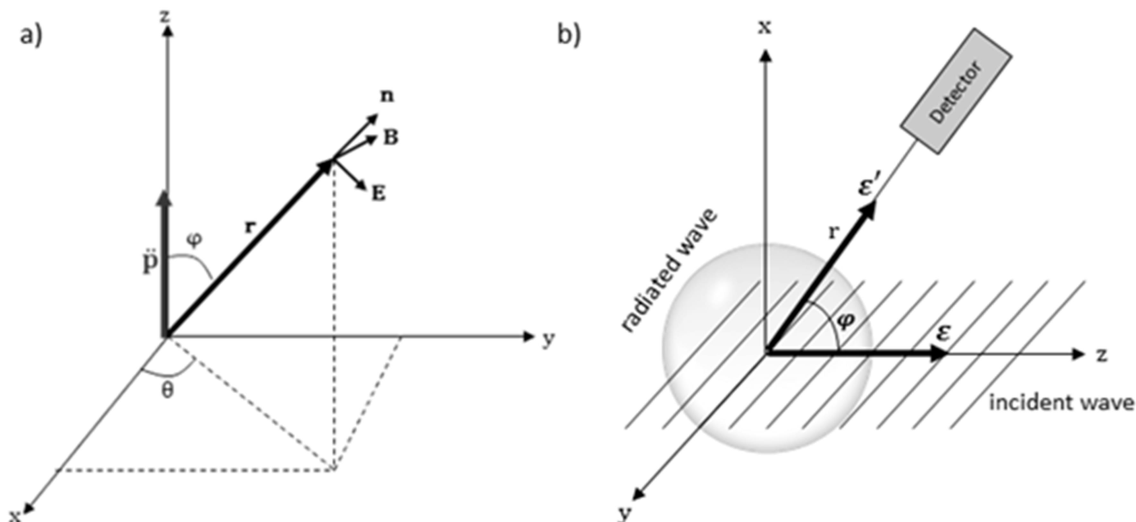

Figure 3.3: a) An electromagnetic plane wave polarized with its electric field along the z axis forces a dipole at the origin to oscillate and generates a radiated wave. b) The scalar product between incident and radiated waves is also$\cos\psi$.

The intensity of the scattered wave is proportional to $|\mathbf{E}|^2$. Looking at Equation 3.7, one obtains the amplitude of the radiated wave is a constant in a given distance and does not depend on the energy. This result is relevant to X-rays, where the photons are energetic enough that even atomic electrons can be approximated as free. This breaks down entirely at low energies in the optical part of the electromagnetic spectrum [36].

3.2 Scattering by an atom

As discussed before, the scattering of an atom can be understood as the sum of the scattering of all electrons in the atom. The interactions of the nucleus and the X-rays can be neglected due to their higher mass. Instead of considering the electrons in the atom as punctual charges, one can introduce a charge density distribution.

Looking at Eq. 3.7 for the amplitude of the radiated wave, the difference is that, instead of one electron, we have now the sum of the scattering of all electrons. This sum can be written as an integral over the charge density. One obtains a similar equation, except that the Thomson scattering length r_0 is replaced by the atomic form factor:

$$\mathrm{r}_0 f^0(\mathbf{Q}) = \mathrm{r}_0 \int \rho(\mathbf{r}) \mathrm{e}^{\mathrm{i}\mathbf{Q}\cdot\mathbf{r}} \mathrm{d}\mathbf{r} \ . \quad (3.8)$$

Where $\rho(\mathbf{r})$ is the charge density of the atom and $\mathbf{Q}$will be discussed below. Eq. 3.8 has a $\mathrm{e}^{\mathrm{i}\mathbf{Q}\cdot\mathbf{r}}$ term which differs from the integral of the total charge of the atom. This is because different volume elements $\mathrm{d}\mathbf{r}$ of the charge density interact with the X-rays with different phases, as shown in Figure3.4. The same phenomenon occurs with the scattered waves.

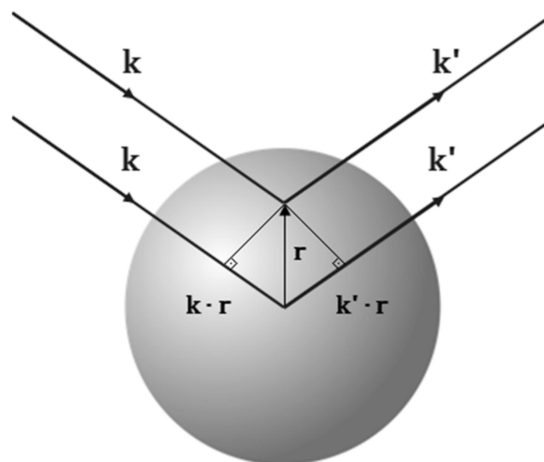

Figure 3.4: Scattering from an atom. An X-ray with a wavevector k scatters from an atom in the direction specified by k'.

The phase difference between a volume element at the origin and one at a distance $\mathbf{r}$ is

$$\Delta\varphi(\mathbf{r}) = (\mathbf{k} - \mathbf{k}') \cdot \mathbf{r} = \mathbf{Q} \cdot \mathbf{r} \ , \quad (3.9)$$

where $\mathbf{Q} = \mathbf{k} - \mathbf{k}'$ is known as the scattering vector. The scattering length of an atom is the sum of the scattering lengths of all volume elements of the charge density, $\rho(\mathbf{r})\mathrm{d}\mathbf{r}$, each one with a phase factor $e^{i\mathbf{Q}\cdot\mathbf{r}}$ as shown in Eq. 3.8. $f^0(\mathbf{Q})$, the atomic form factor (AFF) represents the contribution of all electrons in the atom. In the limit case where all volume elements scatter in phase, $f^0(\mathbf{Q} \to 0) = Z$, and the total scattering amplitude is the sum of the amplitudes of all electrons.

3.3 Scattering by crystals

The scattering of a crystal by X-rays is the sum of the scattering amplitudes of all atoms in it. The calculation is simple if one treats the atoms in the crystal in a coordinate representation, the crystal lattice. First, we start choosing a unit cell, the cell which is repeated over the entire crystal. A given atom can be represented by the coordinates of two vectors:

$$\mathbf{R}_n = n_1\mathbf{a}_1 + n_2\mathbf{a}_2 + n_3\mathbf{a}_3 \tag{3.10}$$

and

$$\mathbf{r}_j = x_j\mathbf{a}_1 + y_j\mathbf{a}_2 + z_j\mathbf{a}_3 \quad . \tag{3.11}$$

The first vector, $\mathbf{R}_n$, gives the position of the unit cell, related to all cells of the crystal, with the integer numbers n_1, n_2, n_3 labeling the cell. The second one, $\mathbf{r}_j$, gives the position of the j-atom inside the chosen cell. Figure 3.5 shows an example of the crystal lattice coordinate system in a two-dimensional crystal.

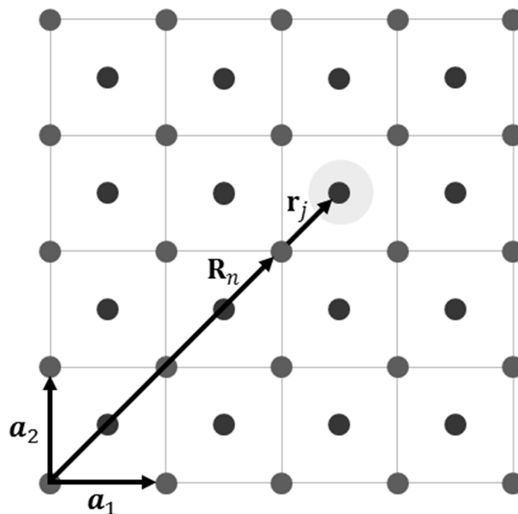

Figure 3.5: Example of a crystal lattice. The highlighted atom has the lattice coordinates $\mathbf{R}_n = 2\mathbf{a}_1 + 2\mathbf{a}_2$ and $\mathbf{r}_j = 0.5\mathbf{a}_1 + 0.5\mathbf{a}_2$.

The scattering amplitude of the crystal, as said before, is the sum over all atoms. Using the lattice coordinate system, this sum can be expressed by

$$F^{\text{crystal}}(\mathbf{Q}) = \overbrace{\sum_j f_j(\mathbf{Q})\mathrm{e}^{i\mathbf{Q}\cdot\mathbf{r}_j}}^{\substack{\text{Unit cell} \\ \text{structurefactor}}} \overbrace{\sum_n \mathrm{e}^{i\mathbf{Q}\cdot\mathbf{R}_n}}^{\text{Form Factor}} \quad . \tag{3.12}$$

The sum can be factorized in two terms. The first one, related to the unit cell, is called the structure factor. The second one, related to the crystal itself and being the sum of all cells of the crystal, is called lattice sum or form factor.

The form factor is a sum composed by phase factors, in a unitary circle of the complex plane. The entire sum is finite only if the scattering vector follows

$$\mathbf{Q}\cdot\mathbf{R}_n = 2\pi \times \text{integer} \quad . \tag{3.13}$$

In this case, the sum is of order N, the number of cells in the crystal. The solution to Eq.3.13 in a general three-dimensional crystal is found using the reciprocal lattice [11]. The representation of a lattice site in reciprocal space is given by

$$\mathbf{G} = h\mathbf{b}_1 + k\mathbf{b}_2 + l\mathbf{b}_3 \quad , \tag{3.14}$$

where h, k, l are all integers. The inner product of vector $\mathbf{G}$ and the real lattice vector $\mathbf{R}_n$ is

$$\mathbf{G}\cdot\mathbf{R}_n = 2\pi(hn_1 + \mathrm{kn}_2 + \mathrm{ln}_3) = 2\pi \times \text{integer} \quad . \tag{3.15}$$

So, analyzing Eq. 3.13 and Eq. 3.15, we have:

$$\mathbf{Q} = \mathbf{G} \quad . \tag{3.16}$$

Equation 3.16 is known as the Laue condition and is equivalent to Bragg's Law $n\lambda = 2d\mathrm{sen}\theta$. The lattice sum is non-vanishing if and only if $\mathbf{Q}$ coincides with a reciprocal lattice vector. In other terms, the scattering intensity will be finite in integer reciprocal lattice points of the crystal, called diffraction points.

In this section it was assumed that the interaction between X-rays and the crystal is weak, not allowing the X-ray beam to be scattered for a second or third time before it leaves the crystal. This assumption leads to considerable simplicity and it is known as the kinematical approximation [36].

The next two sections of this chapter we present discuss the Form Factor and the unit cell Structure Factor.

3.4 Form Factor in three dimensions

In this section we will perform the calculation of the Form Factor for a three dimensional finite crystal. Separating the sum in Eq. 3.12, we have the lattice sum:

$$F_N(\mathbf{Q}) = \sum_{n=0}^{N-1} \mathrm{e}^{i\mathbf{Q}\cdot\mathbf{R}_n} = \sum_{n_1=0}^{N_1-1}\sum_{n_2=0}^{N_2-1}\sum_{n_3=0}^{N_3-1} \mathrm{e}^{i\mathbf{Q}\cdot\mathbf{R}_n} = \sum_{n_1=0}^{N_1-1}\sum_{n_2=0}^{N_2-1}\sum_{n_3=0}^{N_3-1} \mathrm{e}^{i\mathbf{Q}\cdot(n_1\mathbf{a}_1+n_2\mathbf{a}_2+n_3\mathbf{a}_3)}$$

$$F_N(\mathbf{Q}) = \sum_{n_1=0}^{N_1-1} \mathrm{e}^{in_1\mathbf{Q}\cdot\mathbf{a}_1} \sum_{n_2=0}^{N_2-1} \mathrm{e}^{in_2\mathbf{Q}\cdot\mathbf{a}_1} \sum_{n_3=0}^{N_3-1} \mathrm{e}^{in_3\mathbf{Q}\cdot\mathbf{a}_1}$$

Then, evaluating the sums:

$$F_N(\mathbf{Q}) = \frac{\mathrm{e}^{iN_1\mathbf{Q}\cdot\mathbf{a}_1}-1}{\mathrm{e}^{i\mathbf{Q}\cdot\mathbf{a}_1}-1}\frac{\mathrm{e}^{iN_2\mathbf{Q}\cdot\mathbf{a}_2}-1}{\mathrm{e}^{i\mathbf{Q}\cdot\mathbf{a}_2}-1}\frac{\mathrm{e}^{iN_3\mathbf{Q}\cdot\mathbf{a}_3}-1}{\mathrm{e}^{i\mathbf{Q}\cdot\mathbf{a}_3}-1}$$

$$= \mathrm{e}^{iN_1\mathbf{Q}\cdot\mathbf{a}_1/2}\frac{\mathrm{e}^{iN_1\mathbf{Q}\cdot\mathbf{a}_1}-\mathrm{e}^{iN_1\mathbf{Q}\cdot\mathbf{a}_1}}{\mathrm{e}^{i\mathbf{Q}\cdot\mathbf{a}_1}-\mathrm{e}^{iN_1\mathbf{Q}\cdot\mathbf{a}_1}}\mathrm{e}^{iN_1\mathbf{Q}\cdot\mathbf{a}_1/2}\frac{\mathrm{e}^{iN_2\mathbf{Q}\cdot\mathbf{a}_2}-\mathrm{e}^{iN_2\mathbf{Q}\cdot\mathbf{a}_2}}{\mathrm{e}^{i\mathbf{Q}\cdot\mathbf{a}_2}-\mathrm{e}^{iN_2\mathbf{Q}\cdot\mathbf{a}_2}}\mathrm{e}^{iN_1\mathbf{Q}\cdot\mathbf{a}_1/2}\frac{\mathrm{e}^{iN_3\mathbf{Q}\cdot\mathbf{a}_3}-\mathrm{e}^{iN_3\mathbf{Q}\cdot\mathbf{a}_3}}{\mathrm{e}^{i\mathbf{Q}\cdot\mathbf{a}_3}-\mathrm{e}^{iN_3\mathbf{Q}\cdot\mathbf{a}_3}}$$

$$F_N(\mathbf{Q}) = \mathrm{e}^{i\mathbf{Q}\cdot(N_1\mathbf{a}_1+N_2\mathbf{a}_2+N_3\mathbf{a}_3)/2}\frac{\sin(N_1\mathbf{Q}\cdot\mathbf{a}_1)}{\sin(\mathbf{Q}\cdot\mathbf{a}_1)}\frac{\sin(N_2\mathbf{Q}\cdot\mathbf{a}_2)}{\sin(\mathbf{Q}\cdot\mathbf{a}_2)}\frac{\sin(N_3\mathbf{Q}\cdot\mathbf{a}_3)}{\sin(\mathbf{Q}\cdot\mathbf{a}_3)}$$

The intensity of the scattered beam is related to the square of the electric field. The first term is just a phase and the modulus of the Lattice sum is

$$|F_N(\mathbf{Q})| = \left|\frac{\sin(N_1\mathbf{Q}\cdot\mathbf{a}_1)}{\sin(\mathbf{Q}\cdot\mathbf{a}_1)}\frac{\sin(N_2\mathbf{Q}\cdot\mathbf{a}_2)}{\sin(\mathbf{Q}\cdot\mathbf{a}_2)}\frac{\sin(N_3\mathbf{Q}\cdot\mathbf{a}_3)}{\sin(\mathbf{Q}\cdot\mathbf{a}_3)}\right| \ . \qquad (3.17)$$

As can be seen in Figure3.6, the value of $|F_N(\mathbf{Q})|^2$ has a maximum at multiples of π and it is almost zero otherwise. So, for large values of N, Eq. 3.17 becomes a Dirac delta function:

$$|F_N(\mathbf{Q})|^2 \approx \sum_{\mathbf{G}} \delta(\mathbf{Q}-\boldsymbol{G}) \ . \qquad (3.18)$$

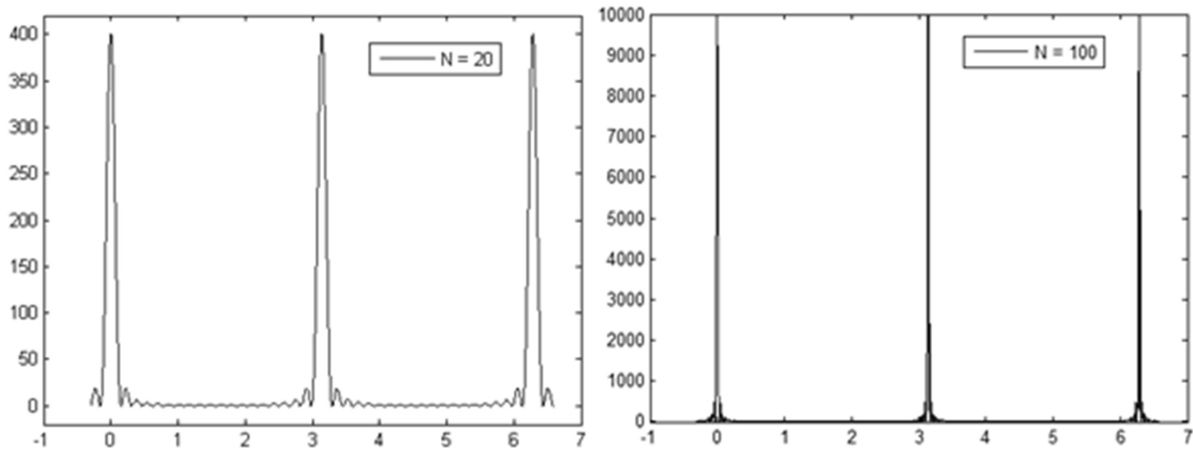

Figure 3.6: Graphic representation of the function $\left|\frac{\sin(N_1\mathbf{Q}\cdot\mathbf{a})}{\sin(\mathbf{Q}\cdot\mathbf{a})}\right|^2$ for a given $\mathbf{Q}$ and lattice parameter $\mathbf{a}$. When N becomes very large; the function becomes a Dirac delta function.

3.5 Unit cell Structure Factor

An example of calculation of the structure factor can be given for a face-centered cubic (FCC) crystal, with one of the simplest unit cells. Four vectors define all atoms on the unit cell of an FCC crystal. They are:

$$\mathbf{r}_1 = 0\,, \qquad \mathbf{r}_2 = \frac{1}{2}(\mathbf{a}_1 + \mathbf{a}_2)\,, \qquad \mathbf{r}_3 = \frac{1}{2}(\mathbf{a}_2 + \mathbf{a}_3)\ , \qquad \mathbf{r}_4 = \frac{1}{2}(\mathbf{a}_1 + \mathbf{a}_3)\ .$$

Our example of unit cell has atoms of the same type. Evaluating the first term of Eq. 3.12 in the Laue condition:

$$S^{\text{fcc}}(\mathbf{Q} = \mathbf{G}) = \sum_{j=1}^{4} f_j(\mathbf{G})\mathrm{e}^{i\mathbf{G}\cdot\mathbf{r}_j} = f_1(\mathbf{G})\mathrm{e}^{i\mathbf{G}\cdot\mathbf{r}_1} + f_2(\mathbf{G})\mathrm{e}^{i\mathbf{G}\cdot\mathbf{r}_2} + f_3(\mathbf{Q})\mathrm{e}^{i\mathbf{G}\cdot\mathbf{r}_3} + f_4(\mathbf{Q})\mathrm{e}^{i\mathbf{G}\cdot\mathbf{r}_4}$$

$$S^{\text{fcc}}(\mathbf{G}) = f_1(\mathbf{G}) + f_2(\mathbf{G})\mathrm{e}^{i\pi(h+k)} + f_3(\mathbf{G})\mathrm{e}^{i\pi(h+l)} + f_4(\mathbf{G})\mathrm{e}^{i\pi(k+l)}$$

$$S^{\text{fcc}}(\mathbf{G}) = f_1(\mathbf{G})(1 + \mathrm{e}^{i\pi(h+k)} + \mathrm{e}^{i\pi(h+l)} + \mathrm{e}^{i\pi(k+l)})$$

$$S^{\text{fcc}}(\mathbf{G}) = f_1(\mathbf{G}) \times \begin{cases} 4 & \text{if h, k, l are all even or all odd} \\ 0 & \text{otherwise.} \end{cases}$$

The fact that $F^{\text{fcc}}(\mathbf{G})$ is zero for some h, k, l leads to forbidden reflections for the crystal. As an example, the (1,0,0) reflection, which is the shortest reciprocal lattice vector, has a vanishing structure factor, since h is odd, but k and l are even. For different types of lattices, we will have different selection rules. For a trigonal lattice, which is the case of our sample; the permitted reflections are the ones whose $2\mathrm{h} + \mathrm{k} + \mathrm{l} = 3\mathrm{n}$, where n is an integer.

So, the X-ray scattering intensity for a real crystal is composed of these two sums, the form factor reflects the size and shape of the crystal yielding the width and shape the diffraction peaks and their measured intensity. The structure factor reflects the type of crystal, its symmetries, determining which peaks will appear in a diffractogram with a given intensity.

3.6 Crystal Truncation Rod Scattering

In section 3.4 it was shown that for an infinite three-dimensional crystal, the Laue condition $\mathbf{Q} = \mathbf{G}$ leads the Form factor into a Dirac delta function. The case of a finite crystal is a little different. When one cleaves the crystal a surface is formed. The Laue condition does not need to be fully satisfied anymore; there can be intensity even out of the Bragg peaks. The cleavage of a crystal allows the appearance of Crystal Truncation Rods Scattering (CTRS) in reciprocal space. These Crystal Truncation Rods (CTRs) can be understood as paths along reciprocal space where the X-ray intensity is present due to the existence of a truncated semi-infinite crystal (see Figure 3.7).

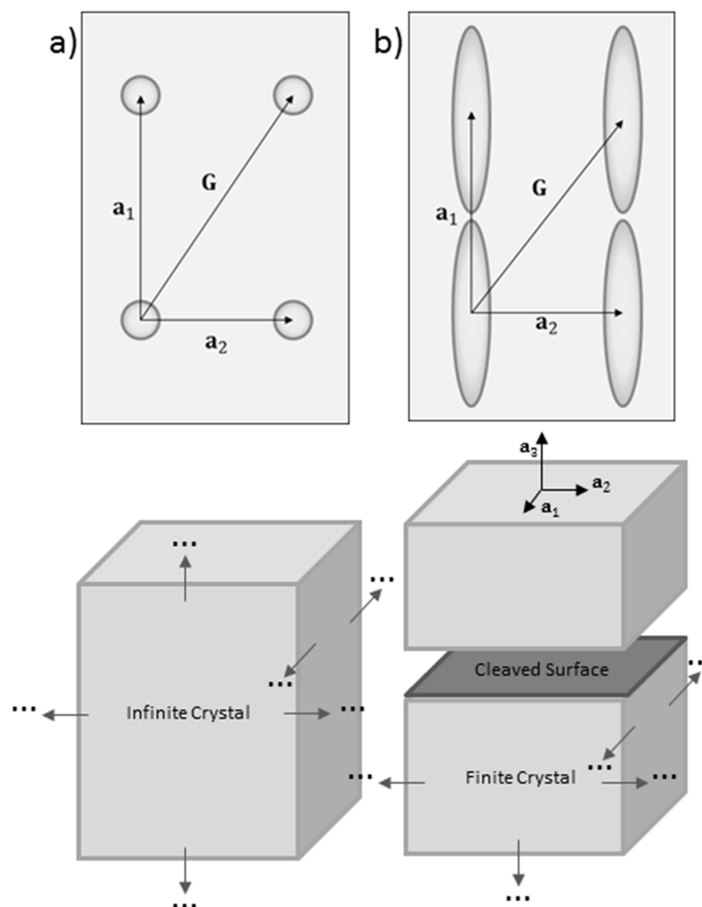

Figure 3.7: Maps in reciprocal space of an infinite (a) and a cleaved (b) crystal. The cleavage in (b) produces a surface, leading to streaks of scattering, the crystal truncation rods.

When the X-ray beam strikes a sample, it crosses a specific surface. In the two orthogonal directions parallel to the surface the crystal can be considered infinite for intensity calculation purposes. In these two directions, the Form factor is still a Dirac Delta function. Along the direction normal to the surface one obtains

$$F^{\mathrm{CTR}} = A(\mathbf{Q}) \sum_{n=0}^{\infty} \mathrm{e}^{i\mathrm{Q}_z \mathrm{a}_3 n} = \frac{A(\mathbf{Q})}{1 - \mathrm{e}^{i\mathrm{Q}_z \mathrm{a}_3}} \ , \tag{3.19}$$

where $A(\mathbf{Q})$ is the scattering amplitude for a layer of atoms. The intensity distribution along the crystal truncation rod is

$$I^{\mathrm{CTR}} = \left|F^{\mathrm{CTR}}\right|^2 = \frac{|A(\mathbf{Q})|^2}{(1 - \mathrm{e}^{i\mathrm{Q}_z \mathrm{a}_3})(1 - \mathrm{e}^{-i\mathrm{Q}_z \mathrm{a}_3})} = \frac{|A(\mathbf{Q})|^2}{4\sin^2(\mathrm{Q}_z \mathrm{a}_3/2)} \ . \tag{3.20}$$

An even more realistic calculation considers the absorption of X-rays. This absorption can be modeled using a factor β, where $\mathrm{e}^{-\beta}$ represents the decease of the X-ray beam intensity by one atomic layer. The Form factor with the absorption factor is given by

$$F^{\mathrm{CTR}} = A(\mathbf{Q}) \sum_{n=0}^{\infty} \mathrm{e}^{i\mathrm{Q}_z \mathrm{a}_3 n} \mathrm{e}^{-\beta n} = \frac{A(\mathbf{Q})}{1 - \mathrm{e}^{i\mathrm{Q}_z \mathrm{a}_3} \mathrm{e}^{-\beta}} \tag{3.21}$$

and the intensity is

$$I^{\mathrm{CTR}} = \left|F^{\mathrm{CTR}}\right|^2 = \frac{|A(\mathbf{Q})|^2}{(1 - \mathrm{e}^{i\mathrm{Q}_z \mathrm{a}_3} \mathrm{e}^{-\beta})(1 - \mathrm{e}^{-i\mathrm{Q}_z \mathrm{a}_3} \mathrm{e}^{-\beta})} \ . \tag{3.22}$$

In Figure 3.8, we show the effect of absorption in CTR. Analyzing Equations 3.20 and 3.22, the first equation (with no absorption) is valid away from the Bragg peaks. The second equation is more appropriate for Bragg peaks, where the calculated intensity no longer diverges.

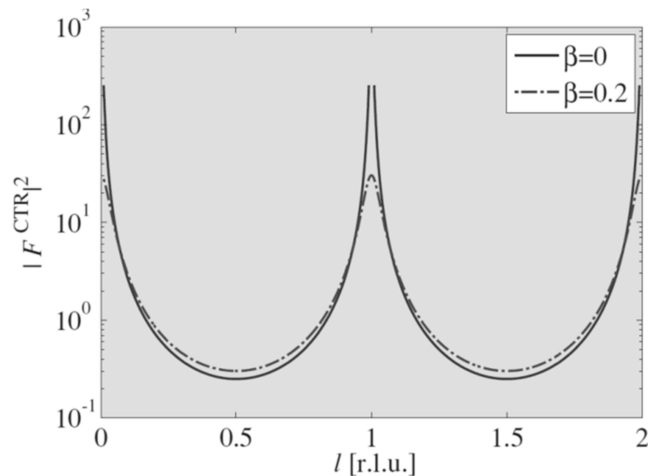

Figure 3.8: Graphic representation of the intensity of a crystal truncation rod. The straight blue line

represents the case of no absorption, diverging at the Bragg peak. The red dotted line represents the case of strong absorption. Normally, β is of the order of 10^{-5}. From [36].

With this mathematical treatment for the diffraction phenomena resulting in truncation rods, we have the tools to calculate the theoretical expected intensity for our sample and compare with our measurements. The experimental setup used in our experiment is shown in the next section.

3.7 Experimental Setup

In Figure3.9 we show a picture of the diffractometer located at Beamline XRD2 of the Brazilian Synchrotron Light Laboratory (Laboratório Nacional de Luz Síncroton - LNLS) in Campinas/SP, which was used for our experiment.

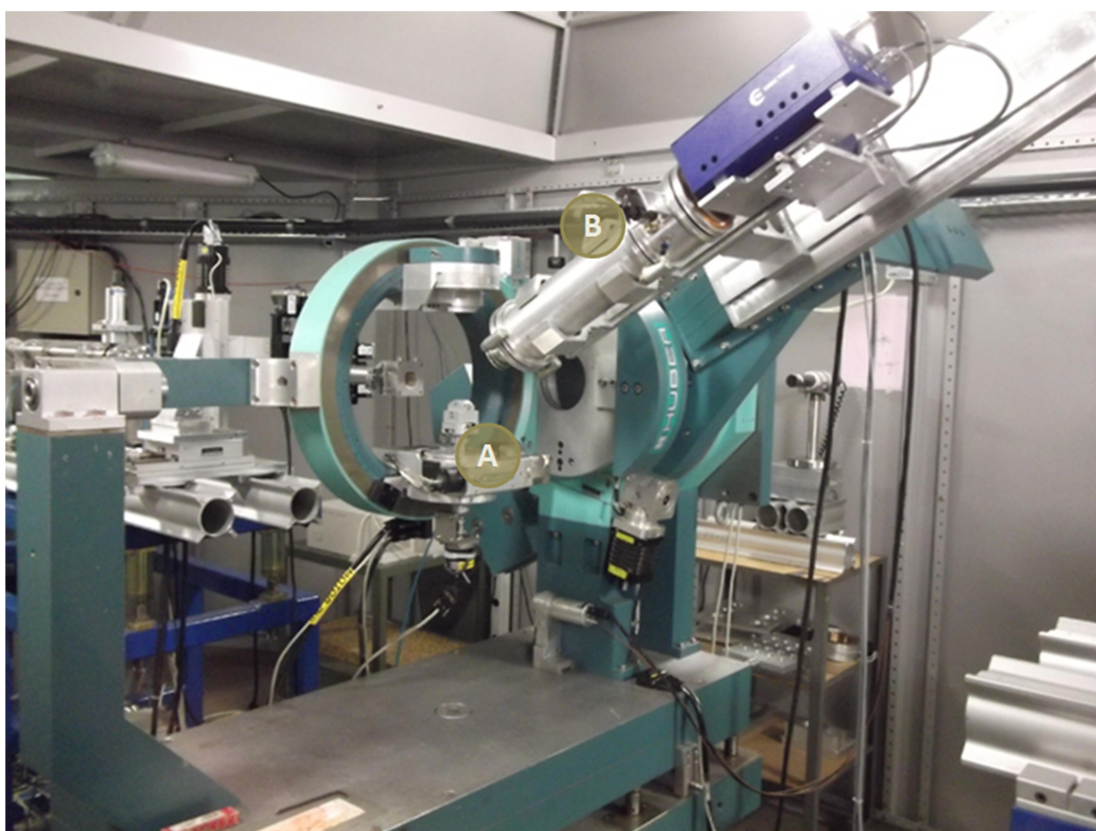

Figure 3.9: A picture of the diffractometer in the XRD2 Beamline at LNLS.

The X-ray beam, with energy of 10 keV shines a crystal sample at position A, and the detector at position B can move along the vertical direction to collect the scattered beam.

There are three more degrees of freedom of the sample holder to move and align the sample. An example of measured intensity is shown in Figure 3.10.

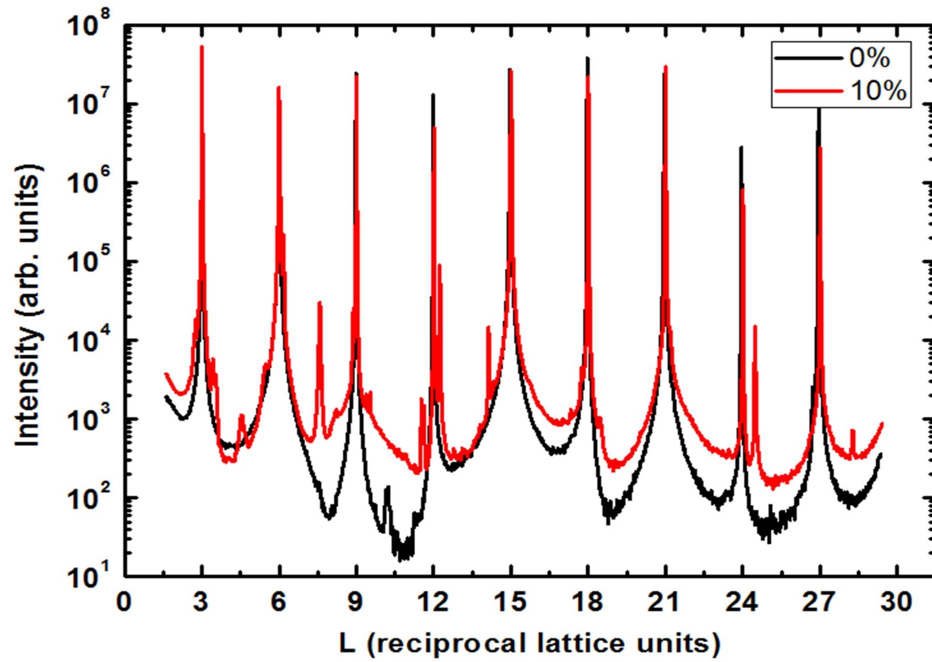

Figure 3.10: Example of a Crystal Truncation Rod measured by the diffractometer at Beamline XRD2 of LNLS. The graph shows the 00L CTR for two samples: A pure Bi_2Se_3 crystal and a Bi_2Se_3 crystal doped with 10% of aluminum.

4 - Scanning Tunneling Microscopy and Spectroscopy

The Scanning Tunneling Microscope was invented by Gerd Binnig and Heinrich Rohrer in 1981. They won the Nobel Prize in 1986 "for their design of the scanning tunneling microscope". Scanning Tunneling Microscopy (STM) is based on the quantum phenomenon of tunneling. A conducting tip is positioned closed to a conducting sample. If the tip approaches the surface, we are able to establish a tunneling current that is controlled by a feedback system attached to a computer.

This invention has become a unique technique to study the surface of materials at the atomic level. Today, atomic resolution is usually achieved with this equipment in university laboratories. Another important role of this kind of microscopy is that it can measure the local density of states of a material, as we will be shown later.

This chapter is divided in 7 sections: the first one shows the simple model for tunneling through a one dimensional square potential; section 2 shows the operation of the STM; sections 3 to 5 cover a more precise quantum approach to tunneling phenomena of the STM; section 6 covers Scanning Tunneling Spectroscopy (STS) and section 7 shows the experimental setup of our experiment.

4.1 Tunneling through a one-dimensional square potential

One of the most surprising differences between quantum and classical mechanics is related to the phenomenon of quantum tunneling. One imagines a particle, an electron for example, free in space when it faces a potential barrier. If the electron has less energy than the barrier, classically, it cannot pass to the other side. But in quantum mechanics this can happen [38]. First, one takes a look at the one-dimensional time-independent Schrödinger equation of an electron in a potential $U(x)$:

$$-\frac{\hbar^2}{2m}\frac{d^2}{dx^2}\Psi(x) + U(x)\Psi(x) = E\Psi(x) \ . \tag{4.1}$$

Where $\Psi(x)$ is the wave function of the electron, ħ is the Planck constant and E its energy. The potential barrier, represented in Figure 4.1, can be written as

$$U(x) = \begin{cases} 0 & x < 0 \\ V_0 & 0 < x < a \\ 0 & x > a \end{cases} . \quad (4.2)$$

Where V_0 is the constant value of the potential and a is the width of the barrier. The solution of Eq. 4.1 outside the barrier, in the classically allowed region, is

$$\Psi(x) = \Psi(0)\mathrm{e}^{\pm isx} , \quad (4.3)$$

where $s = \sqrt{2mE}/\hbar$ is the wavevector of the electron. The solution inside the barrier is given by

$$\Psi(x) = \Psi(0)\mathrm{e}^{-kx} \quad (4.4)$$

with $k = \sqrt{2m(V_0 - E)}/\hbar$. Looking at the Eq. 4.4 we note that the wavefunction is non-zero inside the potential barrier. The density of probability of finding the electron at some position is given by the square modulus of the wavefunction at this position. It is obvious that if the electron can be found inside the barrier, it can cross it and can be found on the other side.

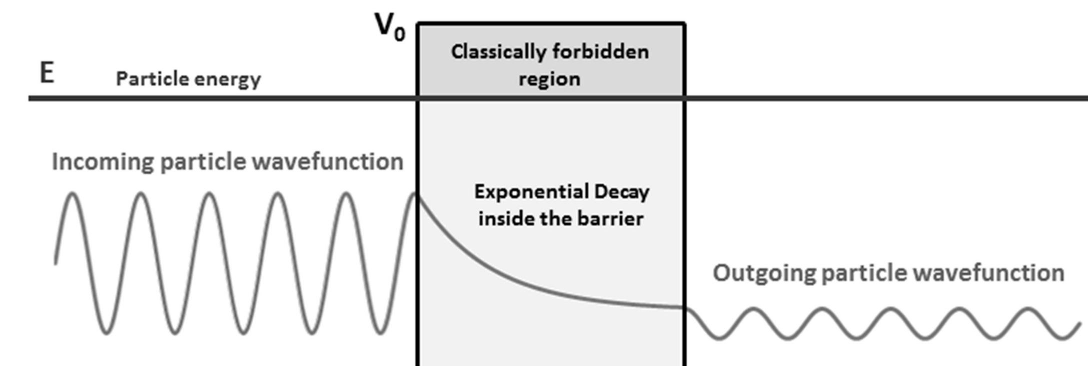

Figure 4.1: Representation of the wavefunction in the three regions. An electron with energy $E < V_0$ placed in the potential $U(x)$ (black).

The tunneling phenomenon consists in electrons crossing potential barriers with very small thicknesses. One can establish a tunneling current across the barrier by applying a voltage between the two sides. An important definition in the tunneling phenomena is the relationship between the incident and the transmitted wavefunctions. The transmission coefficient is given by

$$\mathrm{T} \approx \frac{4E(V_0 - E)}{V_0^2}\mathrm{e}^{-2ka} . \quad (4.5)$$

The tunneling current is related to the transmission coefficient. So it deeply depends on thickness of the barrier. That dependence is used by the Scanning Tunneling Microscope to measure the distance between a conducting tip and the sample separated by a vacuum barrier.

4.2 The Scanning Tunneling Microscope

The Scanning Tunneling Microscope was invented using the concept of tunneling described above. It can measure the tunneling current between a tip and a sample separated by a vacuum barrier.

The basic array of an STM microscope (figure 4.2) is composed by an assembly of an electronic feedback system which controls the distance between a tip (normally made of Tungsten or a Platinum-Iridium alloy) and the surface of the sample. If one applies a bias voltage on the tip, when it reaches a very small distance to the sample, a tunneling current appears. This tunneling current exhibits a very strong dependence on the tip-sample distance as was shown in equation 4.5.

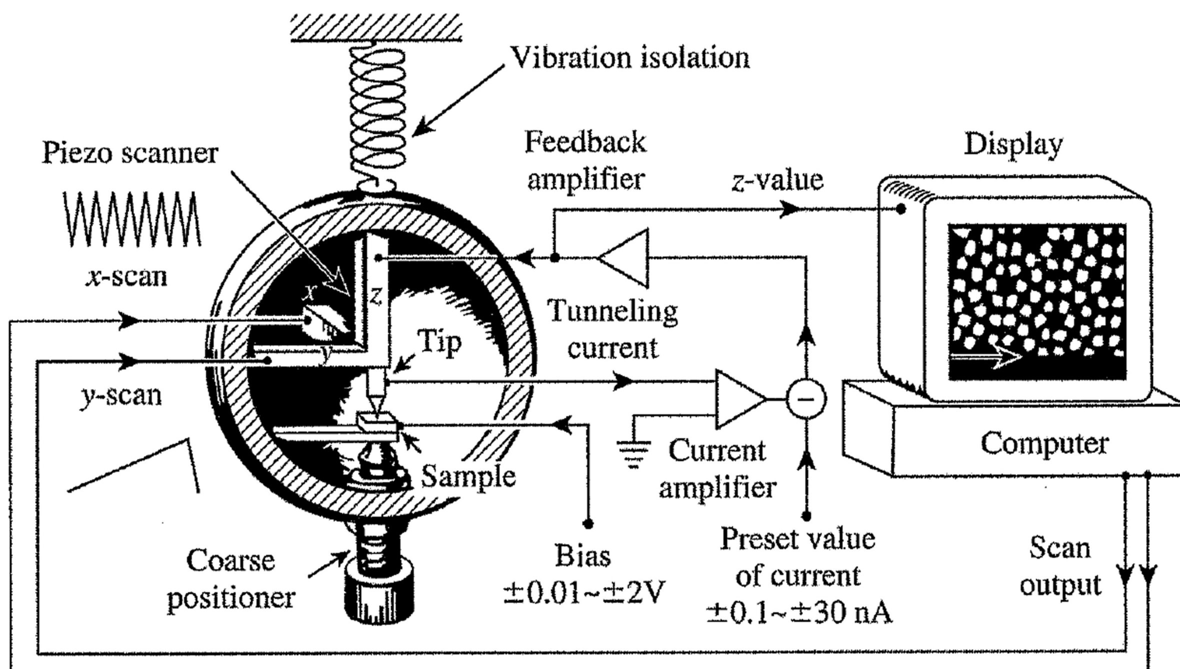

Figure 4.2: The scanning tunneling microscope. From [39].

A piezoelectric device attached to the tip enables it to move vertically to control the distance to the sample and, of course, the tunneling current (z-direction of figure 4.2). This piezoelectric device is connected to the feedback system which is used to maintain the current constant. Depending on the current wanted, the piezo-feedback system can keep that current by changing the distance between tip and sample.

The STM also has two more piezoelectric moving devices (x and y), both perpendiculars to the z-direction, which are used to scan the sample. By moving the tip in the x and y directions and maintaining the tip-sample distance constant, one can produce a two-dimensional map of the topography of sample. In the following sections we will present more precise calculations to describe this process. It is also important to say that we need a vibration-free environment to use the equipment with success. Sometimes we also want ultra-high vacuum (~10^{-10} mBar) and low temperature (5 K) ambient. These values are easily obtained in our laboratory at UFMG. An STM atomic-resolution image done in our laboratory is shown in Figure 4.3.

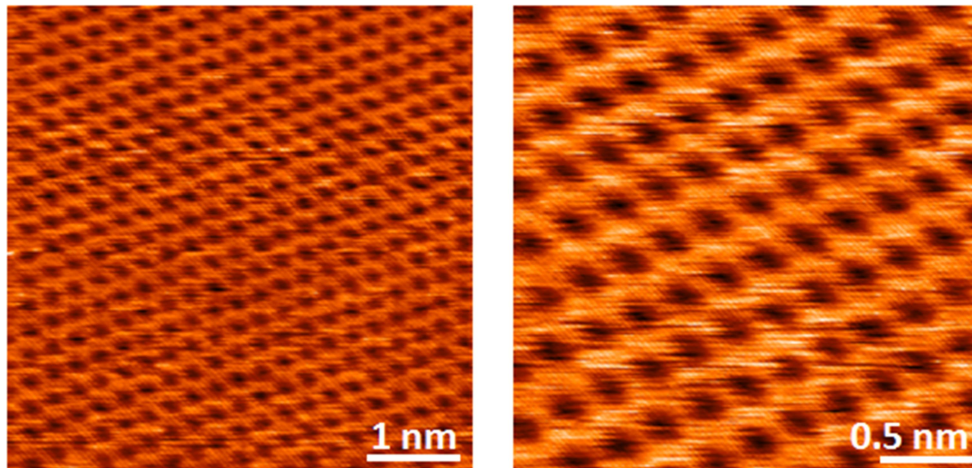

Figure 4.3: STM images of highly-oriented pyrolytic graphite obtained at the Nanoscopy Laboratory (UFMG). The images were obtained with a current of 900pA and bias voltage of 200mV.

4.3 Landauer Theory of tunneling

In section 4.1 we presented the tunneling phenomenon in its simplest approximation. To explain in more detail the dependence of the tunneling current (or more specifically, the tunneling conductance) on the tip-sample distance one needs to recur to the Landauer theory [40]. In 1957, Landauer developed a theory about the absolute value of the tunneling conductance based on a one-dimensional semi-classical model, and predicted the existence of a conductance quantum.

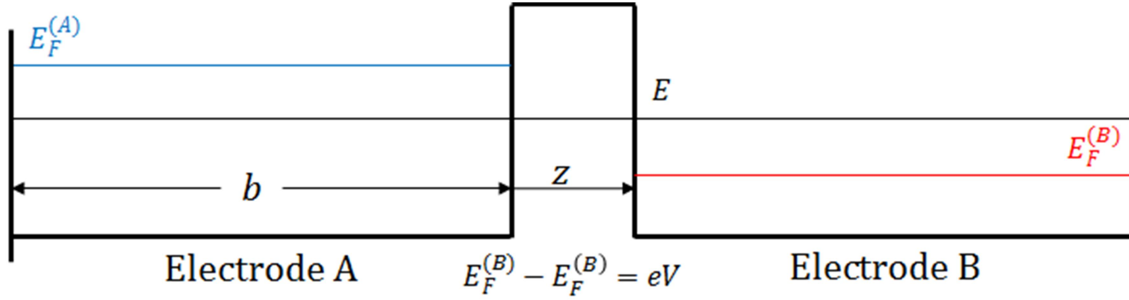

Figure 4.4: The two electrodes of Landauer Theory. Sample and tip are described as a perfect one-dimensional potential well, separately by a potential barrier. The bias voltage between the two electrodes is equal to the difference of the Femi levels of them. The tunneling can take place for electrons with energy levels between them.

The two electrodes represent sample and tip, as shown in Figure 4.4. The first assumption of Landauer is that the electrodes can be described by a one-dimensional free electron gas in an ideal square potential well. If the width of electrode A is b, then the wavefunction and the its energy eigenvalue are respectively given by

$$\Psi_n(z) = \sqrt{\frac{2}{b}} \sin\frac{n\pi z}{b} \quad \text{and} \tag{4.6a}$$

$$\mathrm{E} = \frac{\hbar^2}{2m}\left(\frac{n\pi}{b}\right)^2 \quad , \tag{4.6b}$$

where n is an integer. From equation 4.6b one can obtain the density of electrons per unit of energy per unit of length $\rho(E)$, which is

$$\rho(E) = \frac{2}{b}\frac{\partial n}{\partial E} = \frac{2}{\pi\hbar v} \ , \tag{4.7}$$

where $v = \sqrt{\frac{2E}{m}}$ is the classical velocity of the electron. The current arriving at the barrier junction can be expressed by

$$I_{in} = \frac{1}{2} ev\rho(E_F)\left(E_F^{(A)} - E_F^{(B)}\right) \quad , \tag{4.8}$$

where e is the electron charge, $E_F^{(A)}$ the Fermi level energy on the electrode A and $E_F^{(B)}$ the Fermi level energy on the electrode B. Since $E_F^{(A)} - E_F^{(B)} = eV$, and using the value of $\rho(E_F)$ from Eq. 4.7, the dependence of I_{in}on the bias voltage V is given by

$$I_{in} = \frac{e^2}{\pi\hbar} V \ . \tag{4.9}$$

The tunneling current is given by $I_t = TI_{in}$. The tunneling current is directly proportional to the bias voltage, leading to the conductance of the quantum tunneling:

$$G = \frac{I_t}{V} = \left(\frac{e^2}{\pi\hbar}\right)T \ . \tag{4.10}$$

Where $e^2/\pi\hbar$ is called the conductance quantum.

Landauer theory provides us the direct dependence between the conductance G and the barrier distance a, provided by T. The theory also shows the existence of conductance quantum. Both exponential dependence and the conductance quantum are shown in Figure 4.5.

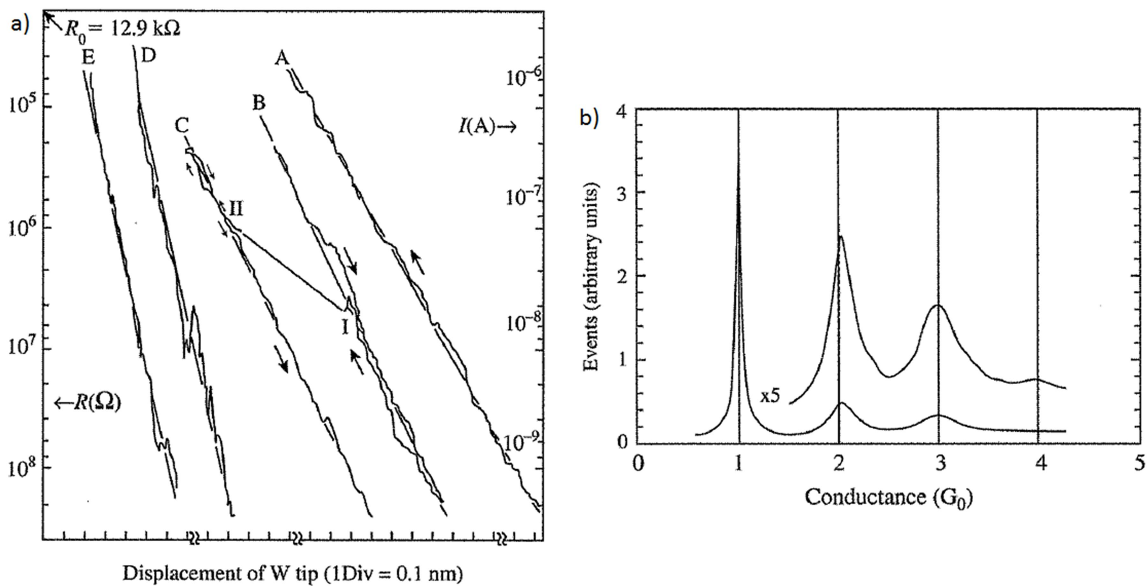

Figure 4.5: a) A historical experiment to establish the relationship between tunneling conductance and tip-sample distance. The exponential dependence I(V) was observed over 4 orders of magnitude. From [41]. b) Statistical results of experimental observation of conductance quantum. From [42].

4.4 Barden Theory

The theory of Landauer by itself gives us the tip-sample dependence of the tunneling current. This theory does not explain entirely the effect of scanning tunneling microscopy, which depends on the relationship between the tunneling conductance and the density of states of both sample and tip. The theory developed by Bardeen [43] can provide spectroscopic information about the density of states, deriving a more detailed equation for the tunneling current.

Imagine two electrodes far away from each other as shown in Figure 4.6a. Bardeen solved the Schrodinger equation for the two regions separately. When the electrodes approach each other, tunneling takes place. He used perturbation theory to determine the tunneling by the two electrodes wavefunctions.

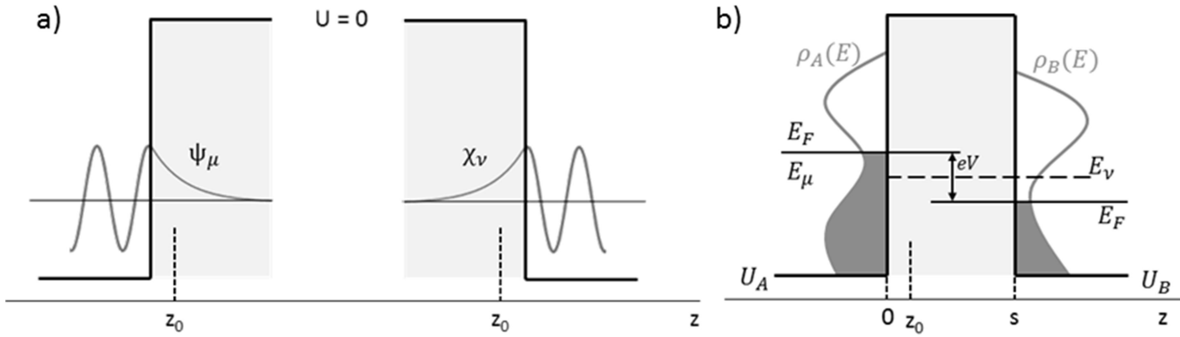

Figure 4.6: The Bardeen tunneling theory in 1D. a) Considering the two electrodes far from each other, wavefunctions decay into the vacuum. b) Bringing them together, the tunneling takes place.

If the two electrodes are far away from each other, the wavefunction on electrode A is described by the Schrodinger equation:

$$i\hbar\frac{\partial \mathbf{\Psi}}{\partial t} = \left[-\frac{\hbar^2}{2m}\frac{\partial^2}{\partial z^2} + U_A\right]\mathbf{\Psi} \ , \tag{4.11}$$

where U_A is the potential in electrode A and $\mathbf{\Psi}$ depends on both spatial and time coordinates. Considering the potential independent of time, equation 4.11 becomes the time-independent Schrodinger equation

$$E_\mu\psi_\mu = \left[-\frac{\hbar^2}{2m}\frac{\partial^2}{\partial z^2} + U_A\right]\psi_\mu \tag{4.12}$$

with $\mathbf{\Psi} = \psi_\mu e^{-iE_\mu t/\hbar}$, where ψ_μ only depend on the spatial coordinate and E_μ is this wave function energy. For the electrode B, similar equations like in 4.11 and 4.12 can be derived with potential U_B:

$$i\hbar\frac{\partial \mathbf{\Psi}}{\partial t} = \left[-\frac{\hbar^2}{2m}\frac{\partial^2}{\partial z^2} + U_B\right]\mathbf{\Psi} \tag{4.13}$$

and

$$E_\nu\psi_\mu = \left[-\frac{\hbar^2}{2m}\frac{\partial^2}{\partial z^2} + U_B\right]\chi_\nu \quad . \tag{4.14}$$

with $\mathbf{\Psi} = \chi_\nu \mathrm{e}^{-iE_\nu t/\hbar}$, where χ_ν only depends on the spatial coordinate and E_ν is this wave function energy. When the two electrodes approach each other, the Schrodinger equation of the new system will be

$$i\hbar\frac{\partial\mathbf{\Psi}}{\partial t} = \left[-\frac{\hbar^2}{2m}\frac{\partial^2}{\partial z^2} + U_A + U_B\right]\mathbf{\Psi} \ . \tag{4.15}$$

The first assumption made by Bardeen was that for the new system, the states on the electrode A will evolve differently from equation 4.11. Bardeen assumed that the wavefunctions calculated by Eq. 4.11 have a probability of transferring to the electrode B as given by

$$\mathbf{\Psi} = \psi_\mu \mathrm{e}^{-iE_\mu t/\hbar} + \sum_{\nu=1}^{\infty} c_\nu(t)\chi_\nu \mathrm{e}^{-iE_\nu t/\hbar} \ , \tag{4.16}$$

where $c_\nu(t)$ are the coefficients to be determined by equation 4.15 and $c_\nu(0) = 0$. The basic assumption in Bardeen theory is that these two states are approximately orthogonal,

$$\int \psi_\mu^* \chi_\nu d^3\mathbf{r} \cong 0 \ . \tag{4.17}$$

Equation 4.16 is still normalized since $c_\nu(t)$ is infinitesimal for any ν. Combining equation 4.15 and 4.16 one obtains

$$i\hbar\sum_{\nu=1}^{\infty}\frac{dc_\nu(t)}{dt}\chi_\nu \mathrm{e}^{-iE_\nu t/\hbar} = U_B\psi_\mu \mathrm{e}^{-iE_\mu t/\hbar} + U_A\sum_{\nu=1}^{\infty} c_\nu(t)\chi_\nu \mathrm{e}^{-iE_\nu t/\hbar} \ . \tag{4.18}$$

The second term in the right-hand side of equation 4.18 is a second order perturbation, so we can approximate equation 4.18 to

$$i\hbar\frac{dc_\nu(t)}{dt} = \int_{z>z_0} \psi_\mu U_B \chi_\nu^* d^3\mathbf{r}\ \mathrm{e}^{-i(E_\mu - E_\nu)t/\hbar} \ . \tag{4.19}$$

This integral can be evaluated only in the region $z > z_0$ because U_B is zero otherwise. This defines the tunneling matrix element as

$$M_{\mu\nu} = \int_{z>z_0} \psi_\mu U_B \chi_\nu^* d^3\mathbf{r} \ . \tag{4.20}$$

Integrating equation 4.19 one obtains

$$c_\nu(t) = M_{\mu\nu}\frac{\mathrm{e}^{-i(E_\mu - E_\nu)t/\hbar} - 1}{E_\mu - E_\nu} \ . \tag{4.21}$$

Starting from the μ-state on the electrode A, the probability of having the ν-state of the electrode B at time t is given by

$$p_{\mu\nu}(t) = |c_\nu(t)|^2 = \left|M_{\mu\nu}\right|^2 \frac{4\sin^2[(E_\mu - E_\nu)t/2\hbar]}{(E_\mu - E_\nu)^2} \ . \tag{4.22}$$

One can define function $f(t)$ as

$$f(t) = \frac{4\sin^2[(E_\mu - E_\nu)t/2\hbar]}{(E_\mu - E_\nu)^2} \ . \tag{4.23}$$

This function has a maximum for $E_\mu = E_\nu$ and becomes zero rapidly for $E_\mu \neq E_\nu$. This leads to the condition of elastic tunneling. The tunneling current depends on how many states in electrode A can tunnel into the electrode B. The total probability is calculated integrating equation 4.22 over all energies and using the concept of density of states, $\rho(E)$, i.e. the density of states that exist in the electrode with energy E, resulting in

$$P_{\mu\nu}(t) = \frac{2\pi}{\hbar}\left|M_{\mu\nu}\right|^2 \rho_B(E_\mu)t \ . \tag{4.24}$$

The tunneling current is related to the number of available states given by the density of states on A and the interval of energies between the two electrodes. If the density of states of both electrodes does not vary appreciably near the Fermi level:

$$I = \frac{4\pi e^2}{\hbar}\left|M_{\mu\nu}\right|^2 \rho_A(E_\mu)\rho_B(E_\mu)V \ . \tag{4.25}$$

This is the Bardeen formula for the tunneling current which also leads to the tunneling conductance. $M_{\mu\nu}$ can be evaluated using equations 4.12 and 4.14, and it only depends on the wavefunctions ψ_μ and χ_ν:

$$M_{\mu\nu} = \frac{\hbar^2}{2m} \int_{z=z_0} \left[\psi_\mu \frac{\partial \chi_\nu^*}{\partial z} - \chi_\nu^* \frac{\partial \psi_\mu}{\partial z}\right] dxdy \ . \tag{4.26}$$

If we are more interested in a spectroscopy study, i.e., the dependence of the tunneling current I on the bias voltage V, it is necessary to modify equation 4.25. The more general case gives

$$I = \frac{4\pi e^2}{\hbar}\int_{-\infty}^{\infty} [f(E_F - eV + \epsilon) - f(E_F + \epsilon)]\rho_A(E_F - eV + \epsilon)\rho_B(E_F + \epsilon)|M|^2 d\epsilon \ , \tag{4.27}$$

where $f(E)$ is the Fermi distribution function. If $k_B T$ is smaller than the energy resolution required for the experiment, equation 4.27 becomes

$$I = \frac{4\pi e^2}{\hbar}\int_{0}^{eV} \rho_A(E_F - eV + \epsilon)\rho_B(E_F + \epsilon)|M|^2 d\epsilon \ . \tag{4.28}$$

That is the general formula for the tunneling current by the Bardeen theory. In next section we have a model to calculate the density of states of the tip and the sample, relating them to the Spectroscopy experiment, called the Tersoff-Hamann model.

4.5 Tersoff-Hamann Model

Using Bardeen Theory, Tersoff and Hamann formulated a model to calculate the wavefunctions of the tip and sample in an STM [44]. The tip can be represented by a spherically symmetric object and the sample by a plane, as shown in Figure 4.7. The sample is at $z = 0$, and the tip has a center of curvature in $\mathbf{r}_0 = (0,0,z_0)$. The Schrodinger equation in the region between the tip and the sample is valid for the two wavefunctions and it is

$$-\frac{\hbar^2}{2m}\nabla^2\psi(\mathbf{r}) = \varphi\psi(\mathbf{r}) \ , \tag{4.29}$$

where φ is the work function of the sample. Using $K = \sqrt{2m\varphi}/\hbar$, it becomes

$$\nabla^2\psi(\mathbf{r}) = K^2\psi(\mathbf{r}) \ . \tag{4.30}$$

For the sample wavefunction, it can be resolved by a two-dimensional Fourier expansion,

$$\psi(\mathbf{r}) = \int d^2\mathbf{q} f(\mathbf{q})\, \mathrm{e}^{-\sqrt{\mathbf{q}^2+k^2}z+i\mathbf{q}\cdot\mathbf{x}} \ , \tag{4.31}$$

where $\boldsymbol{x} = (x,y)$ and $f(\boldsymbol{q})$ are the coefficients of the Fourier components of the sample surface at $z = 0$.

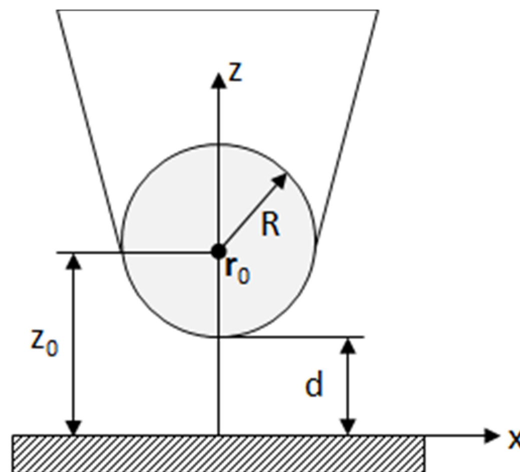

Figure 4.7: The Tersoff-Hamann model of the STM. The tip is modeled as a locally spherical object with a radius of curvature R centered at $\boldsymbol{r_0}$.

For the tip wavefunction, the assumption is that it is spherically symmetric, so equation 4.30 becomes

$$\frac{1}{r}\frac{d^2}{dr^2}[r\chi(r)] = k^2\chi(r) \ . \tag{4.32}$$

Up to a constant, in the region of $\mathrm{z} < \mathrm{z}_0$, the Fourier transform of the solution will be

$$\chi(r) = \frac{1}{2\pi}\int d^2\mathbf{p}\frac{\mathrm{e}^{-\sqrt{\mathbf{p}^2+k^2}(z-z_0)+i\mathbf{p}\cdot\mathbf{x}}}{\sqrt{\mathbf{p}^2+k^2}} \ . \tag{4.33}$$

Using equations 4.31 and 4.33 in equation Eq. 4.26 to calculate the value of M one obtains

$$M = \frac{\hbar^2}{2\pi m}\int d^2\mathbf{q}f(\mathbf{q})\,\mathrm{e}^{-\sqrt{\mathbf{q}^2+k^2}z_0} = \psi(\mathbf{r}_0) \ . \tag{4.34}$$

The integral values$\psi(\mathbf{r}_0)$, so in the Tersoff-Hamann model, M is directly proportional to the value of the sample wavefunction in the center of curvature $\mathbf{r}_0$ of the tip.

Now one can calculate the tunneling current. To do this, one considers four conditions:

1. The tip state is spherically symmetric;
2. The tunneling matrix element does not depend on any energy level;
3. The tip density of states is a constant over the energy interval of interest; and
4. The sample density of states does not vary appreciably in the interval of energy of k_BT.

So, starting from equation 4.28 which already considers (4):

$$I = \frac{4\pi e^2}{\hbar}\int_0^{eV} \rho_T(E_F - eV + \epsilon)\rho_S(E_F + \epsilon)|M|^2 d\epsilon$$

and using (2) and (3), we have:

$$I = \frac{4\pi e^2}{\hbar}\rho_T|M|^2\int_0^{eV} \rho_S(E_F + \epsilon)d\epsilon \ . \tag{4.35}$$

Using (1), $M = \psi(\mathbf{r}_0)$, so

$$I = \frac{4\pi e^2}{\hbar}\rho_T|\psi(\mathbf{r}_0)|^2\int_0^{eV} \rho_S(E_F + \epsilon)d\epsilon \ . \tag{4.36}$$

Now we can define $|\psi(\mathbf{r}_0)|^2\rho_S(E)$ as the local electronic density of states of the sample at the energy level E at the center of curvature of the tip:

$$\rho_S(E, \mathbf{r}_0) = |\psi(\mathbf{r}_0)|^2 \rho_S(E) \ . \tag{4.37}$$

So equation4.36 becomes

$$I = \frac{4\pi e^2}{\hbar} \rho_T \int_0^{eV} \rho_S(E_F + \epsilon, \mathbf{r}_0) d\epsilon \ . \tag{4.38}$$

Differentiating eq. 4.38 one obtains the tunneling conductance, which is directly proportional to the local electronic density of states:

$$G = \frac{dI}{dV} \propto \rho_S(E_F + eV, \mathbf{r}_0) \ . \tag{4.39}$$

This is the reason Scanning Tunneling Spectroscopy is such a powerful technique. Maintaining a constant tip-sample distance and measuring the tunneling current for different values of the tip voltage, one obtains information about the local electronic density of states of the surface of the sample. It is necessary to observe the 4 assumptions made above. (1) and (3) are obtained by a good preparation of the tip. (2) is an assumption about the STM theory and is often valid for most case. But for have a reliable measurement, (4) is obtained by working at low-temperatures to decrease $k_B T$.

4.6 Scanning Tunneling Spectroscopy with a Lock-In Amplifier

By turning down the electronic feedback, the STM can keep the tip-sample distance constant (if there is no vibration and thermal drift of the experimental setup). By varying the bias voltage between tip and sample one is able to measure the variation of the tunneling current. As seen in the previous section, the derivative dI/dV can gives us the Local Density of States of the sample (Eq. 4.39).

One way to acquire this dI/dV curve is to simply differentiate the $I(V)$ curve in a numerical procedure. This kind of approach is not desirable because the produced $I(V)$ curve is not a continuous set of acquired values. The tip measures the current for a value of voltage and then changes this voltage and measures the current again, resulting in a discrete measurement. This gives us non-desirable variations in the dI/dV curve, due to possible movements of the tip with respect to the surface. To suppress this difficulty one can use a Lock-In Amplifier which gives us the continuum derivative of the curve with the bonus of suppressed noise.

A Lock-In Amplifier is nothing more than an AC Voltmeter where one measures just the AC component in a given frequency and a given phase, suppressing all other signals one may have. A scheme of the Lock-In Amplifier is shown in Figure 4.8.

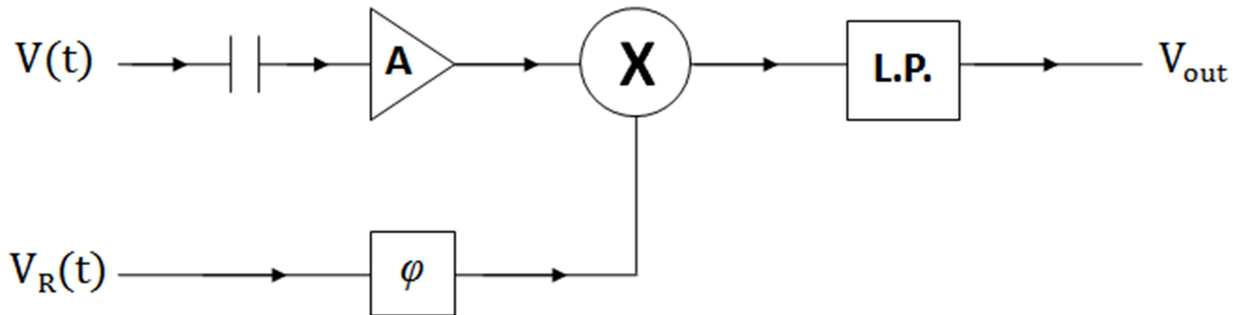

Figure 4.8: Block diagram of a phase sensitive Lock-In Amplifier. The input signal $V(t)$ passes through a capacitor, blocking any pre-existing DC offset, and is then amplified (A). The reference signal $V_R(t)$ passes through an adjustable phase-shifter (φ). These two results are then multiplied (X), and any resulting DC component is extracted by the low-pass (L.P.) filter.

Consider a sinusoidal signal which will be the input of our amplifier

$$V(t) = V_0 \sin(\omega t + \varphi) \ . \tag{4.40}$$

Suppose that we have available a reference signal

$$V_R(t) = \sin(\Omega t) \ . \tag{4.41}$$

What a Lock-In Amplifier does is to multiply these two signals resulting in

$$V(t)V_R(t) = \frac{V_0}{2}\{\cos[(\omega - \Omega)t + \varphi] - \cos[(\omega + \Omega)t + \varphi]\} \ . \tag{4.42}$$

When $\omega \neq \Omega$ this product oscillates in time with an average value of zero (zero DC component), but if $\omega = \Omega$, it has a DC component

$$V(t)V_R(t) = \frac{V_0}{2}\{\cos[\varphi] - \cos[2\Omega t + \varphi]\} \ . \tag{4.43}$$

If we are able to extract just the DC component of the output signal and adjusting $\cos\varphi$ to reach its maximum value one can have a direct measurement of V_0. The Lock-In amplifier technique is good because the output signal rejects the noises in a frequency different from that of the reference. A schematic of the STS experiment is shown in Figure 4.9.

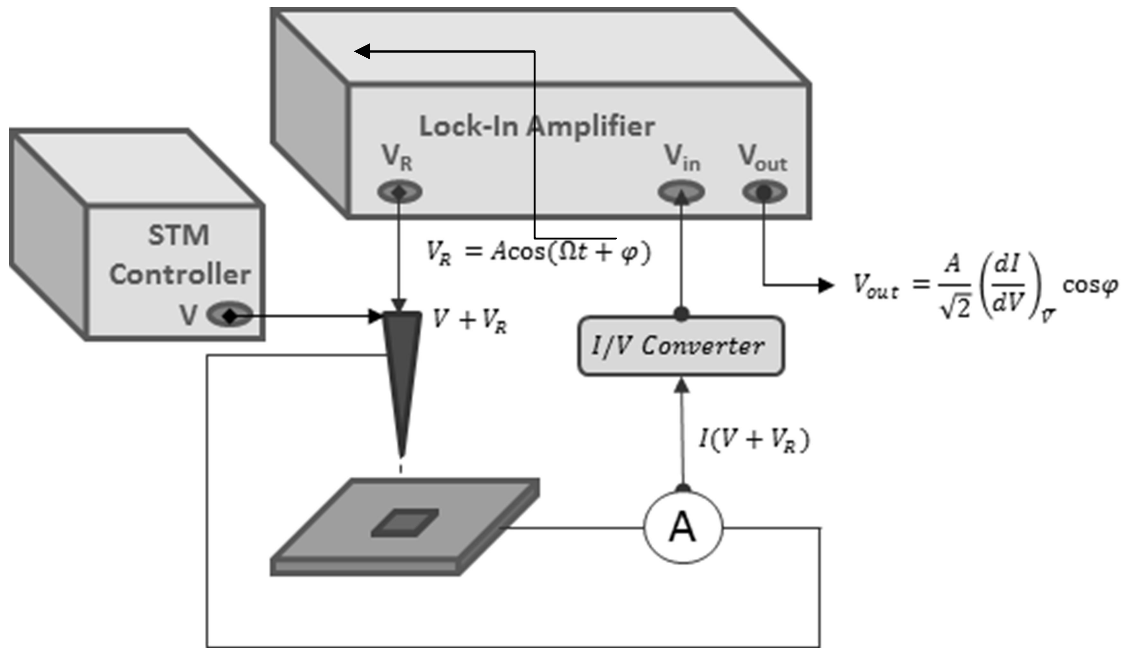

Figure 4.9: Schematic of the STS experiment with Lock-In Amplifier. A sinusoidal signal is added to the bias voltage V of the STM, the measured current $I(V)$ enters the Lock-In Amplifier and the output signal from the Lock-In represents the dI/dV value.

Looking at the Scanning Tunneling Spectroscopy problem, let us add a sinusoidal signal to the tip voltage, so $I(V)$ becomes

$$I(V) = I[V + A\sin(\Omega t + \varphi)] \ . \tag{4.44}$$

The tip voltage is now composed of a DC component (the bias voltage given by the STM) and an AC component we have added. The tunneling current will also have a DC and an AC component. If the amplitude of the signal added is too small when compared to the bias voltage, we can expand $I(V)$ into a Taylor series

$$I(V) = I(\bar{V}) + \left(\frac{dI}{dV}\right)_{\bar{V}} A\sin(\Omega t + \varphi) + O(A^2) \ . \tag{4.45}$$

Running this through the lock-in amplifier gives an output of

$$V_{out} \approx \frac{A}{\sqrt{2}}\left(\frac{dI}{dV}\right)_{\bar{V}} \cos\varphi \ . \tag{4.46}$$

In other words, the output signal given by the Lock-in Amplifier is the derivative of the $I(V)$ curve, proportional to the local density of states itself. In Figure 4.10, we show the difference between the dI/dV curves acquire within and without the Lock-in method.

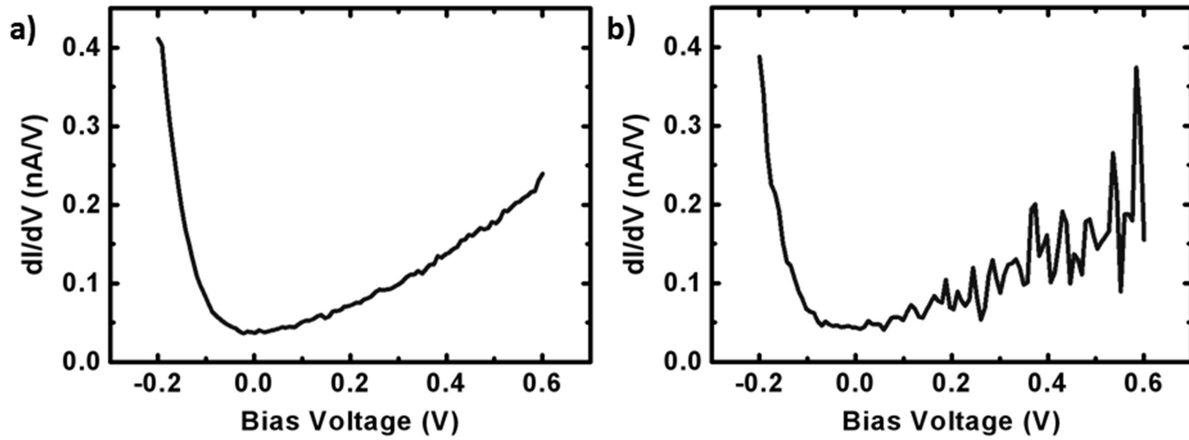

Figure 4.10: (a) dI/dV curve of the topological insulator Bi_2Se_3 acquired with a Lock-in Amplifier. (b) dI/dV acquired by differentiating the $I(V)$ curve with a numerical process. The lock-in process does not directly provide the tunneling conductance, but it suppresses most of the noise in it.

One final issue that we need to consider is due to the fact that the current varies dramatically with the tip-sample distance

$$I = I_0 \mathrm{e}^{-2kz}$$

This gives us different spectra for different distances when we measure the STS spectra. To circumvent this problem, we introduce a normalization to the tunneling conductance, as proposed by Feenstra et al [45], the normalized dynamic conductance

$$g_N(V) \equiv \frac{dI/dV}{\overline{I/V}} \ . \tag{4.47}$$

When necessary the normalized conductance may be shown instead of dI/dV.

4.7 Experimental Setup

The Scanning Tunneling Microscope used in our experiment is a Variable Temperature VT-STM manufactured by Omicron GmbH and located at the UHV Nanoscopy Laboratory at UFMG (Figure 4.11). The system has a vibration-isolation system (A) to suppress the mechanical vibrations on the building. The STM images were obtained in a vacuum chamber (B) pressure better than 1 x 10^{-10}mBar. The STS measurements were performed at 25K using a liquid helium transfer system (C) as shown in the figure below.

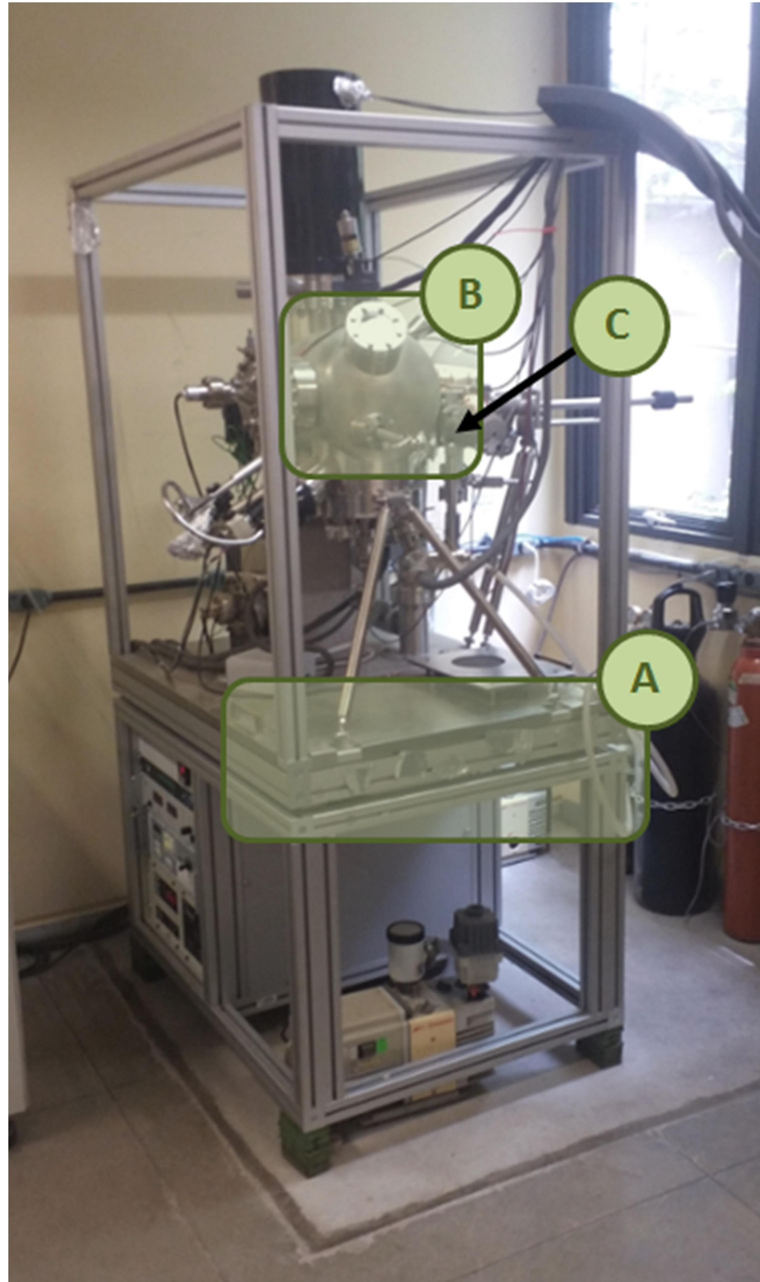

Figure 4.11: STM microscope at the UHV Nanoscopy Laboratory (UFMG). (A) The vibration-isolation system; (B) The vacuum chamber; (C) The narrow indicates the liquid helium transfer input.

5 - Results and Discussions

The STM technique combined with X-Ray Diffraction experiments, provide a complete set of information that covers the electronic and structural properties of conducting samples. Crystal Truncation Rods (CTRs) can be used to identify the presence of distinct phases in semi-infinite crystals with atomically flat surfaces, which are the suitable specimen type for STM. As shown in Section 2.5, our sample is a polyphase crystal with coexisting Bi_2Se_3-Bi_4Se_5 phases. Since the growth was carried out with a small lack of selenium, a non-stoichiometric Bi_2Se_3 crystal was obtained. Such configuration allows the formation of Bi-rich phases that must be formed from instability positions within the Bi_2Se_3 crystal.

In this chapter we show X-ray CTR measurements performed at the Brazilian Synchrotron Laboratory (Campinas/SP). Different phases of Bismuth Selenide were detected in our sample and compared to a real-time annealing CTR experiment, where the amount of non-stoichiometric Bi_2Se_3 phases was monitored along a temperature ramp. We also report Density Functional Theory (DFT) calculations, performed by Dr. Mário Sérgio de Carvalho Mazzoni (UFMG), to compare the band structure of these two phases, and to connect structural results to the electronic properties retrieved by STM/STS.

Scanning Tunneling Microscopy images of the original sample heated at 350°C were done, allowing the identification of the initial steps of formation of Bi_4Se_5 domains, providing their size and topography. Finally, Scanning Tunneling Spectroscopy (STS) measurements on this sample were performed at the stoichiometric and non-stoichiometric regions.

As discussed previously, STS provides information concerning the density of states of our sample. The correlation of structural and electronic properties is directly retrieved by combining STM and STS, assigning to each of the distinct phase their electronic behavior. Our STM measurements showed patterns of nanograins scattered along the sample surface. Some of these nanograins have step heights of less than 1nm, indicating of the formation of Bismuth bilayers, which were also studied by STS measurements.

5.1 X-Ray Scattering results

The X-ray experiments performed here were carried out at the XRD2 Beamline of the Brazilian Synchrotron (LNLS). Line scans in reciprocal space were taken with an X-ray beam of 10 keV with the sample positioned at a variable temperature furnace.

The van der Waals bonds that exist among the quintuple-layers (QLs) of Bi_2Se_3 are inherently weak, allowing the material to be easily exfoliated with the exposure of atomic planes. Figure 5.1 shows a simple scheme of the X-ray experiment. The sample was aligned in coplanar-specular condition, and scans performed with the detector moving along 2θ in real space with a coupled sample movement that fulfills Bragg's condition. With this type of alignment, one measures the 00L Crystal Truncation Rod (CTR) line in reciprocal space.

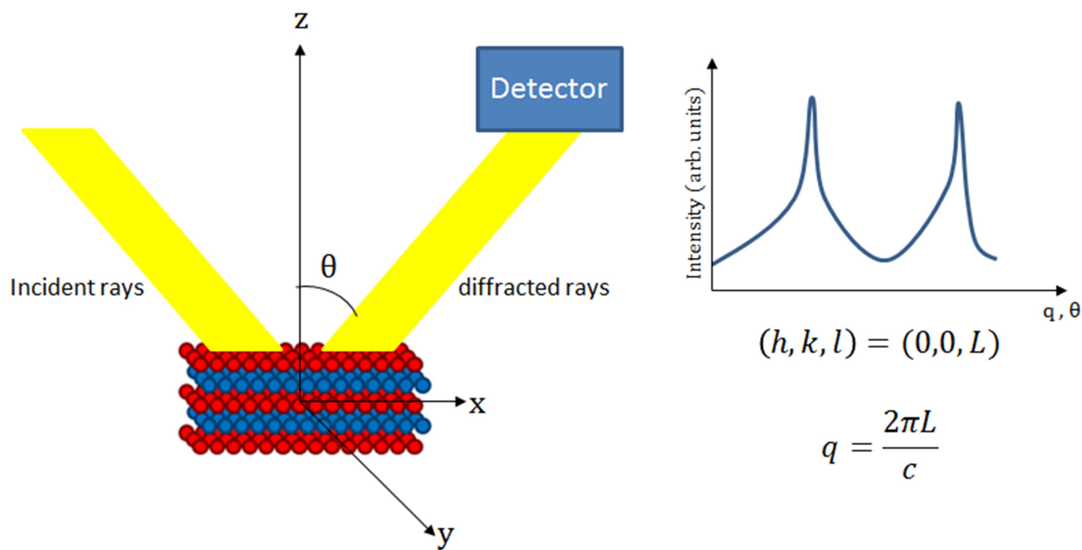

Figure 5.1: Sketch of the experimental setup mounted at Beamline XRD2 for XRD measurements. The X-ray beam impinges the sample with surface normal aligned in the z-direction. If the sample is rotated by an angle θ, and the detector moves twice this angle (2θ) with respect to the horizontal plane, measuring the diffracted intensity as function of the momentum transfer vector $q = (\frac{4\pi}{\lambda})\sin\theta$. The scan direction for the Bi_2Se_3/Bi_4Se_5 sample was chosen to lie along the 00L direction, where $q = 2\pi L/c$ (c is the out-of-plane lattice parameter and L the reciprocal space coordinate).

Several other CTR lines such as 01L, 10L, 20L, etc, can be measured following similar procures and knowing the crystalline structure of Bi_2Se_3. In Figure 5.2 we present results for the truncation rods 00L and 01L, both measured at room temperature. As one observes, some reflections are forbidden for the Bi_2Se_3 unit cell symmetry. For the 00L direction we only have the $(0,0,3n)$ peaks, where n is an integer. This rule is also observed at the 01L direction, where one observes only the $(0,1,3n-1)$ peaks.

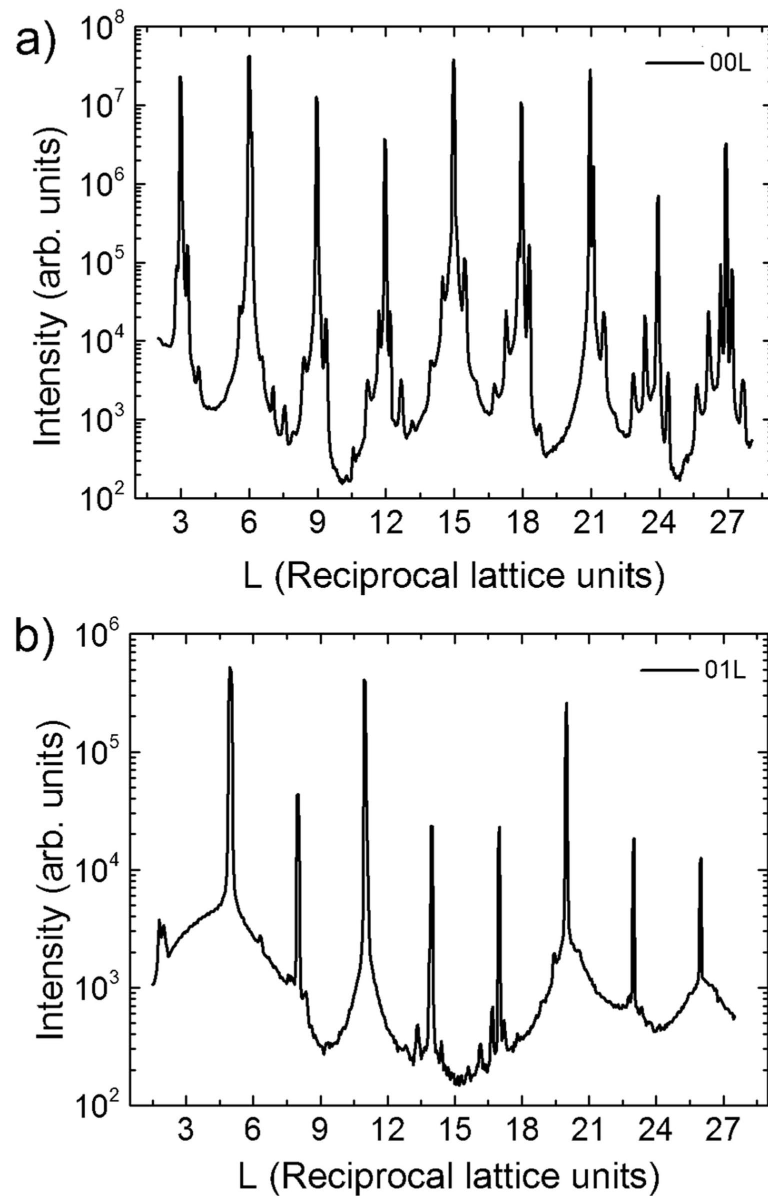

Figure 5.2: Crystal Truncation Rods of the Bi_2Se_3-Bi_4Se_5 sample at room temperature. a) CTR 00L. b) CTR 01L.

X-ray peaks additional to the stoichiometric Bi_2Se_3 can be seen along the 00L direction. As shown in Section 3.6, the quality of the Crystal Truncation Ro data is strongly related to the smoothness of the sample surface. Since a sample morphology with large atomically flat terraces is observed by STM the additional peaks (see Figure 5.3a) must correspond to the formation of a new phase within the material. This phase must possess periodicity in the z-direction, but different lattice parameter with respect to Bi_2Se_3 (it was later identified as Bi_4Se_5). We have centered our analysis efforts at the 00L truncation rod. Some of the data obtained on the in-situ annealing experiment at the 00L CTR line is shown in Fig. 5.3b for different temperature values.

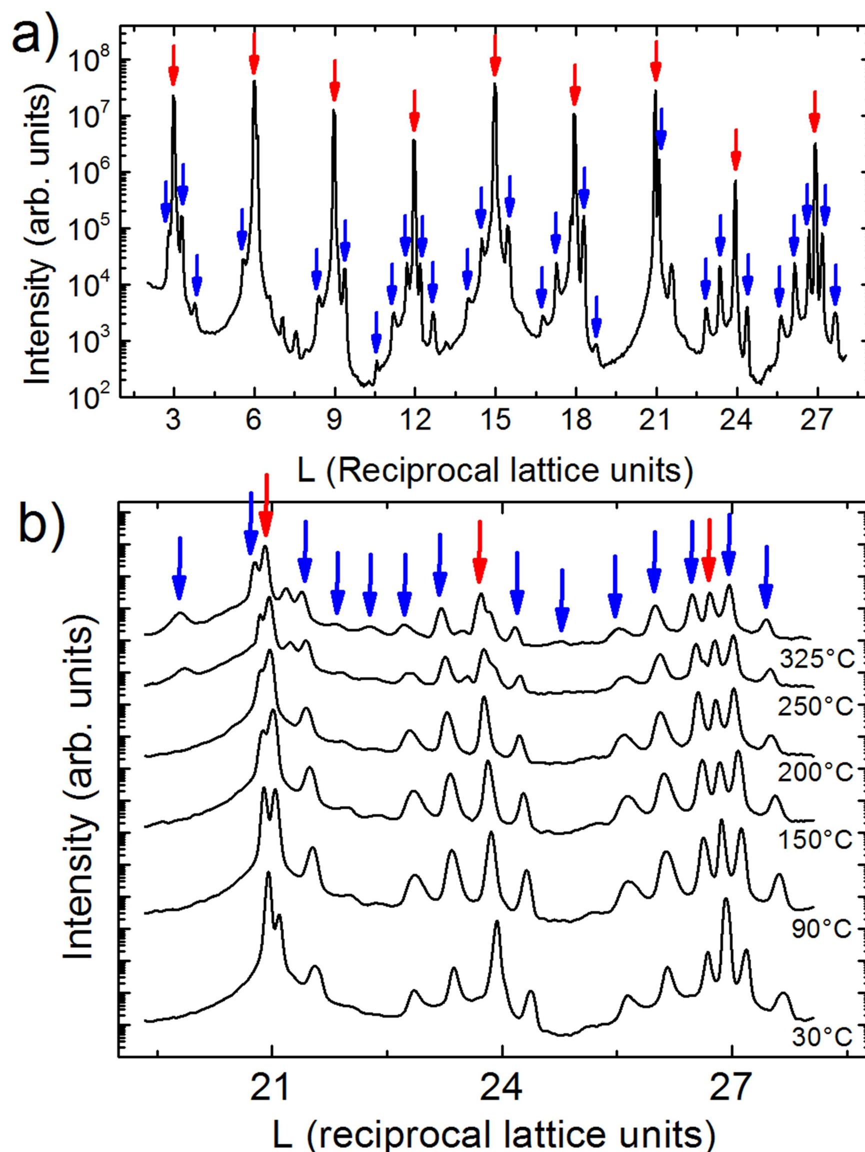

Figure 5.3: Phase changes observed with the increase of temperature for Bi_2Se_3. a) The 00L crystal truncation rod (room temperature). Red arrows indicate Bi_2Se_3 peaks, while the blue arrows indicate other periodicities (i.e., other phases), with the most preeminent being Bi_4Se_5. b) A closer look of the 00L crystal truncation rod data, for selected temperatures along the annealing ramp. One can see the increasing of the Bi_4Se_5 phase amplitude.

The volume of each phase observed in Figure 5.3 can be estimated by the evaluation of the area below diffraction peaks. If one analyzes carefully the changes that take place over the temperature ramp the disappearance of the main Bi_2Se_3 phase is promptly observed. On the other hand, the volume of Bi_4Se_5 phase increases. Since Selenium atoms are lighter the formation of Bi_4Se_5 phase inside the crystal is a result of Se sublimation. Figure 5.4 present the relative area below the Bragg's peak of all observed phases as a function of the temperature.

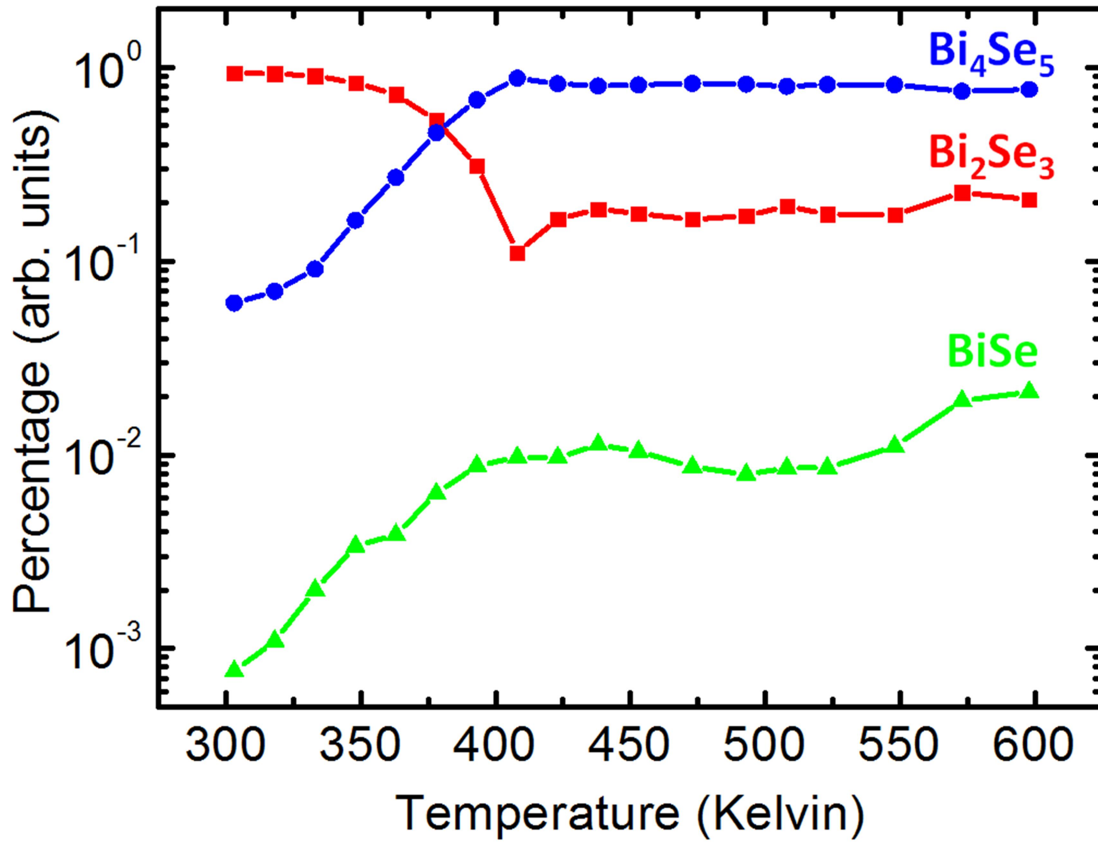

Figure 5.4: Relative peak area of Bi_2Se_3, Bi_4Se_5 and BiSe evaluated from CTR peaks as a function of temperature.

One can introduce two equations for the X-ray scattering intensity used to the experimental data:

$$I^{Bi_2Se_3}(L) = \frac{|A|^2}{4\sin^2(2\pi i L/2)} \left| \sum_{j=1}^{15} f_{Bi,Se}(L) \mathrm{e}^{2\pi i z_j L} \right|^2 \tag{5.1}$$

and

$$I^{Bi_4Se_5}(L) = |A|^2 \left| \sum_{j=1}^{27} f_{Bi,Se}(L,j) \mathrm{e}^{2\pi i z_j L} \sum_{k=1}^{N} \mathrm{e}^{2\pi i k L} \mathrm{e}^{-k\beta} \right|^2 . \tag{5.2}$$

Equations 5.1 and 5.2 depend on the reciprocal space coordinate L; j labels a given atom at the unit cell; z_j represents the position of which atom; $f_{Bi,Se}(L)$ the atomic form factor varying with j for the atom scattering factor: Bi or Se; A is an amplitude factor (order parameter); and β represents the absorption factor of each layer. Equation 5.1 was obtained from Eq. 3.20 and the form factor from Eq. 3.12. Equation 5.2 was obtained from Eq. 3.12 only, with an addition of an absorption factor from each layer.

A least-square fit of the X-ray data of Figure 5.5 was performed using these equations with relative amplitude factors for each phase including a similar equation for the minor BiSe phase.

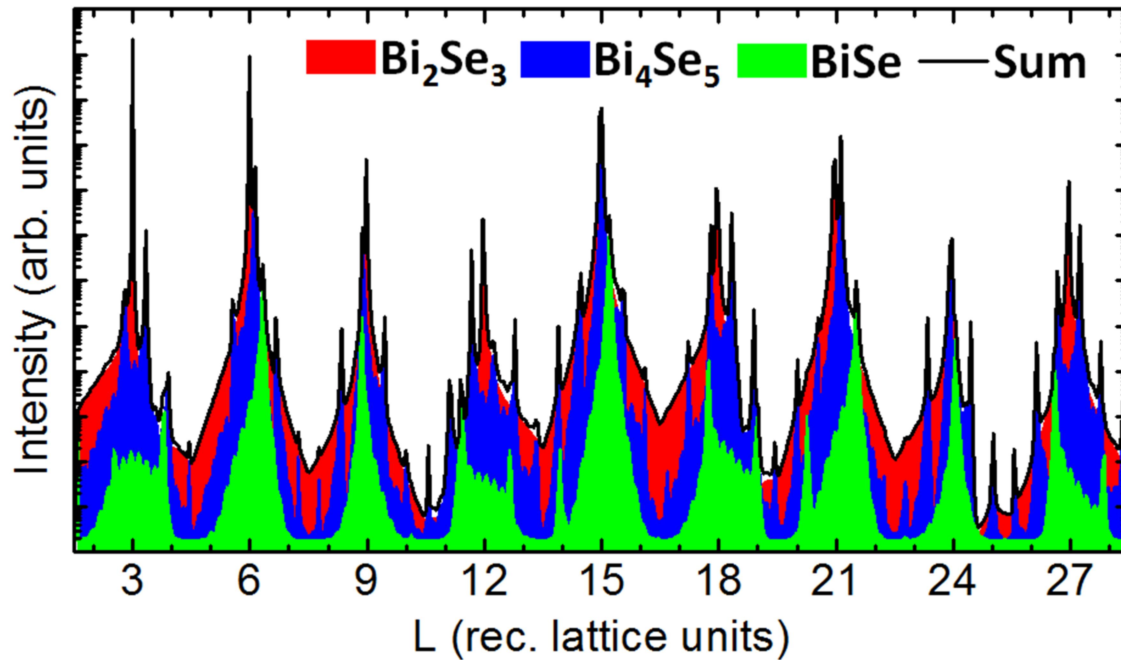

Figure 5.5: Least-square fit of the X-ray data of the Bi_2Se_3-Bi_4Se_5 sample at room temperature. The contribution of each Bi-Se compound is represented by the colored curves.

Values obtained for the perpendicular lattice parameter of the phases were: 2.86 nm for Bi_2Se_3, 5.18 nm for Bi_4Se_5 and 2.32 nm for BiSe. Specifics values of the fit parameters are shown in Table II.

Parameter	Bi_2Se_3	Bi_4Se_5	BiSe
Order Parameter – A	100%	5%	0.1%
Absorption factor – β	-	0.1	0.1
Number of atoms	6 Bi + 9 Se = 15	(10 Bi + 15 Se) + 2 Bi = 27	(4 Bi + 6 Se) + 2 Bi = 12
Off-plane lattice parameter	2.86 nm	5.18 nm	2.32 nm
Strain on the lattice parameter	+ 0.21%	- 0.55%	+ 6.00%
Number of layers	∞	25	25

Table II: Fit parameters of the curves in Figure 5.5.

Values of the off-plane lattice parameters of Bi_4Se_5 and BiSe were obtained constructing a unit cell from the unit cell of the Bi_2Se_3. We added a suitable number of QLs

with the bilayer, following the distance between them from the literature. The distance between the QL and the bilayer was also obtained from the literature. We also added strain to the lattice parameters to fit the experimental data.

Usually X-ray scattering techniques provide information about the bulk structure of crystalline samples (penetration depth ranging from few to hundred micrometers). Although the analysis of the CTR diffraction can directly reveal details of the surface structure the information is averaged over the X-ray spot area and, near Bragg peaks, masked by bulk information. To overcome such issue Scanning Tunneling Microscopy and Spectroscopy techniques were used in selected regions of the sample, revealing morphological and electronic aspects that cannot be captured by solving the CTR data. Before STM/STS results are discussed it is mandatory to understand the band structure of the retrieved dominant phases: Bi_2Se_3 and $Bi4Se_5$. Density Functional Theory calculations were performed by Prof. Mário Sérgio Carvalho Mazzoni (UFMG) and will be discussed in the following section.

5.2 Density Functional Theory calculations

Density Functional Theory (DFT) is a powerful tool to calculate the eigenvalues of a physical system [46]. The details of the calculation itself are beyond the scope of this dissertation and only the results will be discussed. DFT calculations of the electronic band structure and density of states of both Bi_2Se_3 and Bi_4Se_5 crystals are depicted in the following paragraphs. These calculations were carried out using single-crystalline models of each phase separately. In Figure 5.6, we show the possible terminations of the Bi_4Se_5 crystal used for the DFT. Considering that this phase is obtained with the addition of a Bi_2 layer to a supercell of five quintuple layers (QL) separated by Van der Waals gaps there are three distinct arrangements that were considered in DFT. From surface to bottom, these combinations can be of the type Bi_2/5QLs; or QL/Bi_2/4QLs; or 2QLs/Bi_2/3QLs. similar terminations with the Bi_2 layer lying on the lower half of the stack were obtained mirroring the three combinations explicitly listed above.

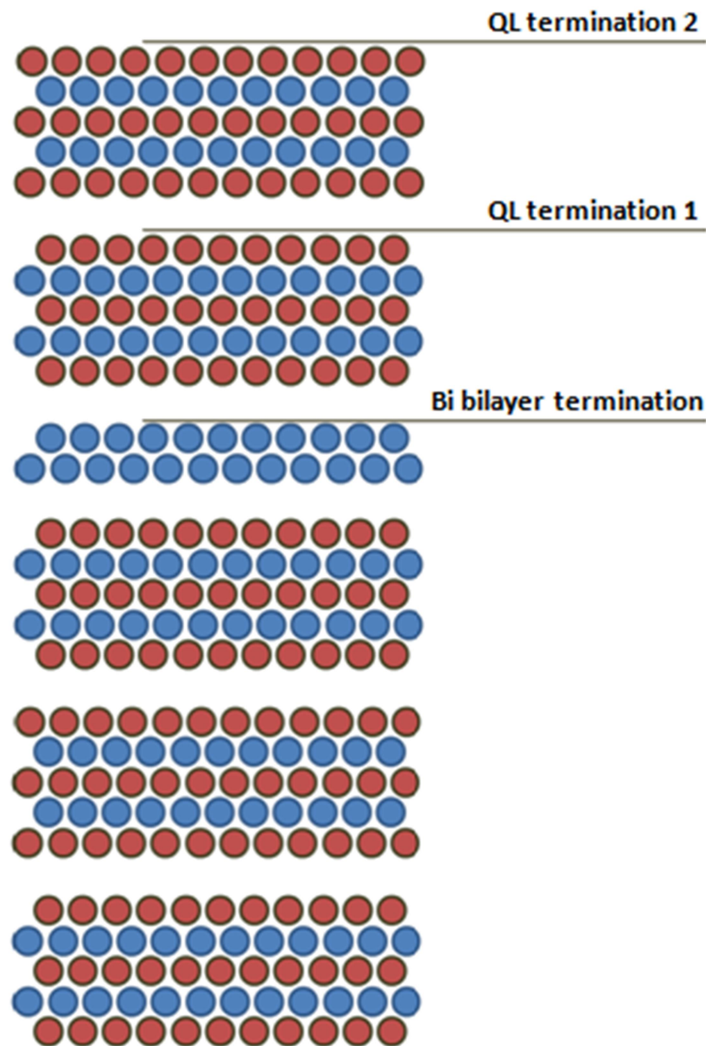

Figure 5.6: Possible surfaces terminations of Bi_4Se_5. There are three different types of termination for Bi_4Se_5crystals: Two of them terminate on quintuple-layers and one on a Bi bilayer. The other three terminations are obtained mirroring the crystal.

As a starting point for the electronic band discussion we show in Figure 5.7 the band structure of Bi_2Se_3. Three distinct regions on the band structure related to its density of states are highlighted in this figure, indicating the top of the valence band (blue), the low-density of states portion of the conduction band, near the Dirac point (yellow) and the high density of states portion of the conduction band (pink).

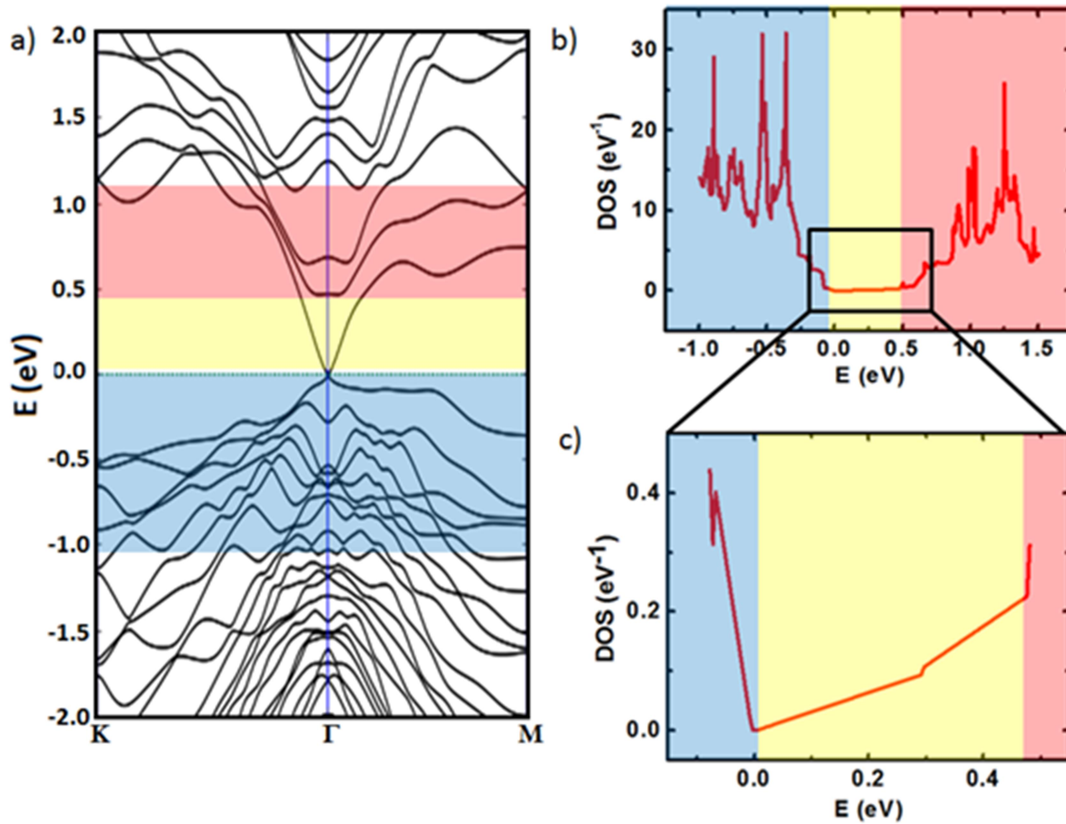

Figure 5.7: DFT Calculations showing the electronic band structure of Bi_2Se_3. (a) Large view of the band structure of Bi_2Se_3. (b) Local density of states of Bi_2Se_3. (c) A closer look to the LDOS of Bi_2Se_3 evidencing the Dirac point. The colors introduced in (a) represent the same regions highlighted in (b) and (c). All Images were made using the software Virtual NanoLab 2016.1 by QuantumWise A/S.

The calculated electronic band structure of the three arrangements of Bi_2:QLs discussed in Figure 5.6 is shown in Figure 5.8. One observes that many new states appear now around the Fermi-level of Bi_4Se_5 (more than in the Bi_2Se_3 crystal). A quick glimpse at the electronic band structure of the new crystals directly indicates that the Bi_4Se_5 is a conductor phase. It is also clear from these calculations that the Bismuth Selenide topological insulator states are not preserved in the Bi_4Se_5 phase. We can also see the appearance of van Hove singularities in these arrangements. The band structure of Bismuth Selenide changes completely with the addition of bilayers, above or below the QLs.

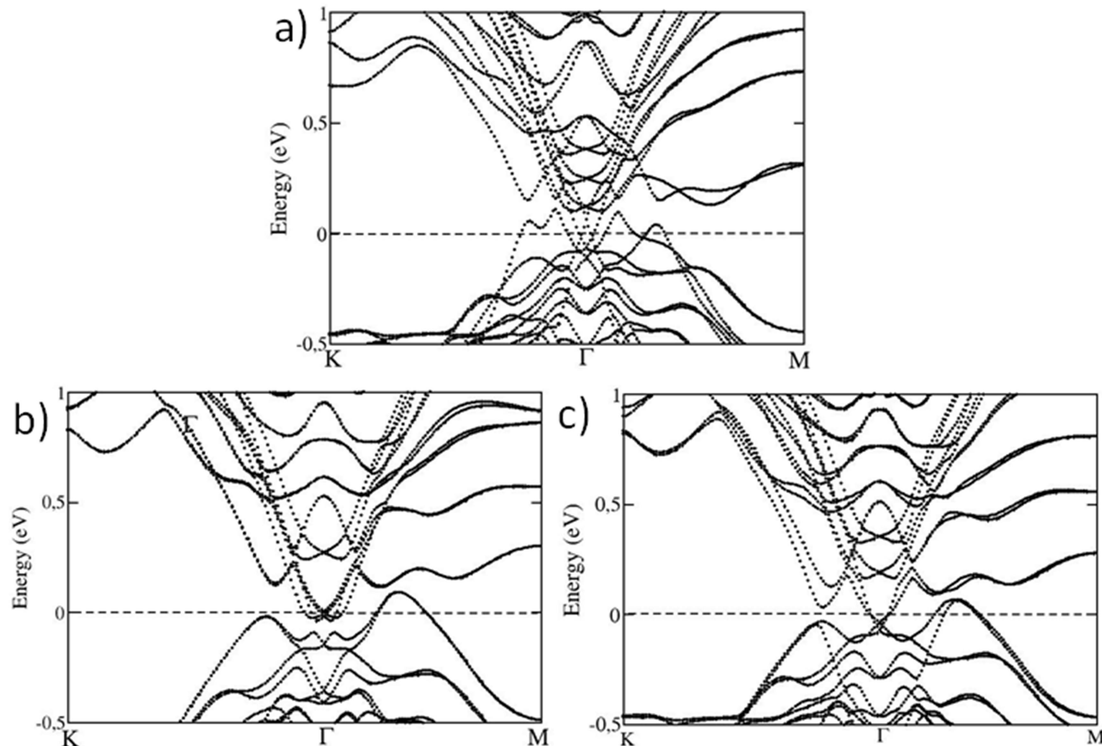

Figure 5.8: DFT Calculations of Bi_4Se_5. a) Electronic band structure of Bi_4Se_5 terminated by a Bismuth bilayer (Bi_2/5QLs), b) by the first QL above the Bi_2 bilayer (QL/Bi_2/4QLs) and c) by the second QL above the Bi_2 bilayer (2QLs/Bi_2/3QLs).

The calculated electronic band structure gives us a direction to correctly interpret the measured STS spectra. Some differences may arise between the two since DFT is calculated for low temperatures (0 K) considering a single-crystalline sample (thus representing the entire density of states) and STS information depends on the layer depth and surface step boundary conditions (such as cleavage defects and/or grain edges).

As we will see in the STM section, the Bi_4Se_5 phase seems to appear at the form of nanograins within the Bi_2Se_3 matrix. The goal of DFT calculations was to provide a qualitative scenario that can be compared to the electronic density of states information obtained by STS at the surface of the Bi_2Se_3/Bi_4Se_5 system. The densities of states of the QLs terminated system are shown in Figure 5.9. The calculations confirm the appearance of van Hove singularities, with are more prominent in the Bi_2/5QLs calculation. They became stronger with the proximity of the bilayer.

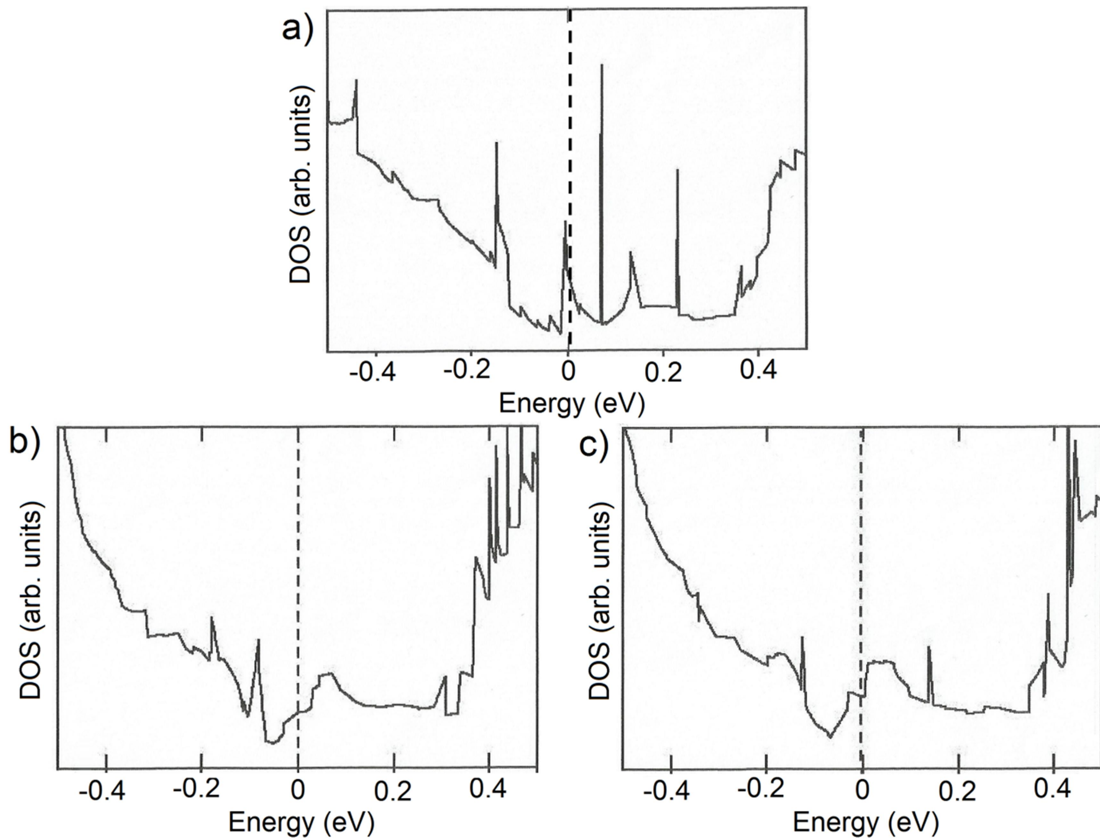

Figure 5.9: A closer look at the DFT Calculations of Bi_4Se_5. a) Electronic density of states of Bi_4Se_5 terminated by a) a quintuple layer ($QL/Bi_2/4QLs$), b) one quintuple layer ($1QLs/Bi_2/4QLs$) and c) two quintuple layers ($2QLs/Bi_2/3QLs$) .

The DFT results show that there is a stronger dependence of the topological state related to the position of the bilayer. A bilayer on the top of the QLs changes completely the electronic properties of the material. That effect decreases when the bilayer is inside the bulk QLs.

5.3 Scanning Tunneling Microscopy results

STM measurements showed the existence of Bi_2Se_3 and Bi_4Se_5 regions within the sample, paving the way for a clear understanding of the Bi_4Se_5 formation at the surface of our sample. In Figure 5.10 we present STM images of Bismuth Selenide at room temperature. These images were obtained on a cleaved surface of the sample (the cleaving procedure was performed inside the vacuum chamber). Current/voltage conditions for all measurements are declared in the figure captions, allowing the future replication of the results, if necessary.

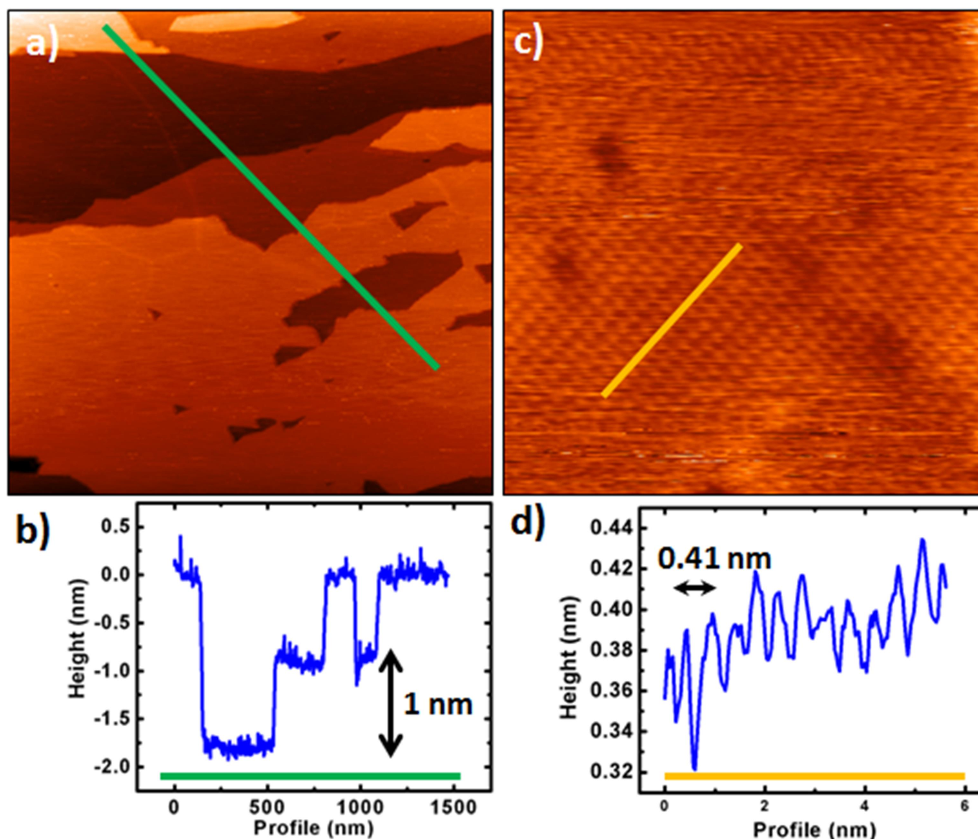

Figure 5.10 (Copy of Figure 2.9): STM images of a Bi_2Se_3 region at room temperature. a) STM image of a Bi_2Se_3 region, taken using I_{tun} = 100pA and V_{bias} = 1.0V. b) A single profile along the image above, showing a single surface step with 1 nm (height of a QL). c) High-resolution 16 nm^2 image of Bi_2Se_3, taken using I_{tun} = 20nA and V_{bias} = 500mV. b) A single profile along the image above.

In Figure 5.10a, a low-resolution STM topographic image is shown. A line profile, displayed in Figure 5.10b, reveals typical Bi_2Se_3 QL 1nm steps on the surface. The surface of the sample seems to be very flat, always presenting steps of a few nanometers (related to a few QLs). This flatness is due the cleavage process. The STM image of Figure 5.10c shows the hexagonal lattice of the Bi_2Se_3 surface. The height profile of Figure 5.10d directly evidences the position of individual atoms. The measured value for the in-plane lattice parameter was is 4.61 nm. For comparison, the value usually retrieved from the literature is 4.14 nm.

Our next step was to find regions where the onset of Bi_4Se_5 formation is observed. The sample was first heated to 350°C, in order to increase the formation of Bi_4Se_5 domains. The search for Bi_3Se_5 was performed by the looking at steps with less than 1 nm. These steps represent Bismuth bilayers.

Figure 5.11 shows typical regions with these nanograins. They exhibit steps of either 1 nm or 0.4 nm, which leads us to conclude that other Bismuth Selenide phases such as

Bi_4Se_5 and BiSe are present. Some nanograins as the one shown in Figure 5.11a have bilayers inside QLs (see Figure 5.11c).

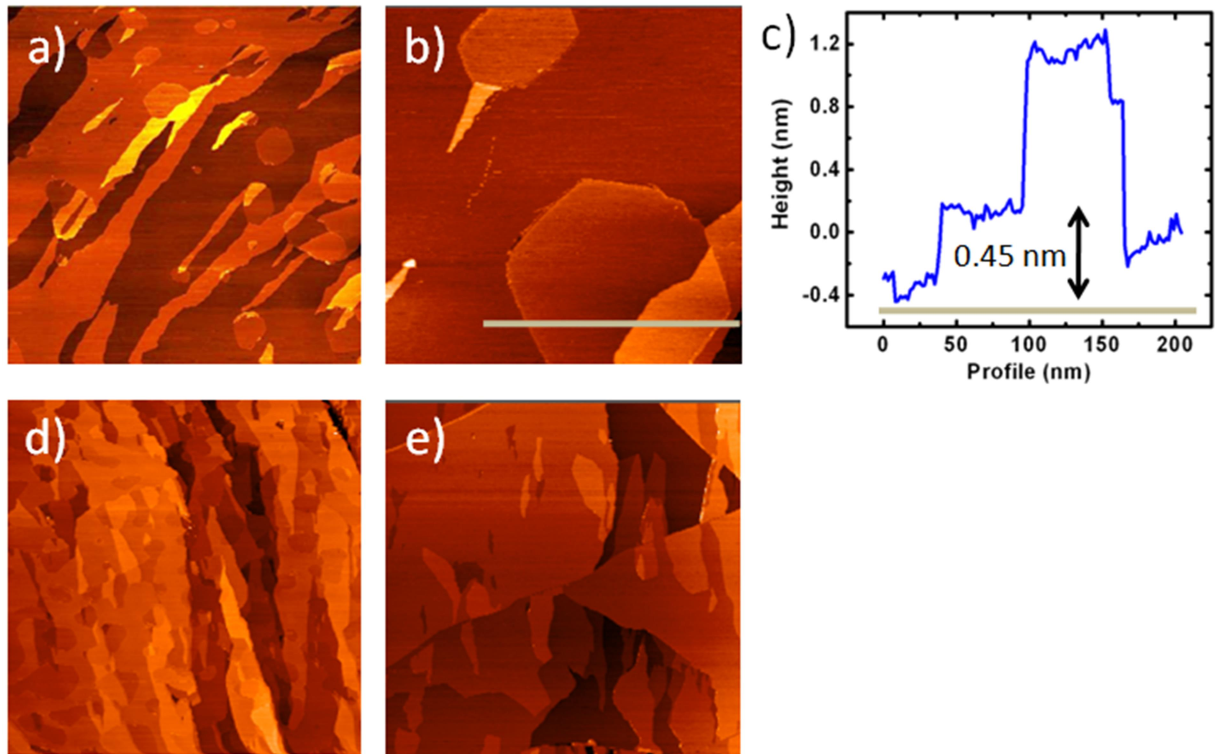

Figure 5.11: STM images of areas with Bi_2Se_3-Bi_4Se_5 phase coexistence. a) 1 μm^2 STM image of a region with few nanograins of Bi_4Se_5. b) 250 nm^2 closer look at the same image. c) Height profile along the nanograin zoomed in (a), showing a 0.4nm step. c) STM image of a region with many intercalated steps. d) STM image of a region with big Bi_4Se_5 nanoplates. All images were carried out using I_{tun} = 100pA and V_{bias} = 1.0V.

The whole sample exhibits two types of regions: one having a simple Bi_2Se_3 structure and another one with the appearance of minor Bi-Se phases nanograins. We found three different regions with such features, depending on the level of phase formation: one with a few nanograins steps (Figure 5.11a and 5.11b); one with many intercalated steps (Figure 5.11d); and the last one with big plates (Figure 5.11e). These regions represent the growth process of the new phases in the crystal. Going from (a), where the nanograins starts their formation, to (c) and (d), where the new phase covers large regions of the sample. The presence of steps of 0.4nm and 1.4nm as shown in Figure 5.11c shows that nanograins are part of the process of phase formation, in contrast with the results by Coelho et al. for Bi_2Te_3 case [47].

On may point that this is due to the formation of Bismuth bilayers on top of Bi_2Se_3, or the formation of them among Bi_2Se_3 quintuple-layers. We speculate that during sample

annealing selenium atoms flow out of the system through grain boundaries and defects, allowing the formation of stable Bismuth bilayers between stacks of five quintuple layers, forming the Bi_4Se_5 phase. This phase was previously detected by X-ray measurements and the main non-stoichiometric Bi_2Se_3 phase.

To confirm such hypothesis we have performed Scanning Tunneling Spectroscopy (STS) measurements, measuring the local electronic density of states of grains and plateaus. These STS results were then compared to DFT models of Bi_4Se_5.

5.4 Scanning Tunneling Spectroscopy results

In this final section of chapter 5 we provide a connection between STS measurements and the local density of states (LDOS) of our sample. We have retrieved out STS data on top of a large new-phase nanograin and over the plateau of Bi_2Se_3. The STS measurement of Bi_2Se_3 was taken in a region far away from nanograins, to avoid any interference from them. In Figure 5.12a we present a scanning tunneling spectrum of the Bi_2Se_3 region, exhibiting the Bi_2Se_3 topological insulator behavior near the Dirac point. The LDOS of Bi_2Se_3 obtained with Density Functional Theory (DFT) is shown in Figure 5.12b for comparison.

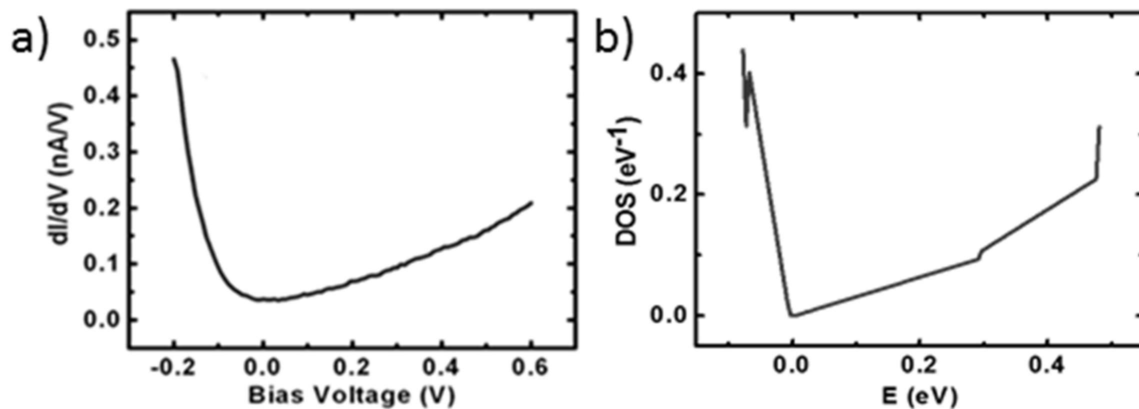

Figure 5.12: Scanning Tunneling Spectroscopy of Bi_2Se_3: a) STS on an isolated region of Bi_2Se_3. b) DFT Calculation of the Density of States of Bi_2Se_3 near the Dirac point. The measurement in (a) was carried out at a temperature of 23K.

Selected spectroscopy measurements on different nanograins are shown in Figure 5.13. We perform STS on three different regions: one away from the grain (a Bi_2Se_3 region); one inside the grain in a bilayer termination (BL); and one inside the grain in a quintuple-layer termination (QL). One observes that the nanograin has a conducting behavior since the

dI/dV value for V = 0 is non-zero. These nanograin regions exhibit signatures of a topological insulator with an added constant value in its conductance.

It seems that the addition of bilayers to form new phases of Bismuth Selenide, add new states near the Fermi-level of the material. The dI/dV curve of STS measurements moves away from zero mainly on the zero voltage point. The conducting behavior is expected from the DFT calculations of Bi_4Se_5, albeit with van hove singularities.

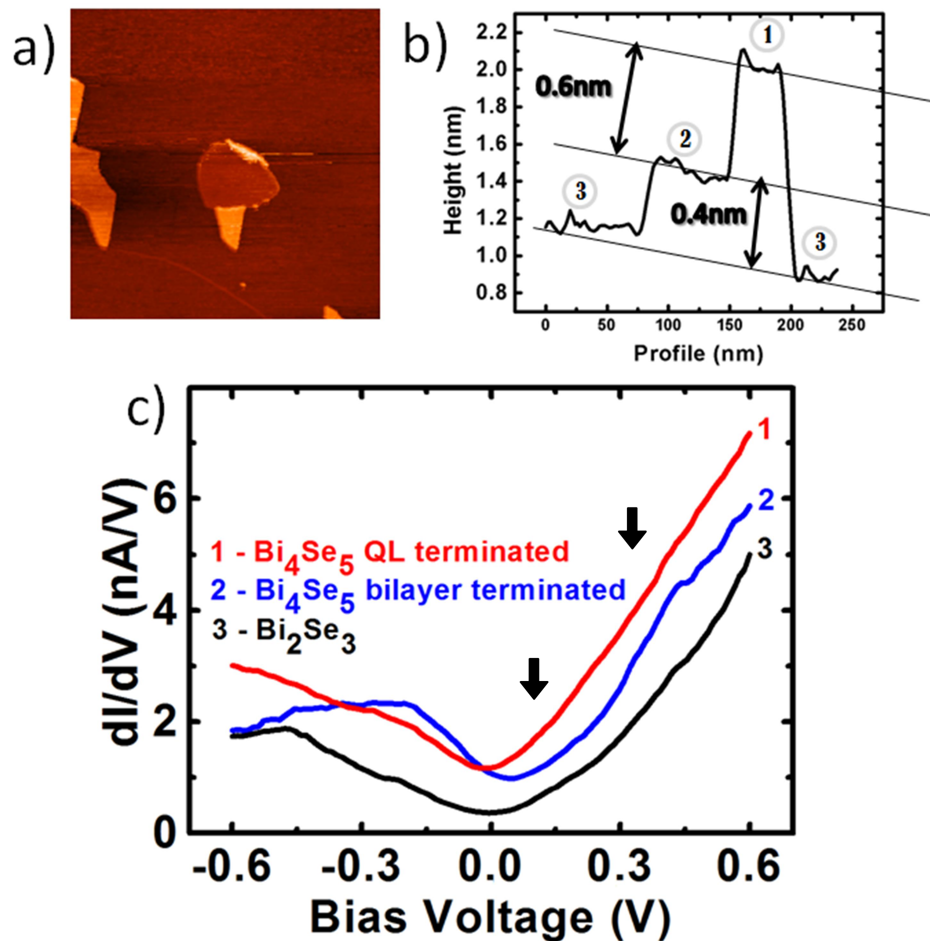

Figure 5.13: Scanning Tunneling Spectroscopy of the nanograin: a) STM image of a nanograin (I_{tun} = 100pA and V_{bias} = 1.0V). b) Height profile showing the heights on the surface termination of a nanograin. c) STS in the regions of the nanograin. The measurements were carried out at a temperature of 23K.

Another way to analyze this behavior is to perform STS measurements in a line crossing the nanograin. Figure 5.14 shows a collection of dI/dV curves as the tip moved into the nanograin, showing a tendency of conductance values to drift away from zero. In this figure the local density of states changes from a topological insulator to a conducting

behavior. In brief, Bismuth bilayers on top (black curve in Figure 5.13c), or even inside the Bi_2Se_3 matrix (red curve in Figure 5.13c) changes the electronic behavior of the material but only introduce peaks for the LDOS on the bilayer termination (see around 0.2 eV and 0.4 eV in Figure 5.13), as expected for Bi_4Se_5.

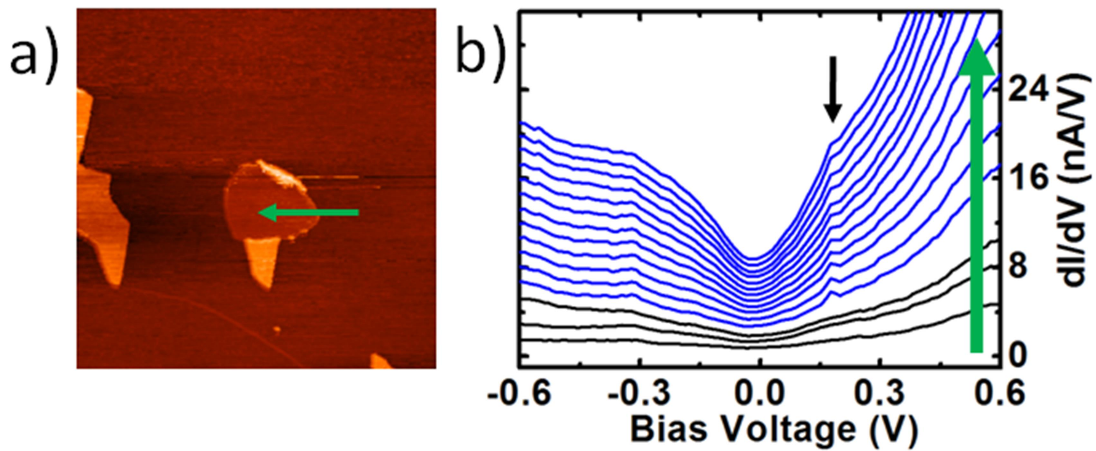

Figure 5.14: Scanning Tunneling Spectroscopy measurements performed over a line entering the Bi_4Se_5 nanograin: (a) STM image of Bi_4Se_5.presenting the line over with did the spectra. I_{tun} = 100pA and V_{bias} = 1.0V. (b) STS spectra of the line showed in (a) showing the shift of the LDOS. The lower curve corresponds to the first STS measurement in the Bi_2Se_3 plateau, while the upper curve is measured at the grain center. The measurements were performed at 25K.

Recent STS studies by Drozdov et al [48] have shown that a bismuth bilayer behaves as a 2D topological insulator (see section 2.3). In a two-dimensional topological insulator, a conducting channel along the borders of the system is found. In their work, the measurements were performed in Bismuth bilayers islands on a Bi(111) surface matrix. This work speculated that Bi_2 islands on a Bi_2Se_3 surface might retain the 2D topological insulator behavior.

6 - Conclusion and prospects

The main goal of this work was to understand the transformations that occur in the topological insulator Bi_2Se_3 upon heating, concerning its electronic and atomic properties. Using the technique of Scanning Tunneling Microscopy and Spectroscopy combined with X-Ray Diffraction experiments we could infer the electronic density of states combined and the crystal structure of our sample.

Our sample, a polyphase Bi_2Se_3-Bi_4Se_5 crystal, was first characterized by X-Ray scattering along the 00L and 01L truncation rods. We observed the main Bi_2Se_3 phase with a secondary Bi_4Se_5 one. Upon heating the material up to 325°C, the Bi_2Se_3 phase starts to disappear while the onset of Bi_4Se_5 formation is observed. As Crystal Truncation Rods are surface-sensitive, this encouraged us to perform Scanning Tunneling Microscopy and Spectroscopy.

In Scanning Tunneling Microscopy experiments after heating the sample, we observed the formation of nanograins which may be Bi_4Se_5. They appeared at some regions of the sample and were first identified by 0.4 nm steps. The surface of Bi_2Se_3 is only comprised of 1 nm steps due to quintuple-layers connected by weak van der Waals interactions.

Scanning Tunneling Spectroscopy experiments were performed inside and outside these nanograins. The spectra outside the nanograins, on the Bi_2Se_3, showed the expected topological insulator behavior. Inside these nanograins, the STS measurements indicated a conducting behavior. Measurements made along a line entering the nanograin showed the transition from the topological insulator to a conducting feature. Although the nanograins present a conducting behavior, their spectra are similar to Bi_2Se_3.

We cannot conclude if that conductor state is caused by modifications of bulk or surface states. This question is difficult to answer using STS and require separate surface and bulk states information. A possible way to answer this question is to perform Angle-Resolved Photoemission Spectroscopy (ARPES) at the nanograin. This requires a focused ultra-violet nanobeam in a very specific area of an ordinary sample. A technique called nanoARPES, only available at the ANTARES Beamline of the SOLEIL Synchrotron in France, would solve this question.

Another prospect of this work is related to the fact that bismuth bilayers are two-dimensional topological insulator. This means that a Bi_2Se_3-Bi_4Se_5 sample upon heating could be an interesting subject for future studies. This system combines two and three-dimensional topological insulators in a balanced system.

References

[1] Philip L. Taylor, Olle Heinonen. *A Quantum Approach to Condensed Matter Physics*. Cambridge University Press, **2002**.

[2] Alan G. Michette, Sławka Pfauntsch. *X-rays: the first hundred years*. John Wiley & Sons, **1996**.

[3] Michael Stone. *Quantum Hall Effect*. World Scientific, **1992**.

[4] K. S. Novoselov, A. K. Geim, S. V. Morozov, D. Jiang, M. I. Katsnelson, I. V. Grigorieva, S. V. Dubonos, A. A. Firsov; *Nature* **2005**, 438, 197-200.

[5] Fan Zhang, C. L. Kane, E. J. Mele. *Phys. Rev. B* **2012**, 86, 081303.

[6] Matthias Götte, Michael Joppe, Thomas Dahm. *Scientific Reports* **2016**, 6, 36070.

[7] P. Richard, K. Nakayama, T. Sato, M. Neupane, Y.-M. Xu, J. H. Bowen, G. F. Chen, J. L. Luo, N. L. Wang, X. Dai, Z. Fang, H. Ding, and T. Takahashi. *Phys. Rev. Lett.* **2010**, 104, 137001.

[8] Charles L. Fefferman, James P. Lee-Thorp, Michael I. Weinstein. *Topologically Protected States in One-Dimensional Systems*. Memoirs of the American Mathematical Society, **2014**.

[9] A. Messiah. *Quantum Mechanics, vol. I*. North Holland Publishing Company, **1967**.

[10] Walter A. Harrison. *Electronic structure and the properties of solids: the physics of the chemical bond*. Dover Publications, **1989**.

[11] Charles Kittel. *Introduction to Solid State Physics*. John Wiley & Sons, **2004**.

[12] I. Tamm. *Phys. Z. Sowjetunion* **1932**, 1, 733-746.

[13] S. D. Kevan, R. H. Gaylord. *Phys. Rev. B* **1987**, 36, 5809-5818.

[14] Klaus von Klitzing. *Rev. Mod. Phys*. **1986**, 58, 519.

[15] S. A. Mikhailov, *Physica B* **2001**, 299, 6-31.

[16] Pedram Roushan, Jungpil Seo, Colin V. Parker, Y. S. Hor, D. Hsieh, Dong Qian, Anthony Richardella, M. Z. Hasan, R. J. Cava, Ali Yazdani. *Nature* **2009**, 460, 1106-1109.

[17] J. E. Avron, D. Osadchy, R. Seiler. *Phys. Today* **2003**, 56, 38.

[18] B. Andrei Bernevig, Taylor L. Hughes, Shou-Cheng Zhang. *Science* **2006**, 314, 1757-1761.

[19] Markus König, Steffen Wiedmann, Christoph Brüne, Andreas Roth, Hartmut Buhmann, Laurens W. Molenkamp, Xiao-Liang Qi, Shou-Cheng Zhang. *Science* **2007**, 318, 766-770.

[20] H. B. Zhang, H. Li, J. M. Shao, S. W. Li, D. H. Bao, G. W. Yang. *ACS Appl. Mater. Interfaces* **2013**, 5, 11503.

[21] C. L. Kane, E. J. Mele. *Phys. Rev. Lett.* **2005**, 95, 226801.

[22] Zhiyong Zhu, Yingchun Cheng, Udo Schwingenschlögl. *Phys. Rev. B* **2012**, 85, 235401.

[23] Liang Fu, C. L. Kane, E. J. Mele. *Phys. Rev. Lett.* **2007**, 98, 106803.

[24] Joel E. Moore; *Nature* **2010**, 464, 194-198.

[25] L. Fu, C. L. Kane; *Phys. Rev. B* **2007**, 76, 045302.

[26] D. Hsieh, D. Qian, L. Wray, Y. Xia, Y. S. Hor, R. J. Cava, M. Z. Hasan. *Nature* **2008**, 452, 970.

[27] Hai-Jun Zhang, Chao-Xing Liu, Xiao-Liang Qi, Xiao-Yu Deng, Xi Dai, Shou-Cheng Zhang, Zhong Fang. *Phys. Rev. B* **2009**, 80, 085307.

[28] Y. L. Chen, J. G. Analytis, J.-H. Chu, Z. K. Liu, S.-K. Mo, X. L. Qi, H. J. Zang, D. H. Lu, X. Dai, Z. Fang, S. C. Zhang, I. R. Fisher, Z. Hussain, Z.-X. Shen. *Science* **2009**, 325, 178.

[29] Marco Bianchi, Dandan Guan, Shining Bao, Jianli Mi, Bo Brummerstedt Iversen, Philip D.C. King, Philip Hofmann. *Nature Communications* **2010**, 1, 128.

[30] D. Hsieh, Y. Xia, D. Qian, L. Wray, F. Meier, J. H. Dil, J. Osterwalder, L. Patthey, A. V. Fedorov, H. Lin, A. Bansil, D. Grauer, Y. S. Hor, R. J. Cava, M. Z. Hasan. *Phys. Rev. Lett.* **2009**, 103, 146401.

[31] Joonki Suh, Deyi Fu, Xinyu Liu, Jacek K. Furdyna, Kin Man Yu, Wladyslaw Walukiewicz, Junqiao Wu. *Phys. Rev. B* **2014**, 89, 115307.

[32] Y. S. Hor, A. Richardella, P. Roushan, Y. Xia, J. G. Checkelsky, A. Yazdani, M. Z. Hasan, N. P. Ong, R. J. Cava. *Phys. Rev. B* **2009**, 79, 195208.

[33] James G. Analytis, Jiun-Haw Chu, Yulin Chen, Felipe Corredor, Ross D. McDonald, Z. X. Shen, Ian R. Fisher. *Phys. Rev. B* **2010**, 81, 205407.

[34] A. V. Antipov, E. B. Rudnyi, Z. V. Dobrokhotova. *Inorganic Materials* **2001**, 37, 126.

[35] Paengro Lee, Jinwoong Kim, Jin Gul Kim, Min-tae Ryu, Hee-min Park, Namdong Kim, Yongsam Kim, Nam-Suk Lee, Nicholas Kioussis, Seung-Hoon Jhi, Jinwook Chung. *Journal of Physics: Condensed Matter* **2010**, 28, 8.

[36] Jens Als-Nielsen, Des McMorrow. *Elements of Modern X-ray Physics*. John Wiley & Sons, **2011**.

[37] John David Jackson. *Classical electrodynamics*. John Wiley & Sons, **2010**.

[38] Leslie E. Ballentine. *Quantum Mechanics: A Modern Development*. World Scientific, **1998**.

[39] C. Julian Chen. *Introduction to Scanning Tunneling Microscopy*. Oxford University Press, **1993**.

[40] R. Landauer. *IBM J. Res. Dev*. **1957**, 21, 223-230.

[41] G. Binnig, H. Rohrer, Ch. Gerber, E. Weibel. *Appl. Phys. Lett*. **1982**, 40, 178-180.

[42] M. Brandbyge, J. Schiotz, M. R. Sorensen, P. Stoltze, K. W. Jacobsen, J. K. Norskov, E. Laegsgaard, I. Stensgaard, F. Besenbache. *Phys. Rev. B* **1995**, 52, 8499-8514.

[43] J. Bardeen. *Phys. Rev. Lett*. **1961**, 6, 57-59.

[44] J. Tersoff; D. R. Hamann. *Phys. Rev. Lett*. **1983**, 50, 1998-2001.

[45] Charles L. Fefferman, James P. Lee-Thorp, Michael I. Weinstein; R. M. Feenstra, J. Y. Lee, M. H. Kang, G. Meyer, K. H. Rieder. *Phys. Rev. B* **2006**, 73.

[46] Eberhard Engel, Reiner M. Dreizler. *Density Functional Theory: An Advanced Course*. Springer Berlin Heidenlberg, **2011**.

[47] Paula M. Coelho, Guilherme A. S. Ribeiro, Â. Malachias, Vinicius L. Pimentel, Wendell S. Silva, Diogo D. Reis, Mário S. C. Mazzoni, Rogério Magalhães-Paniago. *Nano Lett.* **2013**, 13, 4517-4521.

[48] Ilya K. Drozdov, A. Alexandradinata, Sangjun Jeon, Stevan Nadj-Perge, Huiwen Ji, R. J. Cava, B. Andrei Bernevig, Ali Yazdani. *Nature Physics* **2014**, 10, 664-669.

Appendix

Papers related to this dissertation.

1) *Formation of Bi_xSe_y Phases Upon Annealing of the Topological Insulator Bi_2Se_3: Stabilization of In-Depth Bismuth Bilayers*. P. H. R. Gonçalves, Thais Chagas, V. B. Nascimento, D. D. dos Reis, Carolina Parra, M. S. C. Mazzoni, Ângelo Malachias, and Rogério Magalhães-Paniago. **Journal of Physical Chemistry Letters 9, 954−960 (2018).**

2) *Phase Separation of Dirac Electrons in Topological Insulators at the Spatial Limit*. Carolina Parra, Thiago H. R. Cunha, Alex W. Contryman, Desheng Kong, Francisco Montero-Silva, Pedro H. R. Gonçalves, Diogo D. Reis, Paula Giraldo-Gallo, Rodrigo Segura, Fernanda Olivares, Francis Niestemski, Yi Cui, Rogerio Magalhaes-Paniago, and Hari C. Manoharan. **Nano Letters 17, 97−103 (2017).**

THE JOURNAL OF PHYSICAL CHEMISTRY Letters

Letter

Cite This: J. Phys. Chem. Lett. 2018, 9, 954−960

pubs.acs.org/JPCL

Formation of Bi_xSe_y Phases Upon Annealing of the Topological Insulator Bi_2Se_3: Stabilization of In-Depth Bismuth Bilayers

P. H. R. Gonçalves,[†] Thais Chagas,[†] V. B. Nascimento,[†] D. D. dos Reis,[‡] Carolina Parra,[§] M. S. C. Mazzoni,[†] Ângelo Malachias,[*,†] and Rogério Magalhães-Paniago[†]

[†]Physics Department, Federal University of Minas Gerais, Avenida Presidente Antônio Carlos 6627, 31270-901, Belo Horizonte, Minas Gerais, Brazil

[‡]Physics Institute, Federal University of Mato Grosso do Sul, Avenida Costa e Silva, S/N, 79070-900, Campo Grande, Mato Grosso do Sul, Brazil

[§]Nano-biomaterials Laboratory, Physics Department, Technical University Federico Santa María, Avenida España, 1680, Valparaíso, Chile

ABSTRACT: The goal of this work is to study transformations that occur upon heating Bi_2Se_3 to temperatures up to 623 K. X-ray diffraction (XRD) and scanning tunneling microscopy (STM) and spectroscopy (STS) techniques were used in our investigation. XRD was measured following the 00L and 01L truncation rods. These measurements revealed that upon heating there is a coexistence of a major Bi_2Se_3 phase and other ones that present structures of quintuple-layers intercalated with Bismuth bilayers. STM measurements of the surface of this material showed the presence of large hexagonal Bi_xSe_y domains embedded in a Bi_2Se_3 matrix. STS experiments were employed to map the local electronic density of states and characterize the modifications imposed by the presence of the additional phases. Finally, density functional theory (DFT) calculations were performed to support these findings.

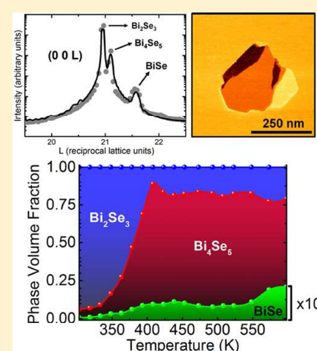

The interplay between topological and electronic properties of two-dimensional systems has been attracting considerable scientific attention in the last years.[1] These efforts led to the characterization of the so-called topological insulators (TIs).[2,3] In these materials, a band inversion mechanism[4] is responsible for the existence of topologically protected spin polarized surface states, which show up in the band structure as linear dispersion bands.[5−7] The resulting Dirac cone is found superimposed to semiconducting bulk states. That is the case, for instance, of the chalcogenide-based TIs such as Bi_2Te_3, Bi_2Se_3, and Sb_2Te_3, which present relatively large bulk bandgaps[8] that make them promising candidates for applications in nanoelectronic devices.[9,10] Bismuth bilayers (Bi_2) have also been important in this context since they were predicted to feature quantum spin hall effect.[11] Several strategies for Bi_2 synthesis and stabilization have been reported, such as hydrogen etching treatment in Bi_2Se_3[12] and thermal annealing of Bi_2Te_3.[13] The question on the exact position of Bi_2 within the 3D TI structure (either Bi_2Se_3 or Bi_2Te_3), especially whether it is always found on the surface, may be regarded as a challenging problem. Incidentally, a theoretical work has shown that energetic aspects are not able to distinguish a configuration in which the Bi_2 is on the surface or inside a 3D TI slab.[14]

In this work we address this question by investigating the structural and compositional evolution of a sample containing a minor amount of nonstoichiometric Bi_2Se_3 phases. Once subjected to a controlled annealing process (carried out in air), the system evolves into a crystal with larger fractions of Bi_xSe_y compounds through the formation of local Bi bilayers distributed within the bulk. The idea is based on the well-known fact that high quality Bi_2Se_3 crystals are formed in stoichiometric conditions, but a lack of Selenium may cause other phases to be formed; in this case, their stabilities vary according to the Bi:Se ratio as well as to synthesis and annealing temperatures.[15] We carried out X-ray crystal truncation rod measurements with in situ annealing by using a variable temperature furnace. A coexistence of Bi_2Se_3, Bi_4Se_5, and BiSe was shown to take place, and the relative volume fraction of each compound was obtained from the (00*L*) and (01*L*) crystal truncation rods (CTRs). Scanning tunneling microscopy (STM) and spectroscopy (STS) measurements were also carried out, and show electronic footprints of Bi_2Se_3 and Bi_4Se_5 regions in the sample surface, allowing an improvement of the understanding of Bi_4Se_5 formation in our sample. Density functional theory (DFT) calculations were employed to understand the experimental models for Bi_2 incorporation into the Bi_2Se_3 structure. Our main result may be summarized as the observation of the evolution of additional phases leading to Bi_2 structures, which may be found either on the surface or intercalated within Bi_2Se_3 quintuple layers.

Received: November 30, 2017
Accepted: February 2, 2018
Published: February 3, 2018

ACS Publications © XXXX American Chemical Society

DOI: 10.1021/acs.jpclett.7b03172
J. Phys. Chem. Lett. 2018, 9, 954−960

The unit cell of Bi_2Se_3 is represented in Figure 1a. In this compound, the in-plane position of a Se atom at the bottom of

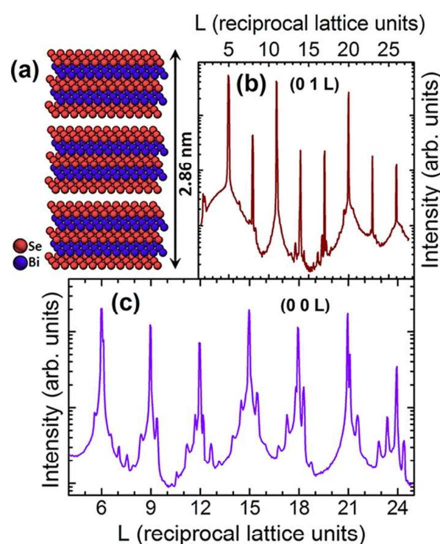

Figure 1. X-ray crystal truncation rod diffraction results. (a) Sketch of the unit cell of Bi_2Se_3. (b) Measurement of the $(01L)$ crystal truncation rod. (c) Measurement of the $(00L)$ crystal truncation rod.

a quintuple layer is only recovered in the periodic registry after three complete quintuple layers. Hence, an out-of-plane lattice parameter of 2.864 nm is observed, while in-plane lattice parameters are found to have the same value of 0.414 nm. The $(01L)$ CTR shown in Figure 1b exhibits strong and sharp peaks compatible with this structure, which has nonzero structure factor at $L = (3n - 1)$ along this reciprocal space line (where n is an integer). Although some minor peaks are observed besides the bulk phases in the interval between $L = 12$ and $L = 18$, none of them is strong enough to indicate the presence of other phases. However, in a lamellar system, the in-plane registry may be lost during the formation of distinct phases. A pure out-of-plane scan such as the $(00L)$ CTR provides more direct evidence of phase coexistence. This measurement, shown in Figure 1c, depicts a plethora of small peaks surrounding the strong and sharp Bi_2Se_3 peaks located at the condition $L = 3n$ (n integer). By performing a simple evaluation of the area below peaks in this scan, one obtains that nonstoichiometric Bi_xSe_y compounds represent less than 5% of the crystal volume at room temperature.

The nonstoichiometric phases can be indexed and quantified by fitting the room temperature $(00L)$ CTR experimental data. This procedure is employed in our case by simulating a bulk Bi_2Se_3 crystal with additional Bi_4Se_5 and BiSe layers. Equations 1 and 2 describe the CTR model used.[16,17] The diffracted intensity as a function of the lamellar reciprocal space index L is given by

$$I^{\mathrm{CTR}}(L) = \frac{(1-\sigma)^2}{1+\sigma^2 - 2\sigma\cos(2\pi L)} \frac{|A|^2}{4\sin^2(\pi L)} \times \left| \sum_{j=1}^{15} f_{\mathrm{Bi,Se}}(L, j) e^{2\pi i z_j L} \right|^2 \tag{1}$$

$$I^{\mathrm{layers}}(L) = |A|^2 \left| \sum_{j=1}^{n} f_{\mathrm{Bi,Se}}(L, j) e^{2\pi i z_j L} \sum_{k=1}^{N} e^{2\pi i k L} e^{-k\beta} \right|^2 \tag{2}$$

where A is a scaling factor (which accounts for the X-ray incident intensity, illumination, footprint, etc.), L is the reciprocal space coordinate, $f_{\mathrm{Bi,Se}}$ is the atomic scattering factor of Bi or Se atoms (depending on the site indexed by j), z_j is the coordinate position of the J atom inside the respective unit cell, k is the index of the layer, N is the number of layers, σ is the roughness of the sample, and β is the absorption factor.

Figure 2a shows the $(00L)$ CTR experimental data (upper curve) and the result of our simulations (bottom curves). The

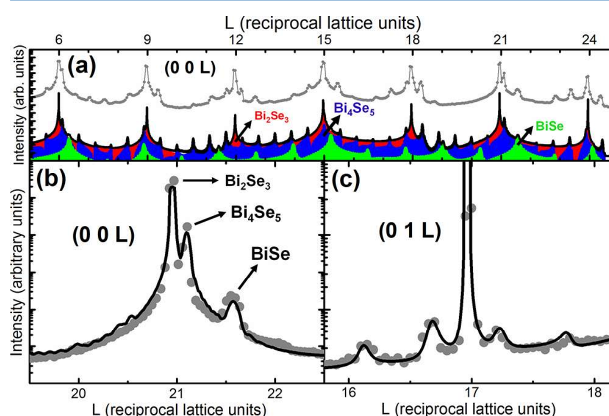

Figure 2. (a) Fit on the measured $(00L)$ CTR (data shown as gray dots, connected by line). The contributions from distinct Bi_xSe_y stoichiometries to the fit of the experimental results are shown: Bi_2Se_3 (red), Bi_4Se_5 (blue), and BiSe (green). All contributions were summed to produce the black curve (fitting). (b) Detail of the fit near the (0 0 21) peak of the $(00L)$ CTR. (c) Fit of the (0 1 17) peak of the $(01L)$ CTR. The parameters for all fits shown here are listed in Table 1.

simulated curve accounts for three major Bi_xSe_y phases. Namely, they are (i) the bulk Bi_2Se_3, which is the phase that accounts for most of the CTR features, and is found to correspond to 93% of the material volume; (ii) Bi_4Se_5, which here is responsible for most of the correlation peaks and; and (iii) BiSe, which is a minor phase in volume for all samples and conditions studied. At 303 K, Bi_4Se_5 and BiSe correspond to 6.5% and 0.5% of the sample volume, respectively. The contribution to the overall diffraction profiles of each phase is depicted on the lower, color-coded curves of Figure 2a. A quantitative description of the fit parameters used in this analysis is provided in Table 1.

The detail of the simulation near the (0 0 21) Bragg peak is shown in Figure 2b. Here we observe satellite peaks, which indicate a spatial correlation along the z-axis (out of plane, lamellar direction) of 5.155 nm (Bi_4Se_5) and 2.257 nm (BiSe). We found out that these lamellar distances correspond to 5 and 2 quintuple layers, respectively. Such periodicities do not match the usual ensemble of three lamellae of quintuple layers, which produces an in-plane registry of atoms that form the Bi_2Se_3 unit cell. In order to achieve such periodicities one must insert Bi_2 layers along the crystal, separated one from another by the correlation distances of 5 and 2 quintuple layers. In such case, the Bi_2 layer has a structure in which its upper Bi atoms produce a registry with the first Se atoms of the quintuple layer

DOI: 10.1021/acs.jpclett.7b03172
J. Phys. Chem. Lett. 2018, 9, 954–960

Table 1. Parameters Used for the Fitting of the (00*L*) and (01*L*) CTRs[a]

phase	Bi_2Se_3	Bi_4Se_5	BiSe
relative amplitude factor − *A*	1	0.0667	0.006
number of atoms − *N*	6 Bi + 9 Se = 15	(10 Bi + 15 Se) + 2 Bi = 27	(4 Bi + 6 Se) + 2 Bi = 12
out of plane lattice parameter	2.864 nm	5.155 nm	2.257 nm
strain along out of plane direction	+0.23%	−0.55%	−2.70%
number of layers	∞	12	16
in-plane lattice parameter	0.414 nm	0.423 nm	0.414 nm
strain along in-plane direction	0	+2.20%	0
roughness factor − σ	0.22	-	-
absorption factor − β	-	0.1	0.1

[a]At the (01*L*) CTR, the five topmost parameters are the same for the simulation produced in the interval from L = 12 to L = 15.

above it, which keeps the registry of the usual Bi_2Se_3 unit cell. Hence, the periodicities observed (correlation peaks along the CTR) correspond to the repetition of Bi_2 layers in the Bi_4Se_5 and BiSe phases. The correlation periodicity observed in the (00*L*) CTR is also retrieved at the (01*L*) data for the interval between L = 12 to L = 18. In Figure 2c the same structural parameters used in the (00*L*) were employed to produce the fit. The simultaneous fit of the (00*L*) and (01*L*) data shows that the structure used is correct.

In order to understand the composition evolution in this system, we carried out a controlled in situ annealing procedure. We used a furnace adapted to the diffractometer, and the temperature was ramped from 303 to 573 K, in 15 K steps. For each step, the temperature was achieved and the sample thermalized in 10 min. Then, both CTRs were measured within 1 h. The process showed an increase in the relative volume of Bi_4Se_5 domains, which indicates Se sublimation.[18] Figure 3a shows the detail of the vicinity of the (0 0 21) Bi_2Se_3 peak, where the intensity contributions from Bi_4Se_5 and BiSe were retrieved from CTR fits. From these fits, the volume of each phase can be quantified, producing the scenario shown in Figure 3b. Among the major changes that take place over the temperature ramp, a reduction of intensity of the main Bi_2Se_3 phase is promptly observed. On the other hand, the volume of Bi_4Se_5 and BiSe phases increase. This indicates that the sublimation of Selenium atoms results in the creation of Bi_2 bilayers[13] inside the crystal, which impacts the volume of the phases observed at higher temperatures.

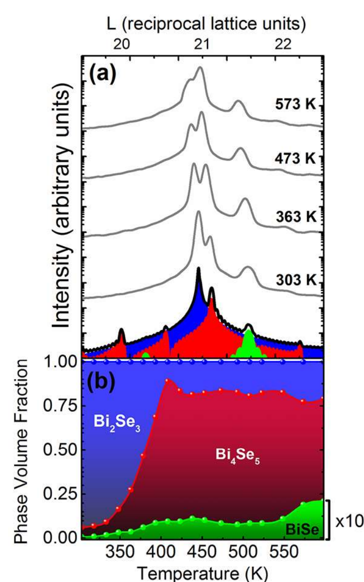

Figure 3. (a) Detail of the vicinity of the (0 0 21) peak of the (00*L*) CTR, showing the interplay of contributions of each Bi_xSe_y phase as the temperature changes, and the fitted curve for 303 K (bottom curves). (b) Order parameter (relative phase amplitudes) plotted with respect to the temperature along the studied range.

Our unit cell, used for CTR simulation of Bi_4Se_5, is formed by five Bi_2Se_3 quintuple-layers and a Bismuth bilayer on top of it. This unit cell can be understood as two unit cells of Bi_2Se_3 with the topmost quintuple layer replaced by a pure Bismuth bilayer. As already discussed in previous works, the main phases of Bismuth Selenide are formed by the intercalation of Bi_2Se_3 quintuple-layers and Bi_2 bilayers[19]. X-ray diffraction techniques are known to provide information about the bulk structure of crystalline samples (penetration depth ranging from few to ten or more micrometers[17]). Although the analysis of the CTR diffraction can directly reveal details of the surface structure (mainly between bulk Bragg peaks), such information is averaged over the X-ray spot area.[17] Near Bragg peaks, bulk diffraction overcomes surface components.

To understand this issue, STM and STS techniques were carried out in selected regions of the sample, revealing local morphological and electronic aspects that cannot be captured by solving the CTR data. These measurements were conducted on an as-grown sample and one sample annealed at 573 K. Since STS results require an interpretation of spectroscopic data, it is mandatory to understand the band structure of the retrieved dominant phases: Bi_2Se_3 and Bi_4Se_5. Density functional theory (DFT) calculations were performed to address this issue.

The structural models employed in the DFT calculations were built with the assumption that distinct phases are obtained with the addition of a Bi_2 bilayer to a supercell of five quintuple layers (QLs). All geometries were fully relaxed with a lattice parameter fixed in the experimental value of 0.414 nm. The band structures and the corresponding density of states (DOS) for Bi_2Se_3 (five QLs) are shown in Figure 4a for comparison purposes. Three distinct arrangements for the Bi_2 bilayer were then considered in the calculations, with respect to the surface location. From surface to bottom, these combinations are of the type Bi_2/5QLs (Figure 4b), QL/Bi_2/5QLs (Figure 4c) and 2QLs/Bi_2/4QLs (Figure 4d). The distances between the selenium plane and the neighbor(s) bismuth plane(s) of the Bi_2 bilayer were found to be 0.256 nm for Bi_2 bilayer on the surface, and between 0.248 and 0.249 nm, for the other cases. These values are in excellent agreement (within 2%) with similar calculations, which explicitly include van der Waals contributions in the description of the exchange-correlation

DOI: 10.1021/acs.jpclett.7b03172
J. Phys. Chem. Lett. 2018, 9, 954−960

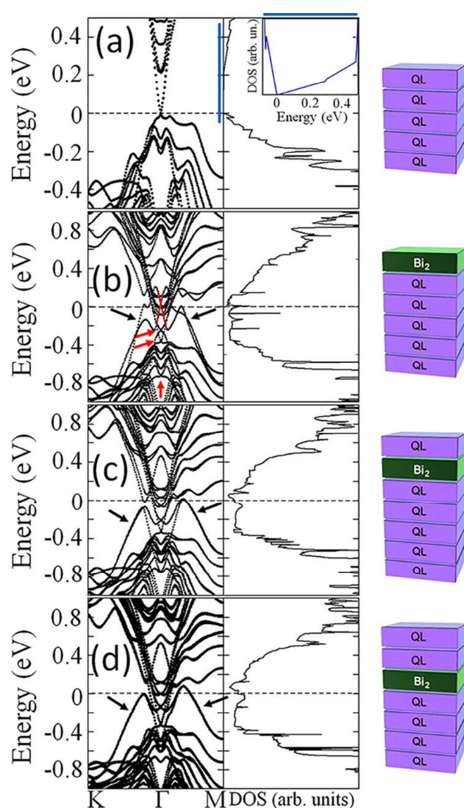

Figure 4. DFT calculations for Bi_2Se_3 and Bi_4Se_5. Left, central, and right panels correspond to band structure, density of states, and schematic structural configurations, respectively. Four cases are shown: (a) five QLs (Bi_2Se_3) with a inset of the interval marked by a blue line showing the Dirac cone on the DOS; (b) five QLs with a Bi_2 bilayer on the top surface; (c) six QLs, with a Bi_2 bilayer placed before the topmost QL; (d) six QLs, with a Bi_2 bilayer placed after four QLs and followed by the two topmost QLs. The M-shaped bands, signature of a Bi_2 bilayer on top of Bi_2Se_3, are indicated by black arrows. Red arrows in panel b indicate the Dirac cones.

functional.[14] Using the Bi_2Se_3 case as reference, the bands originated from the additional Bi_2 may be easily identified. In particular, the two shoulders forming an M-shaped band (indicated by black arrows in Figure 4b−d), which appear close to the Fermi level (set to zero), are signatures of the Bi_2 bilayer on top of 3D TIs.[20] For the Bi_2 bilayer on top of the slab, a Dirac cone is found at the Fermi level (emphasized by red lines directly depicted in the band structure of Figure 4b), representing topological states predominantly localized at the bilayer. Other Dirac cones can be seen in the band structure: they are indicated by red arrows in Figure 4b and represent topological states located in the QLs,[14] which moved to lower energies due to a charge transfer effect. In the topmost QL, close to the Bi_2 bilayer, such states have been reported in the literature as interface topological states.[14]

The presence of helical states associated with these cones could be analyzed by using a noncollinear spin scheme[21] which allows the determination of a charge contribution for each state labeled by n and k. These quantities can be projected in a basis formed by the unit matrix and Pauli matrices, from which the angles that characterize the spin polarization vector may be calculated. A similar procedure leads to a spin polarization vector in real space (starting from the real space density matrix).[21] When more QLs are placed on top of the Bi_2, the charge transfer process is intensified, which contribute to the shift of Bi_2 bands (indicated by arrows in Figures 4c,d) higher in energy. Several sharp peaks appear in the DOS, most of them originating from Rashba-split quantum-well states.[14] In general, these band structures agree with the results reported by Govaerts et al.[14] An important feature that distinguishes the cases in which the Bi_2 bilayers are present from the pure QLs is the presence of conduction bands in the energy range 0.1−0.2 eV extending in the Γ-M direction. When the Bi_2 bilayer is found on top of the five QLs (Figure 4b), these bands, which are predominantly localized in the topmost QL,[14] contribute to enlarge and broaden the DOS peak around 0.15 eV. As we shall show, this feature is important in the interpretation of STS measurements.

The search for Bi_4Se_5 regions was carried out via STM looking at localized (nonextended) steps with less than 1 nm height on the sample surface. Our description focuses on the sample heated up to 573 K. These steps can represent Bismuth bilayers at the surface or configurations with buried Bi bilayers, like described in Figure 4. We found that there is an existence of Bi_2Se_3 and Bi_4Se_5 regions along the sample surface, which in turn can be studied to provide a deeper understanding of the Bi_4Se_5 formation. We start our discussion with Figure 5, where we present STM images of bismuth selenide at room temperature. These images were obtained on a cleaved surface of the sample (the cleaving procedure was done inside the vacuum chamber). Current/voltage conditions for all measurements are declared in the figure captions. The topographic image of Figure 5a, combined with the line profile displayed in Figure 5b, reveals typical Bi_2Se_3 QL 1 nm steps on the surface. Figure 5c shows a typical region where Bi_4Se_5 is formed, with a line profile depicted in Figure 5d. In this case, one observes the presence of nanograins with height steps of 0.4 nm (typical from the Bismuth bilayers). A closer look to a Bi_4Se_5 nanograin is shown in Figure 5e with an atomically resolved image displayed in Figure 5f. A hexagonal lattice is found over the Bismuth bilayer surface, with an in-plane lattice parameter of 0.461 nm.

Some nanograins as the one shown in Figure 5b have bilayers inside QLs. In these grains, step heights that denote the inner presence of Bi_2 bilayers are found, such as 1.4 and 0.6 nm. In other cases, the grains have a step of 1 nm height difference from the Bi_2Se_3 surface, presenting an additional 0.4 nm steps inside them. We speculate that during sample annealing selenium atoms flow out of the region through grain boundaries and defects, allowing the formation of stable Bismuth bilayers between stacks of five quintuple layers, forming the Bi_4Se_5 phase.

In order to confirm and correlate the results from DFT and STM, we have carried out STS measurements, which provide the local electronic density of states of grains and plateaus, such as the topographic configuration shown in Figure 6a. Grain sizes and lateral widths were evaluated from height profiles, as shown in Figure 6b. We have collected STS spectra on top of 40 nanograins and over several areas of flat surface, corresponding to Bi_2Se_3 plateaus. Local STS spectra (e.g., Figure 6c) were extracted from the average response of 100 *I*−*V* curves, while for STS line scans each spectrum is averaged over 10 *I*−*V* curves. The STS measurement of Bi_2Se_3 shown in Figure 6c was measured in a region far away from nanograins, to avoid possible interferences from these structures. In Figure 6c, the black curve represents an STS spectrum of the Bi_2Se_3

DOI: 10.1021/acs.jpclett.7b03172
J. Phys. Chem. Lett. 2018, 9, 954−960

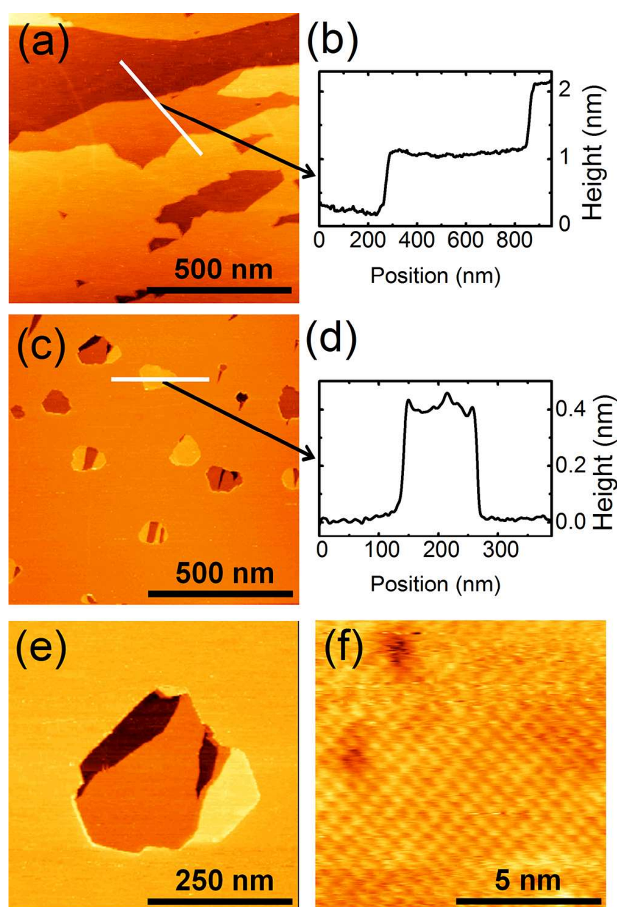

Figure 5. STM results on Bi_2Se_3−Bi_4Se_5 for a sample heated up to 573 K. (a) Low-resolution image of the Bi_2Se_3 surface (as-grown, unheated sample). (b) Line-profile of the Bi_2Se_3 surface (as-grown, unheated sample). (c) Low-resolution image of a Bi_4Se_5-rich surface. (d) Line-profile of a nanograin on the Bi_4Se_5-rich surface. (e) Closer look at a Bi_4Se_5 nanograin. (f) Atomic-resolution image of the Bi_4Se_5 surface, terminated in a Bi_2 bilayer.

region, exhibiting the expected Bi_2Se_3 topological insulator behavior near the Dirac point. Selected STS measurements on different surface terminations for nanograins that contain Bi_2 layers are plotted in blue (bilayer termination) and red (QL termination). One observes that the nanograin has a conducting behavior since the dI/dV values in both blue and red curves are finite at $V = 0$. These nanograin regions exhibit modified signatures of topological insulator, since a constant conduction value is added. For the bilayer terminated region of the nanograin (blue curve), one observed an inflection of the curve around −0.3 eV. While the regions of the nanograins which are terminated in QLs exhibit a response which is similar to the bulk topological insulator spectrum, the addition of Bismuth bilayers tend to modify the STS response due to the formation of new conducting channels. Such behavior is also found on the DFT calculations shown in Figure 4, where additional bands with respect to Figure 4a are found closer to the Fermi level.

To analyze the transition from the Bi_2Se_3 QLs behavior to the conducting Bi_4Se_5 response, we performed STS line profiles, crossing nanograins. Figure 6d shows a collection of dI/dV curves as the tip moves from the Bi_2Se_3 plateau into the

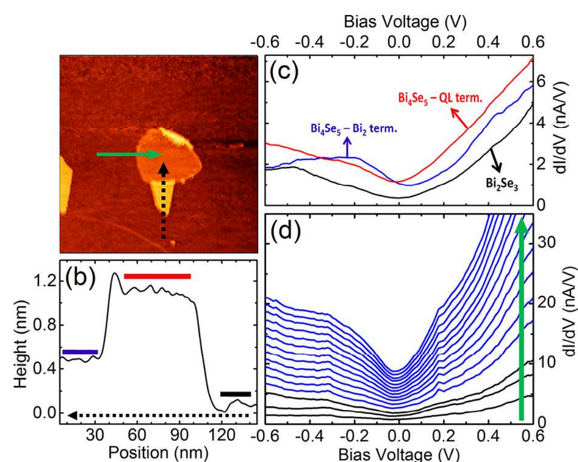

Figure 6. STM results. (a) STM image of a region of Bi_2Se_3 with a Bi_4Se_5 nanograin. (b) Line height profile of the nanograin, carried out along the dashed black vertical line in panel a. (c) STS on the three regions of the image: (1) Bi_4Se_5 terminated into a QL (red); (2) Bi_4Se_5 terminated into a Bi_2 bilayer (blue); (3) Bi_2Se_3 flat surface (black). (d) STS profiles measured along the green horizontal line in panel a. Blue curves represent the Bi_2 bilayer termination, while the black curves represent Bi_2Se_3.

nanograin of Figure 6a, showing a tendency of conductance values at $V = 0$ to drift away from zero. In brief, Bismuth bilayers on top (blue curves in Figure 6d), or even inside the Bi_2Se_3 matrix (black curves in Figure 6d) change the local electronic behavior of Bi_2Se_3. This is compatible with the introduction of a STS peak around 0.2 eV as pointed out from DFT calculations for Bi_4Se_5. We also observe an overall shape change of the STS curves from flat areas to nanograins, where the usual "V" shape from TIs is replaced by a curvature inflection for applied bias values lower than −0.3 V.

Using a combination of STM/STS measurements and X-ray diffraction experiments, we were able to infer the electronic density of states and the crystal structure of Bi_4Se_5 nanograins that appear at the Bi_2Se_3 surface upon annealing. The (00L) and (01L) CTRs provide structural parameters and relative volume of each phase on a polyphase Bi_2Se_3−Bi_4Se_5 crystal. Heating the material up to 573 K, one observed the reduction of the Bi_2Se_3 phase with the concomitant formation of Bi_4Se_5. Bi_4Se_5 nanograins were found by STM and first identified by their typical 0.4 nm height steps.

STS experiments were carried inside and outside these nanograins and compared with DFT calculations. While the spectra outside the nanograins (flat regions with only Bi_2Se_3) showed the expected topological insulator behavior, a conducting behavior was retrieved inside these nanograins. STS line-scan spectra, entering into a nanograin, showed the transition from the topological insulator to a conducting phase. Then spectral response of these grains shows an inflection for $V < -0.3$ V. It is not possible, however, to experimentally infer whether such conductor state is caused by modifications of bulk or surface states. A possible way to answer this question is to carry out angle-resolved photoemission spectroscopy (ARPES) at a single nanograin.[22] This requires a focused ultraviolet nanobeam in a very specific area of an ordinary sample. Another perspective revealed in the present work is related to the fact that bismuth bilayers are two-dimensional topological insulators.[23] This means that a Bi_2Se_3−Bi_4Se_5 sample obtained upon heating could be of interest for further studies, since this

DOI: 10.1021/acs.jpclett.7b03172
J. Phys. Chem. Lett. 2018, 9, 954−960

system combines two- and three-dimensional topological insulators.[24]

METHODS

Bi_2Se_3–Bi_4Se_5 crystals were prepared in a quartz tube furnace at the Physics Department of UFMG (Belo Horizonte, Brazil). Bulk (1 mm diameter 99.999%) Bi and Se spheres were inserted in the furnace, encapsulated in an evacuated quartz tube, at a 2:3 molar proportion. The furnace was ramped up to 1023 K from room temperature at a rate of 2 K/min and remained in this temperature for 40 h. After temperature quenching (the furnace was switched off), several 5 mm × 5 mm × 2 mm pieces of Bi_2Se_3–Bi_4Se_5 crystals were produced. Quenching to room temperature was achieved after 4 h, due to the total furnace mass. After extracting these crystals from the resulting material, they were freshly cleaved by scotch tape prior to the experimental measurements. X-ray diffraction measurements were carried out in the six-circle diffractometer of the XRD2 beamline of the Brazilian Synchrotron Light Laboratory (LNLS - Campinas). The X-ray energy was fixed to 10 keV, and a Pilatus 100 K detector was used to map out the reciprocal space along the Bi_2Se_3 (00*L*) and (01*L*) truncation rods. A variable temperature scanning tunneling microscope (VT-STM; Omicron GmbH) was used in our experiment. The equipment is located at the UHV Nanoscopy Laboratory at UFMG. All STM images were obtained in a vacuum pressure better than 1×10^{-10} mBar. STS measurements were performed at 25 K using a liquid helium transfer system, using a lock-in amplifier working at 3.03 kHz to filter the I–V signal measurements obtained in spectroscopy mode. For further details, see ref 25.

DFT calculations were performed within the QUANTUM-ESPRESSO[26] implementation. The cutoff energy in the plane wave expansion of the Kohn–Sham eigenstates was set to 35 Ry, and the Perdew–Burke–Ernzerhof (PBE)[27] parametrization for the exchange-correlation functional was adopted. We made use of the projector augmented wave (PAW) framework (potentials Bi.rel-pbe-dn-kjpaw.UPF and Se.rel-pbe-n-kjpaw.UPF). The geometries were considered relaxed when the remanent force component in any atom was less than 1.0×10^{-3} u.a.

AUTHOR INFORMATION

Corresponding Author

*E-mail: angelomalachias@gmail.com.

ORCID

D. D. dos Reis: 0000-0003-1151-7745

Carolina Parra: 0000-0003-3819-7614

Ângelo Malachias: 0000-0002-8703-4283

Notes

The authors declare no competing financial interest.

ACKNOWLEDGMENTS

The authors acknowledge experimental support by the Brazilian Synchrotron Light Source (LNLS). Financial support was provided by Instituto Nacional de Ciência e Tecnologia (INCT-NanoCarbono). We also acknowledge additional funding by CNPq, CAPES, FAPEMIG and Fondecyt.

REFERENCES

(1) Bansil, A.; Lin, H.; Das, T. Colloquium: Topological Band Theory. *Rev. Mod. Phys.* **2016**, *88*, 021004.

(2) Hsieh, D.; Qian, D.; Wray, L.; Xia, Y.; Hor, Y. S.; Cava, R. J.; Hasan, M. Z. A Topological Dirac Insulator in a Quantum Spin Hall Phase. *Nature* **2008**, *452*, 970–974.

(3) Chen, Y. L.; Analytis, J. G.; Chu, J.-H.; Liu, Z. K.; Mo, S.-K.; Qi, X. L.; Zhang, H. J.; Lu, D. H.; Dai, X.; Fang, Z.; et al. Experimental Realization of a Three-Dimensional Topological Insulator. *Science* **2009**, *325*, 178–181.

(4) Zhu, Z.; Cheng, Y.; Schwingenschlögl, U. Band Inversion Mechanism in Topological Insulators: A Guideline for Materials Design. *Phys. Rev. B: Condens. Matter Mater. Phys.* **2012**, *85*, 235401.

(5) Hsieh, D.; Xia, Y.; Qian, L.; Wray, L.; Meier, F.; Dil, J. H.; Osterwalder, J.; Patthey, L.; Fedorov, A. V.; Lin, H.; et al. Observation of Time-Reversal-Protected Single-Dirac-Cone Topological-Insulator States in Bi_2Te_3 and Sb_2Te_3. *Phys. Rev. Lett.* **2009**, *103*, 146401.

(6) Roushan, P.; Seo, J.; Parker, C. V.; Hor, Y. S.; Hsieh, D.; Qian, D.; Richardella, A.; Hasan, M. Z.; Cava, R. J.; Yazdani, A. Topological Surface States Protected from Backscattering by Chiral Spin Texture. *Nature* **2009**, *460*, 1106–1109.

(7) Zhang, H.; Liu, C.-X.; Qi, X.-L.; Dai, X.; Fang, Z.; Zhang, S.-C. Topological Insulators in Bi_2Se_3, Bi_2Te_3 and Sb_2Te_3 with a Single Dirac Cone on the Surface. *Nat. Phys.* **2009**, *5*, 438–442.

(8) Hasan, M. Z.; Kane, C. L. Colloquium: Topological Insulators. *Rev. Mod. Phys.* **2010**, *82*, 3045–3068.

(9) Götte, M.; Joppe, M.; Dahm, T. Pure Spin Current Devices Based on Ferromagnetic Topological Insulators. *Sci. Rep.* **2016**, *6*, 36070.

(10) Zhang, H. B.; Li, H.; Shao, J. M.; Li, S. W.; Bao, D. H.; Yang, G. W. High-Performance Bi_2Te_3-Based Topological Insulator Film Magnetic Field Detector. *ACS Appl. Mater. Interfaces* **2013**, *5*, 11503–11508.

(11) Murakami, S. Quantum Spin Hall Effect and Enhanced Magnetic Response by Spin-Orbit Coupling. *Phys. Rev. Lett.* **2006**, *97*, 236805.

(12) Shokri, R.; Meyerheim, H. L.; Roy, S.; Mohseni, K.; Ernst, A.; Otrokov, M. M.; Chulkov, E. V.; Kirschner, J. Atomic and Electronic Structure of Bismuth-Bilayer-Terminated Bi_2Se_3 (0001) Prepared by Atomic Hydrogen Etching. *Phys. Rev. B: Condens. Matter Mater. Phys.* **2015**, *91*, 205430.

(13) Coelho, P.; Ribeiro, G.; Malachias, A.; Pimentel, V.; Silva, W.; Reis, D.; Mazzoni, M.; Magalhães-Paniago, R. Temperature-Induced Coexistence of a Conducting Bilayer and the Bulk-Terminated Surface of the Topological Insulator Bi_2Te_3. *Nano Lett.* **2013**, *13*, 4517–4521.

(14) Govaerts, K.; Park, K.; De Beule, C.; Partoens, B.; Lamoen, D. Effect of Bi Bilayers on the Topological States of Bi_2Se_3: A First-Principles Study. *Phys. Rev. B: Condens. Matter Mater. Phys.* **2014**, *90*, 155124.

(15) Okamoto, H. The Bi-Se (Bismuth-Selenium) System. *J. Phase Equilib.* **1994**, *15*, 195–201.

(16) Robinson, I. K. Crystal Truncation Rods and Surface Roughness. *Phys. Rev. B: Condens. Matter Mater. Phys.* **1986**, *33*, 3830–3836.

(17) Als-Nielsen, J.; McMorrow, D. *Elements of modern X-ray physics*; John Wiley & Sons: Chichester, U.K.; 2011.

(18) Buha, J.; Gaspari, R.; Del Rio Castillo, A.; Bonaccorso, F.; Manna, L. Thermal Stability and Anisotropic Sublimation of Two-Dimensional Colloidal Bi_2Te_3 and Bi_2Se_3 Nanocrystals. *Nano Lett.* **2016**, *16*, 4217–4223.

(19) Lee, P.; Kim, J.; Kim, J. G.; Ryu, M.; Park, H.; Kim, N.; Kim, Y.; Lee, N.-S.; Kioussis, N.; Jhi, S.-H.; et al. Topological Modification of the Electronic Structure by Bi-bilayers Lying Deep Inside Bulk Bi_2Se_3. *J. Phys.: Condens. Matter* **2016**, *28*, 085002.

(20) Hirahara, T.; Bihlmayer, G.; Sakamoto, Y.; Yamada, M.; Miyazaki, H.; Kimura, S.-i.; Blügel, S.; Hasegawa, S. Interfacing 2D and 3D Topological Insulators: Bi(111) Bilayer on Bi_2Te_3. *Phys. Rev. Lett.* **2011**, *107*, 166801.

(21) Zhao, Y.; Hu, Y.; Liu, L.; Zhu, Y.; Guo, H. Helical States of Topological Insulator Bi_2Se_3. *Nano Lett.* **2011**, *11*, 2088–2091.

(22) Arango, Y. C.; Huang, L.; Chen, C.; Avila, J.; Asensio, M. C.; Grützmacher, D.; Lüth, H.; Lu, J. G.; SchäPers, T. Quantum Transport and Nano Angle-resolved Photoemission Spectroscopy on the

DOI: 10.1021/acs.jpclett.7b03172
J. Phys. Chem. Lett. 2018, 9, 954–960

Topological Surface States of Single Sb_2Te_3 Nanowires. *Sci. Rep.* **2016**, *6*, 29493.
(23) Drozdov, I. K.; Alexandradinata, A.; Jeon, S.; Nadj-Perge, S.; Ji, H.; Cava, R. J.; Bernevig, B. A.; Yazdani, A. One-Dimensional Topological Edge States of Bismuth Bilayers. *Nat. Phys.* **2014**, *10*, 664−669.
(24) Zhang, K. F.; Yang, F.; Song, Y. R.; Liu, C.; Qian, D.; Gao, C. L.; Jia, J.-F. Strongly Compressed Bi (111) Bilayer Films on Bi_2Se_3 Studied by Scanning Tunneling Microscopy. *Appl. Phys. Lett.* **2015**, *107*, 121601.
(25) Parra, C.; Rodrigues da Cunha, T.; Contryman, A.; Kong, D.; Montero-Silva, F.; Rezende Gonçalves, P.; Dos Reis, D.; Giraldo-Gallo, P.; Segura, R.; Olivares, F.; et al. Phase Separation of Dirac Electrons in Topological Insulators at the Spatial Limit. *Nano Lett.* **2017**, *17*, 97−103.
(26) Giannozzi, P.; Baroni, S.; Bonini, N.; Calandra, M.; Car, R.; Cavazzoni, C.; Ceresoli, D.; Chiarotti, G. L.; Cococcioni, M.; Dabo, I.; et al. QUANTUM ESPRESSO: a Modular and Open-Source Software Project for Quantum Simulations of Materials. *J. Phys.: Condens. Matter* **2009**, *21*, 395502.
(27) Perdew, J.; Burke, K.; Ernzerhof, M. Generalized Gradient Approximation Made Simple. *Phys. Rev. Lett.* **1996**, *77*, 3865−3868.

DOI: 10.1021/acs.jpclett.7b03172
J. Phys. Chem. Lett. 2018, 9, 954−960

NANO LETTERS
Letter
pubs.acs.org/NanoLett

Phase Separation of Dirac Electrons in Topological Insulators at the Spatial Limit

Carolina Parra,[*,†,‡,§] Thiago Henrique Rodrigues da Cunha,[‖] Alex W. Contryman,[⊥] Desheng Kong,[§,#,○] Francisco Montero-Silva,[†] Pedro Henrique Rezende Gonçalves,[▽] Diogo Duarte Dos Reis,[▽] Paula Giraldo-Gallo,[◆] Rodrigo Segura,[□] Fernanda Olivares,[□] Francis Niestemski,[‡,§] Yi Cui,[§,#] Rogerio Magalhaes-Paniago,[▽] and Hari C. Manoharan[‡,§]

[†]Laboratorio Nanobiomateriales, Departamento de Física, Universidad Técnica Federico Santa María, Avenida España, 1680, Valparaíso, Chile

[‡]Department of Physics, Stanford University, Stanford, California 94305, United States

[§]Stanford Institute for Materials and Energy Sciences, SLAC National Accelerator Laboratory, Menlo Park, California 94025, United States

[‖]CTNanotubos, Universidade Federal de Minas Gerais, Rua Professor José Vieira de Mendonça 1.000, Engenho Nogueira, BH, Brazil

[⊥]Department of Applied Physics, Stanford University, Stanford, California 94305, United States

[#]Department of Materials Science and Engineering, Stanford University, Stanford, California 94305, United States

[○]National Laboratory of Solid State Microstructure, College of Engineering and Applied Sciences, and Collaborative Innovation Center of Advanced Microstructures, Nanjing University, Nanjing 210093, China

[▽]Departamento de Física, Universidade Federal de Minas Gerais, CP 702 Belo Horizonte, MG CEP 30123-970, Brazil

[◆]National High Magnetic Field Laboratory, Tallahassee, Florida 32310, United States

[□]Instituto de Química y Bioquímica, Facultad de Ciencias, Universidad de Valparaíso, Av. Gran Bretaña, 1111 Valparaíso, Chile

Supporting Information

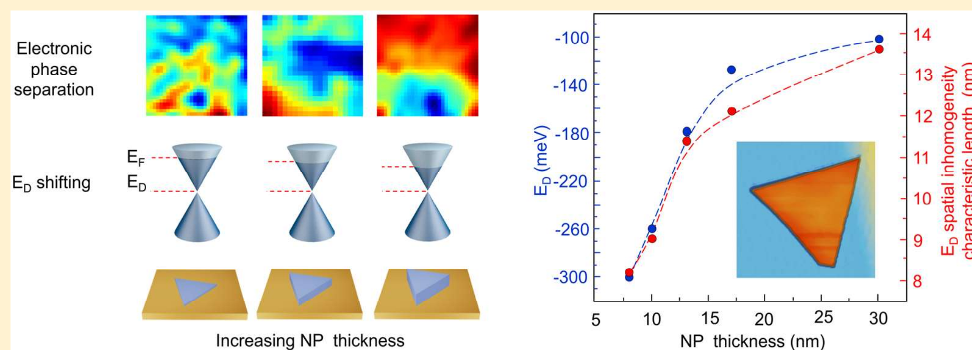

ABSTRACT: In this work we present unique signatures manifested by the local electronic properties of the topological surface state in Bi_2Te_3 nanostructures as the spatial limit is approached. We concentrate on the pure nanoscale limit (nanoplatelets) with spatial electronic resolution down to 1 nm. The highlights include strong dependencies on nanoplatelet size: (1) observation of a phase separation of Dirac electrons whose length scale decreases as the spatial limit is approached, and (2) the evolution from heavily n-type to lightly n-type surface doping as nanoplatelet thickness increases. Our results show a new approach to tune the Dirac point together with reduction of electronic disorder in topological insulator (TI) nanostructured systems. We expect our work will provide a new route for application of these nanostructured Dirac systems in electronic devices.

KEYWORDS: *Topological insulator nanostructures, Bi_2Te_3, Dirac electrons, scanning tunneling spectroscopy, phase separation, doping*

Recently both theoretical predictions and experimental measurements have demonstrated that Bi_2Te_3, a layered binary compound, is a three-dimensional (3D) topological insulator (TI), a new state of quantum matter with a bulk gap and massless Dirac surface states topologically protected with helical spin texture.[1]

The Fermi level in 3D TIs does not necessarily coincide with the Dirac point. In some of these materials, the Fermi level falls

Received: August 19, 2016
Revised: December 27, 2016
Published: December 27, 2016

ACS Publications © 2016 American Chemical Society

DOI: 10.1021/acs.nanolett.6b03506
Nano Lett. 2017, 17, 97−103

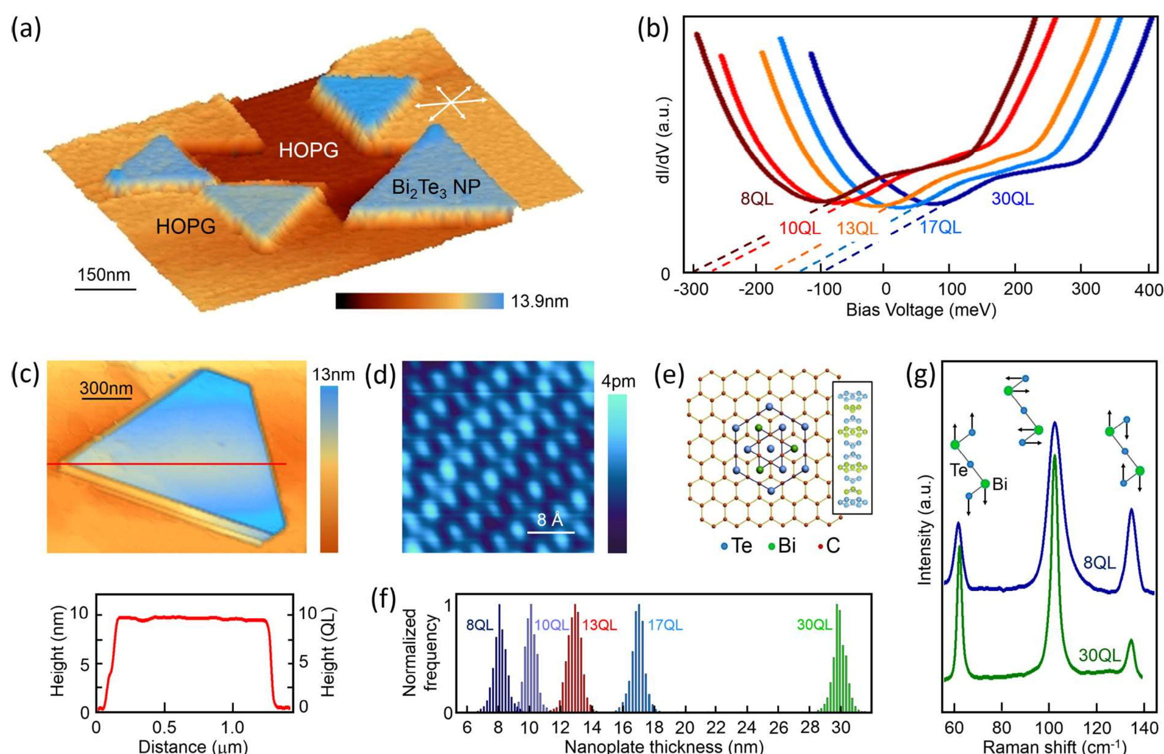

Figure 1. Structure and morphology of Bi_2Te_3 nanoplatelets. (a) STM image of a group of Bi_2Te_3 NPs grown on HOPG, V_S = 0.5 V, I = 1.0 pA. Nanoplatelets (in blue) with uniform thicknesses were aligned in the same orientation on the graphite layer (white arrows), an unequivocal sign of epitaxial growth. (b) Representative specs for Bi_2Te_3 NPs of five different thicknesses where a shift in Dirac energy was observed with respect to Fermi level. (c) Constant-current STM image of a triangular Bi_2Te_3 nanoplatelet grown on HOPG; V_S = 1 V, I = 1.0 pA, where V_S is the sample bias voltage with respect to the sample and I is the tunneling current (lower panel). Line profile along the red linecut shows that NP is 10 QL (~10 nm) in height and has a base length of 1.4 μm. (d) Atomically resolved STM image of Bi_2Te_3 nanoplatelet showing a lattice constant of 4.3 ± 0.3 Å. (e) Diagram showing final configuration for van der Waals epitaxial growth mode of Bi_2Te_3 on HOPG. Graphite exhibits a honeycomb lattice structure with C−C bond length of ~1.42 Å and Bi_2Te_3 with rhombohedral structure and a lattice constant of 4.38 Å. Lattice mismatch between substrate and Bi_2Te_3 is ~2.7%. (f) Height histogram for NPs used in the current study. (g) Raman spectra from as-grown 8 QL and 30 QL Bi_2Te_3 nanoplatelets with corresponding active Raman modes.

in either the conduction band or the valence band, and its position can strongly vary because of naturally occurring defects. In addition, a high density of charge carriers in their bulk generally mixes together bulk and surface transport characteristics. In order to separately access the remarkable properties of the surface carriers in TIs, it is vital to controllably suppress the bulk conductivity by constraining the Fermi level to the bulk bandgap.[2]

This limitation has triggered an intense search for clean TIs with the Fermi level occurring within the gap. One approach is controlling bulk carrier concentration by using an effective compensation dopant like Sn,[3,4] Cd,[4,5] Ca,[6−8] Pb,[9] Na,[10] or Sb.[11,12] However, a high dopant concentration can also introduce undesirable impurity scattering. The Fermi level in TIs can also be manipulated via gating,[13−15] structural deformation,[15,16] use of different substrates,[17] and control of thin film thickness.[18,19]

Low-dimensional TI materials, such as nanoribbons and nanoplatelets (NPs), have arisen as an excellent alternative in order to overcome the impurity scattering effect, favoring the manifestation and access to the surface states in transport measurements due to their very large surface-to-bulk ratios,[20,21] which reduce bulk carrier contribution in TI electron transport. These unique nanostructures also stand out as excellent candidates for making functional devices easy to manipulate and manufacture, creating an opportunity for versatile band structure engineering of the surface states.

To date, angle-resolved photoemission spectroscopy (ARPES) has been the predominantly used technique to determine TI band structure, employed mainly on TI thin films grown by MBE[18,22,23] and single-crystal samples cleaved in UHV conditions.[4−7] Some of these ARPES measurements, together with theoretical calculations, have revealed unconventional size effects like the evolution from 2D TI to 3D TI phase depending on film thicknesses in Bi_2Te_3[23] and Bi_2Se_3.[18] In contrast, STM and STS reports in TI crystals and MBE thin films[4,5,24,25] accessing local phenomena are less numerous than its momentum-resolved counterpart. Additionally, these studies have mainly focused on demonstrating the suppression of surface backscattering and the robust nature of MBE-grown TI systems.

Given the lack of STS measurements on TI nanostructures, we present in this work the first combined scanning tunneling microscopy (STM) and spectroscopy (STS) studies on high-quality epitaxial Bi_2Te_3 nanoplatelets grown by vapor−solid process. Here we concentrate uniquely on the nanoscale spatial limit of topological insulators (nanoplatelets), where all dimensions are well below 1 μm, in contrast to existing work in TI nanoplates.[20,21] We show that it is possible to tune the electronic properties of such high-quality TI nanomaterials

DOI: 10.1021/acs.nanolett.6b03506
Nano Lett. 2017, 17, 97−103

through its thickness, decreasing n-type charge carriers and local spatial electronic disorder as a function of thickness.

Bi_2Te_3 NPs were fabricated by a catalyst-free vapor transport and deposition process in a 12 in. horizontal tube furnace (Lindberg/Blue M) on HOPG substrate. The growth method is discussed in a previous work[20] (see Supporting Information, Figure S1 for details).

Although surface states of TIs are inherently robust against almost any surface modifications, these materials are prone to various surface chemical reactions, which are taken into account when preparing samples for devices and STM study. Particularly, continuous surface oxide growth has been observed in Bi_2Te_3[26] and Bi_2Se_3[27] after long exposure to oxygen-containing atmosphere, which causes a surface state degradation process after TI material interaction with the ambient environment. In our experiments the samples were transferred from the furnace to our STM chamber after exposure to air for just a few minutes. In order to remove the oxygen-containing layer adsorbed during transportation process (but do not change NP morphology), a few cycles of short sputtering at 200 eV were used followed by annealing at 130 C.

The final product is characterized by low temperature scanning tunneling microscopy and spectroscopy (Omicron LT-STM/STS). All topography scans were acquired in constant-current mode at 78 K in an ultrahigh vacuum chamber (pressure $<10^{-10}$ Torr) with a sample bias between 0.3 and 1 V and tunneling currents between 1 and 20 pA.

STM topography images show NPs that usually exhibit triangular and hexagonal morphologies with lateral dimensions extending up to several micrometers. A group of triangular nanoplatelets is shown in Figure 1a with color-scale representing the topographic height. Blue regions highlight NPs, whereas earth tones correspond to HOPG. In general, NPs have different thicknesses, which enable us to investigate the thickness-dependent band structure of Bi_2Te_3 NPs. Figure 1b shows a group of representative dI/dV spectra taken at the surface of NPs with different thicknesses.

We resolve the atomic lattice of a Bi_2Te_3 NP surface (Figure 1c) with a lattice constant of 4.3 ± 0.3 Å (Figure 1d). A linecut taken across these NPs shows uniform thickness and flat surface in the majority of the platelet. NP height is 10 quintuple layers (QL) as determined by the height histogram. Determined NP height is always consistent with the Bi_2Te_3 quintuple layer thickness. This correspondence suggests a quintuple layer-by-layer growth process for Bi_2Te_3 nanoplatelets.

Additionally, evidence of van der Waals epitaxial growth was found (Figure 1a) in areas where terrace edges in the substrate aligned with NP edges (NP aligned in the same orientation on the substrate). Even though, for this highly lattice-mismatched system (2.7% compressive strain, Figure 1e) the present van der Waals interface drastically relaxes the lattice matching condition encountered in heteroepitaxial growth.[28] Growth conditions for this system are far from those used in MBE (delicate control of temperature and deposition rate), which make the observed van der Waals epitaxial growth in this system remarkable. This growth mode would indicate a high crystalline quality of as-grown NPs.

Figure 1f shows the NP thickness used for the present study. Raman spectra for the thinnest (8 QL) and the thickest (30 QL) NP are shown in Figure 1g. A_{1g}^1 mode (out-of-plane mode at ~60 cm^{-1}) and E_g^2 mode (in-plane mode at ~102 cm^{-1}) are broader in the thinnest NP, which could be attributed to a previously reported disorder-induced inhomogeneous broadening and a stronger electron−phonon interaction with a concomitant reduction of phonon lifetime in TI nanostructures, which increases for thinner nanostructures.[29−31] Position of E_g^2 vibrational mode does not show a significant change, which suggests that the frequency of in-plane vibrations is not very sensitive to changes in thickness, in contrast to A_{1g}^1 and A_{1g}^2 (~132 cm^{-1}) out-of-plane vibrational modes, which shift when reducing NP thickness.

The spatial dependence of dI/dV spectra through a 50 nm linecut taken at 13 QL Bi_2Te_3 NP surface is shown in Figure 2a,

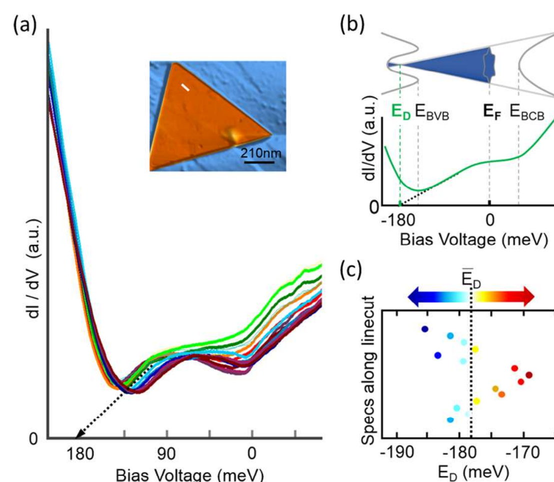

Figure 2. Spatial variation snapshots of the local density of states of Bi_2Te_3 nanoplatelets. (a) Measurements of dI/dV along a line of length 50 nm for a 13 QL. The zero-conductance point (intersection of black dashed line with 0 DOS) corresponds to the Dirac point (E_D) of the wrapped topological surface state. (b) Schematic of surface band structure and dI/dV spectrum of Bi_2Te_3 showing E_D and E_F positions. The position of the Dirac point for each spectrum is displayed in (c), where the dashed line corresponds to the mean E_D value for this nanoplatelet thickness.

providing the first glimpse of the spatial inhomogeneities and behavior analyzed in the rest of the letter. The Dirac energy (E_D) of the TI surface state (SS) for each spectrum can be obtained at the intersection of the black dashed line (extension of linearly dispersing TI surface state wrapped in bulk valence band) with zero conductance line (Figure 2b). The variations of E_D along the linecut are shown in Figure 2c with values fluctuating below (in blue) and above (in red) the mean E_D value (178 mV for this NP thickness). These local spatial fluctuations have been explored before in STS studies of doped Bi_2Te_3 crystals[32,33] and MBE thin films[34] but thus far never reported in a TI nanostructured system. Here we extend these measurements to the spatial limit.

The E_D variations for different NP thickness are quantified by the histograms seen in Figure 3a. A Gaussian has been fitted to each histogram to quantify the mean E_D value. The measured mean E_D values for different NP thickness are −301 mV for 8 QL, −260 mV for 10 QL, −178 mV for 13 QL, −127 mV for 17 QL, and −101 mV for 30 QL, indicating that E_D shifts to less negative energies when nanoplatelet thickness increases (Figure 3b). Variations of the E_D value reach a minimum for the thickest NPs, where there is a 1.5% variation around the mean E_D value (see Figure S2 for details). This variation increases for thinner nanoplatelets reaching a 14% for 10 QL and 7.3% for 8 QL.

DOI: 10.1021/acs.nanolett.6b03506
Nano Lett. 2017, 17, 97−103

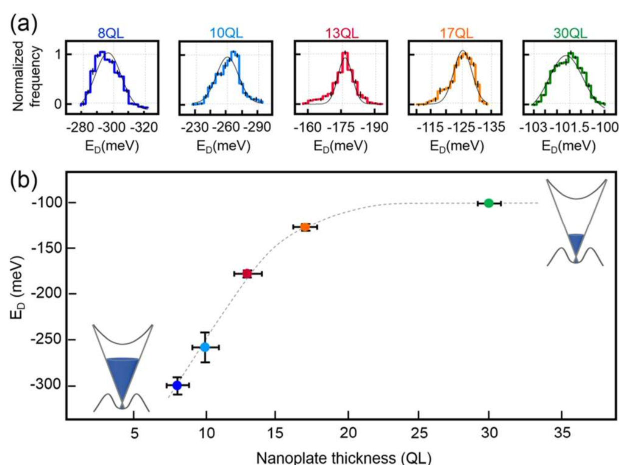

Figure 3. Bi_2Te_3 nanoplatelet thickness dependence of E_D position. (a) Histogram of E_D obtained from STS results on 8, 10, 13, 17, and 30 QL Bi_2Te_3 NPs at 78 K. A Gaussian has been fitted to each histogram to quantify fluctuations around the mean E_D value coming from STS spectra shifting. Slope variations of STS spectra are included as error bars in histograms. (b) E_D as a function of Bi_2Te_3 nanoplatelet thickness obtained from histogram in (a) with corresponding error bar. As nanoplatelet thickness increases E_D shifts to less negative energies.

As revealed by these STS measurements there is a clear thickness dependence of E_D position, showing an evolution from a heavily doped n-type to lightly doped n-type behavior. The as-grown Bi_2Te_3 compound has been reported to be either n- or p-type, depending on whether Te−Bi antisites or Te vacancies take the main role.[22,35,36] Both antisite defects (Te on Bi lattice and Bi on Te lattice) are energetically more favorable than possible vacancies in this material. However, only Bi-poor conditions (Te_{Bi}) lead to n-type transport properties.[37] The observed evolution of charge carrier doping in this nanostructured system might be a consequence of the reduction of Te_{Bi} antisite defects with Bi_2Te_3 NP thickness increase.

To visualize spatial variations we map the E_D values as a function of sample thickness with spatial resolution down to 1 nm (Figure 4). The color scale represents variation (inhomogeneity) in Dirac point with respect to Fermi level, ranging from −322 to −100 mV in real space (as seen in the color scale bar below each map). Percentage variation maps with respect to the mean E_D value are shown in Figure S2. From our local spectroscopic measurements no insulating signatures (coming from the insulating bulk state) for any NP thickness were observed.

To quantify the characteristic length scales of the E_D spatial inhomogeneity for each NP thickness, the average spatial correlation function $\langle G(\vec{r})\rangle$, and the angle-dependent spatial correlation function $\langle G_\theta(\vec{r})\rangle$ were computed for each E_D map (see Figures S3 and S4, respectively). The spatial autocorrelation function $G(\vec{r})$ of an image (STM image or STS map in our case) is defined as the statistical correlation of any two points separated by a vector $\vec{r} = \vec{r}_i - \vec{r}_j$ where $\vec{r}_i$ and $\vec{r}_j$ are the positions of those two points in the image.[38,39]

$$G(\vec{r}) = \frac{1}{N(\vec{r})} \sum_{i,j} \frac{(I_i - \langle I\rangle_1)(I_j - \langle I\rangle_2)}{\sigma_1\sigma_2}$$

where

$$N(\vec{r}) = \sum_{i,j} \delta_{\vec{r},(\vec{R}_i - \vec{R}_j)}$$

indicates the number of points at distance $\vec{r} = \vec{R}_i - \vec{R}_j$.

The average intensities (height value in an STM image or Dirac point value in an STS map) are calculated according to the expressions:

$$\langle I\rangle_1 = \sum_{i,j} \delta_{\vec{r},(\vec{R}_i - \vec{R}_j)} I_i$$

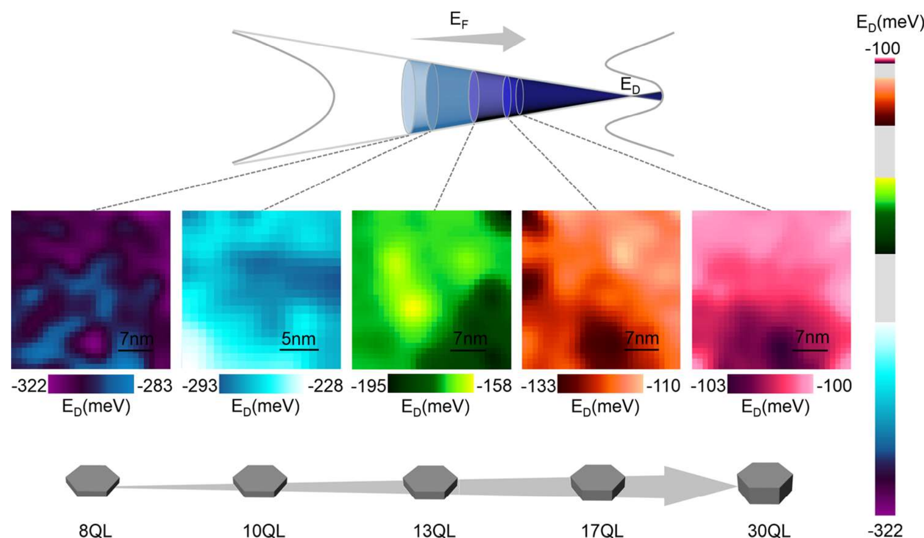

Figure 4. Spatial dependence of E_D as a function of Bi_2Te_3 nanoplatelet thickness. Map of spatial variations of the Dirac point, deduced from STS experiments for different Bi_2Te_3 NP thicknesses. Maps for 8 QL, 13 QL, 17 QL, and 30 QL are 30 × 30 nm², whereas for 10 QL is 20 × 20 nm². E_D variations range from −322 to −100 mV, with E_D overall values approaching E_F as NP thickness increases. Corresponding E_D values are represented by the color scale bar below each map. The right color scale bar shows the entire E_D range.

DOI: 10.1021/acs.nanolett.6b03506
Nano Lett. 2017, 17, 97−103

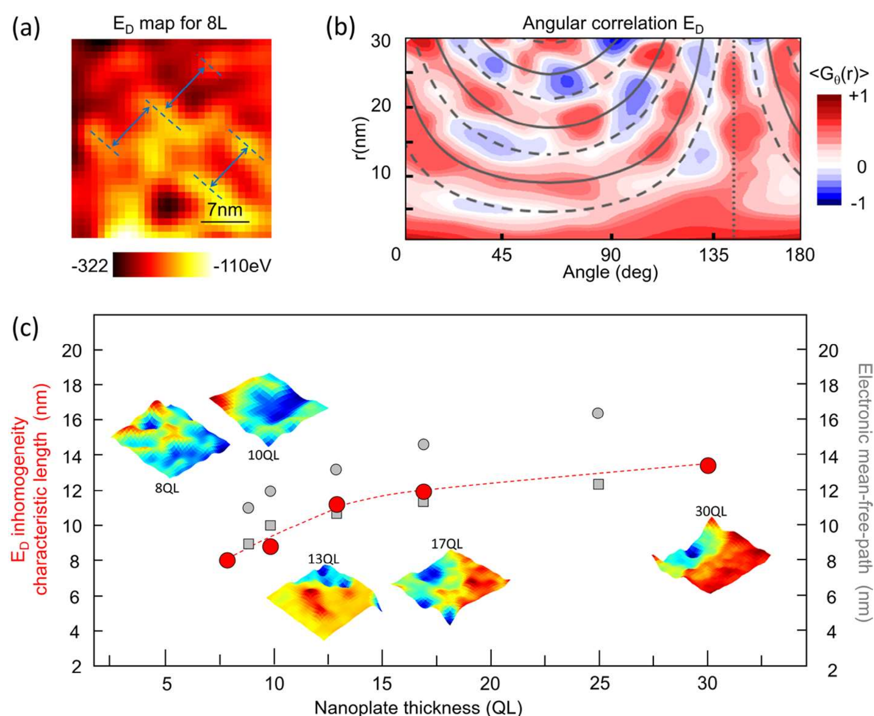

Figure 5. Thickness dependence of E_D inhomogeneity characteristic length. (a) Real space 8 QL E_D map with guidelines (in blue) to highlight the observed repeating structure. (b) Angle-dependent correlation $\langle G_\theta(\vec{r})\rangle$ analysis for 8 QL E_D map clearly shows an arc pattern, which is consistent with the real space phase separation in E_D map (See Figure S4 for other thicknesses). (c) Characteristic length scale of observed E_D spatial inhomogeneity was obtained from angular correlation analysis of STS E_D maps. E_D maps for each thickness are included as 3D images. Bulk valence (gray squares) and conduction band (gray circles) mean free path versus thickness for fully diffuse surface scattering from ref 40 are also shown for comparison purposes.

$$\langle I\rangle_2 = \sum_{i,j} \delta_{\vec{r},(\vec{R}_i-\vec{R}_j)} I_j$$

And the standard deviations are calculated according to

$$\sigma_1^{\;2} = \left(\frac{1}{N(\vec{r})}\sum_{i,j}\delta_{\vec{r},(\vec{R}_i-\vec{R}_j)} I_i^{\;2}\right) - (\langle I\rangle_1)^2$$

$$\sigma_2^{\;2} = \left(\frac{1}{N(\vec{r})}\sum_{i,j}\delta_{\vec{r},(\vec{R}_i-\vec{R}_j)} I_j^{\;2}\right) - (\langle I\rangle_2)^2$$

The average spatial autocorrelation function $\langle G(\vec{r})\rangle$ is the result of averaging the correlation function of all vectors with the same magnitude $|\vec{r}|$. The angle-dependent autocorrelation function $\langle G_\theta(\vec{r})\rangle$ is the result of averaging the correlation function of all vectors with orientation θ with respect to the horizontal axis and magnitude $|\vec{r}|$.

Both $\langle G(\vec{r})\rangle$ and $\langle G_\theta(\vec{r})\rangle$ of all the E_D maps reveal that there is a particular spatial pattern (with local minima and maxima), implying the presence of characteristic length scales for the observed spatial E_D inhomogeneity. The arcs in such pattern are imperfect, but repeat with a fixed periodicity, as clearly seen for the 8 QL map (Figure 5a,b), implying a pattern of phase separation of low and high carrier density domains over large length scales. The functional form of those arcs, for a system with partially disordered regions separated by a distance d and running along an angle α with respect to the horizontal, measured at an angle θ, is given by $Nd/\cos((\alpha - 90°) - \theta)$[41] (see Figure S4 for details). For real space 8 QL E_D map (Figure 5a), guidelines (in blue) highlight the observed repeating structure, which is consistent with results from angle-dependent correlation $\langle G_\theta(\vec{r})\rangle$ analysis.

In addition, close to zero cross-correlation values between E_D maps and topographies for all NP thicknesses suggest that electronic order is disconnected from local structural disorder (Figure S3). These results provide evidence that the observed phase separation of the Dirac electrons in Bi_2Te_3 NPs, which occurs in the form of stripe-like structures at repeat length d, may be self-organized. In contrast to electron−hole puddles in graphene[42] the E_D inhomogeneities observed here are actually spatially correlated with each other and to the nanoscale dimensions of the host material.

To further illustrate this point, the characteristic length scale d of such E_D spatial inhomogeneities obtained from $\langle G_\theta(\vec{r})\rangle$ analysis as a function of NP thickness is shown in Figure 5c. d values (red circles) increase with thickness, ranging from 8.2 to 13.5 nm. Electronic mean free path for bulk Bi_2Te_3 are included for reference purposes. The observed length scale increase can be interpreted as a reduction of spatial electronic disorder for thicker nanoplatelets (probably connected to the decrease of Te_{Bi} antisite defects), which is in agreement with the observed broadening of Raman spectra for thinner nanostructures. Such decreases in spatial electronic disorder with thickness suggests that electron-disorder scattering gets stronger for thinner nanoplatelets. This is in agreement with the observed evolution of the system toward lightly n-type doping, which has been reported to be related to reduction in the electron−phonon interaction and electron-disorder scattering.[37]

DOI: 10.1021/acs.nanolett.6b03506
Nano Lett. 2017, 17, 97−103

In the same way, mobility has been reported to be increased linearly with TI thin film thickness and to be saturated as the samples got thicker,[43] following the same trend as the observed spatial electronic disorder behavior. In general, an increase in mobility is due to weak strain from the substrate and reduced defect density,[43] like the one displayed in this nanostructured system.

In conclusion we found in Bi_2Te_3 nanoplatelets a clear thickness dependence of their topological surface state electronic properties. This leads to (1) the evolution from heavily n-type to lightly n-type surface doping as NP thickness increases, probably connected to a decrease in Te_{Bi} antisite defects, which leads to higher quality thicker samples and (2) increase of length scale of phase separation of Dirac electrons with NP thickness, suggesting (together with Raman results) a reduction of electron-disorder scattering and electron−phonon interaction. Under these conditions an increase in mobility is expected.

Our results show a new approach for controlling the surface doping in TI nanostructured systems, which varies in thickness together with nanoscale phase separation of the surface state electronic structure. Recently, TI nanostructures have become a promising platform to explore both fundamental questions and applications related to low dimensionality of electronic systems. According to our results, the increase of n-type charge carrier density and electronic disorder as nanostructures get thinner (and approach the spatial limit) suggests that a good approach to tune Fermi level in these TI system is the use of moderate thickness samples. We expect our work will provide a new route for application of these nanostructured Dirac systems in electronic devices.

■ ASSOCIATED CONTENT

Supporting Information

The Supporting Information is available free of charge on the ACS Publications website at DOI: 10.1021/acs.nanolett.6b03506.

(i) Detailed description of Bi_2Te_3 nanoplatelets growth method and resulting samples. (ii) E_D maps showing percentage variations with respect to mean E_D value. (iii) Autocorrelation and cross-correlation of topographies and E_D maps for all NP thickness. (iv) Angular correlation of E_D maps for all NP thickness (PDF)

■ AUTHOR INFORMATION

Corresponding Author

*E-mail: carolina.parra@usm.cl.

ORCID

Carolina Parra: 0000-0003-3819-7614

Rodrigo Segura: 0000-0003-0928-0021

Author Contributions

The manuscript was written through contributions of all authors. All authors have given approval to the final version of the manuscript.

Notes

The authors declare no competing financial interest.

■ ACKNOWLEDGMENTS

We acknowledge financial support from CONICYT inserción a la academia 791220009, Becas Santander para Jóvenes Investigadores, INCT Nanocarbono, which funded sample growth, STM/STS studies and analysis at Laboratório Nanoscopia UFMG (to C.P., T.H.R.C., F.M.S., P.H.R.G., D.D.D.R., and R.M.P.), and from the US Department of Energy, Office of Basic Energy Sciences, Division of Materials Sciences and Engineering, under contract DE-AC02-76SF00515 and Becas Chile/Programa Bicentenario de Ciencia y Tecnologia, which funded project inception and sample growth, STM/STS studies, and analysis at Stanford University/SIMES laboratories (to C.P., A.W.C., D.K., F.N., Y.C., and H.C.M.). D.K. acknowledges support from the Fundamental Research Funds for the Central Universities.

■ REFERENCES

(1) Luo, C. W.; Wang, H. J.; Ku, S. A.; Chen, H.-J.; Yeh, T. T.; Lin, J.-Y.; Wu, K. H.; Juang, J. Y.; Young, B. L.; Kobayashi, T.; Cheng, C.-M.; Chen, C.-H.; Tsuei, K.-D.; Sankar, R.; Chou, F. C.; Kokh, K. A.; Tereshchenko, O. E.; Chulkov, E. V.; Andreev, Yu. M.; Gu, G. D. *Nano Lett.* **2013**, *13* (12), 5797−5802.

(2) Kong, D.; Cui, Y. *Nat. Chem.* **2011**, *3* (11), 845−849.

(3) Chen, Y. L.; Analytis, J. G.; Chu, J.-H.; Liu, Z. K.; Mo, S.-K.; Qi, X.-L.; Zhang, H. J.; Lu, D. H.; Dai, X.; Fang, Z.; et al. *Science* **2009**, *325* (5937), 178−181.

(4) Alpichshev, Z.; Analytis, J. G.; Chu, J. H.; Fisher, I. R.; Chen, Y. L.; Shen, Z. X.; Fang, A.; Kapitulnik, A. *Phys. Rev. Lett.* **2010**, *104* (1), 016401.

(5) Alpichshev, Z.; Analytis, J. G.; Chu, J. H.; Fisher, I. R.; Kapitulnik, A. *Phys. Rev. B: Condens. Matter Mater. Phys.* **2011**, *84* (4), 041104.

(6) Hsieh, D.; Xia, Y.; Qian, D.; Wray, L.; Dil, J. H.; Meier, F.; Osterwalder, J.; Patthey, L.; Checkelsky, J. G.; Ong, N. P.; Fedorov, A. V.; Lin, H.; Bansil, A.; Grauer, D.; Hor, Y. S.; Cava, R. J.; Hasan, M. Z. *Nature* **2009**, *460* (7259), 1101−1105.

(7) Hor, Y. S.; Richardella, A.; Roushan, P.; Xia, Y.; Checkelsky, J. G.; Yazdani, A.; Hasan, M. Z.; Ong, N. P.; Cava, R. J. *Phys. Rev. B: Condens. Matter Mater. Phys.* **2009**, *79* (19), 195208.

(8) Wang, Z.; Wei, P.; Shi, J. *Front. Phys.* **2012**, *7* (2), 160−164.

(9) Aitani, M.; Sakamoto, Y.; Hirahara, T.; Yamada, M.; Miyazaki, H.; Matsunami, M.; Kimura, S. I.; Hasegawa, S. *Jpn. J. Appl. Phys.* **2013**, *52*, 110112.

(10) Wang, Y.; Xiu, F.; Cheng, L.; He, L.; Lang, M.; Tang, J.; Kou, X.; Yu, X.; Jiang, X.; Chen, Z.; Zou, J.; Wang, K. L. *Nano Lett.* **2012**, *12* (3), 1170−1175.

(11) Kong, D.; Chen, Y.; Cha, J. J.; Zhang, Q.; Analytis, J. G.; Lai, K.; Liu, Z.; Hong, S. S.; Koski, K. J.; Mo, S.-K.; Hussain, Z.; Fisher, I. R.; Shen, Z.-X.; Cui, Y. *Nat. Nanotechnol.* **2011**, *6* (11), 705−709.

(12) Arakane, T.; Sato, T.; Souma, S.; Kosaka, K.; Nakayama, K.; Komatsu, M.; Takahashi, T.; Ren, Z.; Segawa, K.; Ando, Y. *Nat. Commun.* **2012**, *3*, 636.

(13) Xiu, F.; He, L.; Wang, Y.; Cheng, L.; Chang, L.-T.; Lang, M.; Huang, G.; Kou, X.; Zhou, Y.; Jiang, X.; Chen, Z.; Zou, J.; Shailos, A.; Wang, K. L. *Nat. Nanotechnol.* **2011**, *6* (4), 216−221.

(14) Jauregui, L. A.; Pettes, M. T.; Rokhinson, L. P.; Shi, L.; Chen, Y. P. *Sci. Rep.* **2015**, *5*, 8452.

(15) Park, S. H.; Chae, J.; Jeong, K. S.; Kim, T. H.; Choi, H.; Cho, M. H.; Hwang, I.; Bae, M. H.; Kang, C. *Nano Lett.* **2015**, *15* (6), 3820−3826.

(16) Liu, Y.; Li, Y. Y.; Rajput, S.; Gilks, D.; Lari, L.; Galindo, P. L.; Weinert, M.; Lazarov, V. K.; Li, L. *Nat. Phys.* **2014**, *10* (March), 1−6.

(17) Liu, W.; Peng, X.; Wei, X.; Yang, H.; Stocks, G. M.; Zhong, J. *Phys. Rev. B: Condens. Matter Mater. Phys.* **2013**, *87* (20), 205315.

(18) He, K.; Zhang, Y.; Chang, C.-Z.; Song, C.-L.; Wang, L.-L.; Chen, X.; Jia, J.-F.; Fang, Z.; Dai, X.; Shan, W.-Y.; Shen, S.-Q.; Niu, Q.; Qi, X.-L.; Zhang, S.-C.; Ma, X.-C.; Xue, Q.-K. *Nat. Phys.* **2010**, *6*, 584.

(19) Song, C. L.; Wang, Y. L.; Jiang, Y. P.; Zhang, Y.; Chang, C. Z.; Wang, L.; He, K.; Chen, X.; Jia, J. F.; Wang, Y.; Fang, Z.; Dai, X.; Xie, X. C.; Qi, X. L.; Zhang, S. C.; Xue, Q. K.; Ma, X. *Appl. Phys. Lett.* **2010**, *97* (14), 143118.

(20) Kong, D.; Dang, W.; Cha, J. J.; Li, H.; Meister, S.; Peng, H.; Liu, Z.; Cui, Y. *Nano Lett.* **2010**, *10* (6), 2245−2250.

DOI: 10.1021/acs.nanolett.6b03506
Nano Lett. 2017, 17, 97−103

(21) Kong, D.; Randel, J. C.; Peng, H.; Cha, J. J.; Meister, S.; Lai, K.; Chen, Y.; Shen, Z. X.; Manoharan, H. C.; Cui, Y. *Nano Lett.* **2010**, *10* (1), 329−333.
(22) Wang, G.; Zhu, X. G.; Sun, Y. Y.; Li, Y. Y.; Zhang, T.; Wen, J.; Chen, X.; He, K.; Wang, L. L.; Ma, X. C.; Jia, J. F.; Zhang, S. B.; Xue, Q. K. *Adv. Mater.* **2011**, *23* (26), 2929−2932.
(23) Li, Y.-Y.; Wang, G.; Zhu, X.-G.; Liu, M.-H.; Ye, C.; Chen, X.; Wang, Y.-Y.; He, K.; Wang, L.-L.; Ma, X.-C.; Zhang, H.-J.; Dai, X.; Fang, Z.; Xie, X.-C.; Liu, Y.; Qi, X.-L.; Jia, J.-F.; Zhang, S.-C.; Xue, Q.-K. *Adv. Mater.* **2010**, *22* (36), 4002−4007.
(24) Roushan, P.; Seo, J.; Parker, C. V.; Hor, Y. S.; Hsieh, D.; Qian, D.; Richardella, A.; Hasan, M. Z.; Cava, R. J.; Yazdani, A. *Nature* **2009**, *460* (7259), 1106−1109.
(25) Zhang, T.; Cheng, P.; Chen, X.; Jia, J. F.; Ma, X.; He, K.; Wang, L.; Zhang, H.; Dai, X.; Fang, Z.; Xie, X.; Xue, Q. K. *Phys. Rev. Lett.* **2009**, *103* (26), 266803.
(26) Bando, H.; Koizumi, K.; Oikawa, Y.; Daikohara, K.; Kulbachinskii, V. A.; Ozaki, H. *J. Phys.: Condens. Matter* **2000**, *12* (26), 5607.
(27) Kong, D.; Cha, J. J.; Lai, K.; Peng, H.; Analytis, J. G.; Meister, S.; Chen, Y.; Zhang, H. J.; Fisher, I. R.; Shen, Z. X.; Cui, Y. *ACS Nano* **2011**, *5* (6), 4698−4703.
(28) Koma, A. *J. Cryst. Growth* **1999**, *201*, 236−241.
(29) Song, F.; Han, M.; Liu, M.; Chen, B.; Wan, J.; Wang, G. *Phys. Rev. Lett.* **2005**, *94* (9), 093401.
(30) Spirkoska, D.; Abstreiter, G.; Fontcuberta I Morral, A. *Nanotechnology* **2008**, *19* (43), 435704.
(31) He, R.; Wang, Z.; Qiu, R. L. J.; Delaney, C.; Beck, B.; Kidd, T. E.; Chancey, C. C.; Gao, X. P. A. *Nanotechnology* **2012**, *23* (45), 455703.
(32) Sessi, P.; Otrokov, M. M.; Bathon, T.; Vergniory, M. G.; Tsirkin, S. S.; Kokh, K. A.; Tereshchenko, O. E.; Chulkov, E. V.; Bode, M. *Phys. Rev. B: Condens. Matter Mater. Phys.* **2013**, *88* (16), 161407.
(33) Beidenkopf, H.; Roushan, P.; Seo, J.; Gorman, L.; Drozdov, I.; Hor, Y. S.; Cava, R. J.; Yazdani, A. *Nat. Phys.* **2011**, *7* (12), 939−943.
(34) Sessi, P.; Reis, F.; Bathon, T.; Kokh, K. A.; Tereshchenko, O. E.; Bode, M. *Nat. Commun.* **2014**, *5*, 5349.
(35) Hashibon, A.; Elsässer, C. *Phys. Rev. B: Condens. Matter Mater. Phys.* **2011**, *84* (14), 144117.
(36) Carva, K.; Kudrnovský, J.; Máca, F.; Drchal, V.; Turek, I.; Baláž, P.; Tkáč, V.; Holý, V.; Sechovský, V.; Honolka, J. *Phys. Rev. B: Condens. Matter Mater. Phys.* **2016**, *93* (21), 214409.
(37) Chen, C.; Xie, Z.; Feng, Y.; Yi, H.; Liang, A.; He, S.; Mou, D.; He, J.; Peng, Y.; Liu, X.; Liu, Y.; Zhao, L.; Liu, G.; Dong, X.; Zhang, J.; Yu, L.; Wang, X.; Peng, Q.; Wang, Z.; Zhang, S.; Yang, F.; Chen, C.; Xu, Z.; Zhou, X. J. *Sci. Rep.* **2013**, *3*, 2411.
(38) Fratini, M.; Poccia, N.; Ricci, A.; Campi, G.; Burghammer, M.; Aeppli, G.; Bianconi, A. *Nature* **2010**, *466*, 841.
(39) Giraldo-Gallo, P.; Zhang, Y.; Parra, C.; Manoharan, H. C.; Beasley, M. R.; Geballe, T. H.; Kramer, M. J.; Fisher, I. R. *Nat. Commun.* **2015**, *6*, 8231.
(40) Pettes, M. T.; Maassen, J.; Jo, I.; Lundstrom, M. S.; Shi, L. *Nano Lett.* **2013**, *13* (11), 5316−5322.
(41) Giraldo-Gallo, P.; Zhang, Y.; Parra, C.; Manoharan, H. C.; Beasley, M. R.; Geballe, T. H.; Kramer, M. J.; Fisher, I. R. *Nat. Commun.* **2015**, *6*, 8231.
(42) Martin, J.; Akerman, N.; Ulbricht, G.; Lohmann, T.; Smet, J. H.; Von Klitzing, K.; Yacoby, A. *Nat. Phys.* **2008**, *4*, 144.
(43) Kim, Y. S.; Brahlek, M.; Bansal, N.; Edrey, E.; Kapilevich, G. A.; Iida, K.; Tanimura, M.; Horibe, Y.; Cheong, S. W.; Oh, S. *Phys. Rev. B: Condens. Matter Mater. Phys.* **2011**, *84* (7), 073109.

DOI: 10.1021/acs.nanolett.6b03506
Nano Lett. 2017, 17, 97−103